PH.D. THESIS

From Detailed Simulation to Model Reduction: Development of Numerical Tools for a Plasma Processing Application

by Yi-hung Lin
Advisor: Raymond A. Adomaitis

Ph.D. 00-1

ISR develops, applies and teaches advanced methodologies of design and analysis to solve complex, hierarchical, heterogeneous and dynamic problems of engineering technology and systems for industry and government.

ISR is a permanent institute of the University of Maryland, within the Glenn L. Martin Institute of Technology/A. James Clark School of Engineering. It is a National Science Foundation Engineering Research Center.

Web site http://www.isr.umd.edu

ABSTRACT

Title of Dissertation: FROM DETAILED SIMULATION
TO MODEL REDUCTION: DEVELOPMENT
OF NUMERICAL TOOLS FOR
A PLASMA PROCESSING APPLICATION

Yi-hung Lin, Doctor of Philosophy, 1999

Dissertation directed by: Assistant Professor Raymond A. Adomaitis
Department of Chemical Engineering

Low pressure plasma processing is a key step in manufacturing integrated circuits, used both for etching and for enhancing thin film deposition. The plasma discharge reactor systems are characterized by a large number of adjustable parameters and poorly understood transport and reaction mechanisms. This has motivated the vigorous development of models and full scale simulators in the past decade to study various aspects of plasma processing. However, the large scale system models are unsuitable for real-time control, efficient simulation, and iterative process optimization. To increase the utility of the existing simulators, model reduction methods must be used to extract the dominant spatial characteristics of the discharge; numerically efficient spectral projection methods are

then used to generate the reduced model. These practical needs motivated the development of a set of simulation tools that provide a framework for process simulation, model reduction, and analysis of simulator predictions. The goals of this thesis were to build this framework by identifying the computationally common elements of semiconductor manufacturing simulation, model reduction, and analysis methods, and to test these tools on the difficult problem of RF plasma simulation. The simulation tools were developed as a library of MATLAB functions.

In addition to the RF plasma simulations reported in this work, the software library has been applied in the simulation of other semiconductor projects, including chemical vapor deposition and rapid thermal processing. Tests on highly stiff boundary value problems were conducted to examine the accuracy of the numerical techniques; it was found that the global spectral methods were applicable to problems previously thought inappropriate or impossible. Original findings of this thesis research also include the first reported studies of plasma simulator solution convergence and an assessment of model reduction methods applicable to RF discharge simulations.

FROM DETAILED SIMULATION TO MODEL REDUCTION: DEVELOPMENT OF NUMERICAL TOOLS FOR A PLASMA PROCESSING APPLICATION

by

Yi-hung Lin

Dissertation submitted to the Faculty of the Graduate School of the
University of Maryland, College Park in partial fulfillment
of the requirements for the degree of
Doctor of Philosophy
1999

Advisory Committee:

Assistant Professor Raymond A. Adomaitis, Chairman/Advisor
Professor James W. Gentry
Associate Professor Michael T. Harris
Assistant Professor John N. Kidder Jr.
Associate Professor Evanghelos Zafiriou

Dedication

To my parents

Table of Contents

List of Tables

List of Figures

FROM DETAILED SIMULATION
TO MODEL REDUCTION: DEVELOPMENT
OF NUMERICAL TOOLS FOR
A PLASMA PROCESSING APPLICATION

Yi-hung Lin

August 14, 1999

This comment page is not part of the dissertation.

Typeset by LaTeX using the `dissertation` style by Pablo A. Straub, University of Maryland.

Chapter 1

Introduction

Plasmas with low gas pressure ($1mtorr$ to $10torr$), temperature (300 to $500K$), and degree of ionization (10^{-6} to 10^{-1}) are used extensively for manufacturing integrated circuits (ICs). Plasma processing is a key IC fabrication step, used for both etching and enhancing thin film deposition rates (e.g., PECVD). Plasma etching has essentially replaced wet chemical etching in many applications because of its ability to provide anisotropic features of submicron size in controllable fashion. It produces a smaller amount of harmful chemicals relative to wet etching. Additionally, plasma etching offers better opportunities for process integration and large-scale manufacturing. The technique has been used in etching silicon, silicon dioxide, germanium, GaAs, InP, a variety of III-V compounds and contact metals, and stripping photoresist and masking materials. PECVD, on the other hand, enables the deposition of heat-sensitive materials at relatively low temperature. For example, a conventional CVD reactor requires temperature as high as 700^0C to deposit dielectric silicon nitride. With PECVD, the same process can be finished in the range of $100 - 200^0$C.

Plasma discharges used in IC manufacturing are extremely complex. There

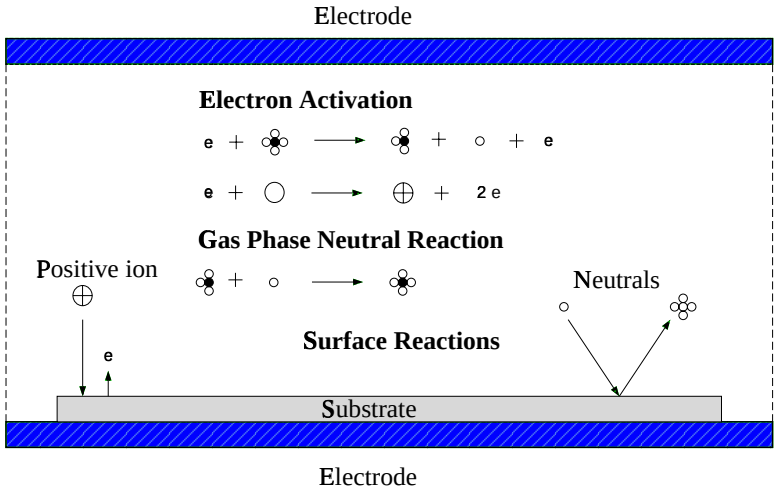

Figure 1.1: Reactions involved in a plasma discharge between two parallel-plate electrodes.

are many interacting effects that need to be considered (see Fig. 1.1). For example, a variety of active species can be generated in the process. The mechanisms of plasma power deposition and loss are not well-understood. The surface condition of the reactor walls may also influence the outcome of the discharge. Other problems include generation of dusty particles [1, 2, 3], gas flow patterns, and heat transfer in the wafer. It has been repeatedly reported that ostensibly identical plasma reactors produce different results with identical operating conditions [4]. These observations can be attributed to the complex nature of plasma processing, resulting in a large number of adjustable design parameters. Therefore, it is difficult to properly design these systems to meet given objectives and to obtain reproducible process results during manufacturing.

A physically based model can provide an understanding of the process by providing insight into various transport and reaction mechanisms. It also can be used to study the effects of parameter values on reactor performance at a low cost

relative to experimental studies. The model can also be used in reactor design for specific applications, process scale-up, and for process control applications. These possibilities have resulted in the vigorous development of models in the past decade to study various aspects of plasma processing (representative works from major research groups include [5, 6, 7, 8, 9, 10, 11, 12]).

Current plasma equipment simulators can perform two-dimensional simulations for their specific design purpose, for example, inductively coupled plasma (ICP), electron cyclotron resonance reactor (ECR), reactive ion etch (RIE), or PECVD systems. Most of these simulators are produced by Lawrence Livermore and Sandia National Laboratories, and by university research laboratories such as the University of California at Berkeley, University of Illinois at Urbana/Champaign, and University of Wisconsin at Madison [12]. The cited simulators take a "first-principles" approach by solving the spatially-lumped Boltzmann equation to obtain the reaction kinetics and transport data, solving the full fluid equations with finite element methods [10] or finite difference methods [13], or solving the Boltzmann equations with Monte-Carlo methods [14, 15], to obtain the spatiotemporal distributions of the state variables. Hybrid methods using both FEM and Monte-Carlo methods are also available [16, 17]. Commercial grade software is also available from CFD Research Inc., Kinema Research and Software, and Scientific Research Associates [12]. These simulators may use models with the similar degree of details as those used by research laboratories [18]. They may otherwise use simplified models to achieve the balance between computational efficiency and true physical predictions. The CFD-PLASMA developed by CDF Research Inc. is such an example of the latter [8].

Motivation and Goals of this Research

The degree of maturity of the detailed simulators continues to increase and three-dimensional tools are emerging [12, 17]. However, the computational cost of using these simulators for process design and optimization can be prohibitive since these simulators frequently require supercomputer-sized computational resources. One of the primary reasons is that a finely-resolved spatial discretization mesh is required to resolve the plasma sheath regions. The system of ordinary differential equations resulting from such a fine discretization of the partial differential equation models becomes too large for real-time control, simulation, and efficient process optimization. Model reduction methods should be used to extract uncorrelated states to increase utility of existing simulators.

Model reduction in this study is defined by the construction of a significantly smaller model by extracting the uncorrelated, core elements from the dynamics of the system. The theoretical methodologies include approximate inertial manifold (e.g., nonlinear Galerkin method [19, 20, 21, 22, 23]) and optimized reduced-basis methods (e.g., principal component analysis, PCA [24, 25, 26, 27, 28]). The implementation mainly involves generation and possibly orthogonalization of globally defined basis functions, and weighted inner product (projection) operations. Both fall in the category of spectral discretization methods. This is one of the key reasons motivating the development of our numerical techniques entirely in terms of spectral theories.

A complete numerical tool set should also be capable of integrating of existing experimental and process data with simulations (e.g., parameter estimation, empirical basis functions) and to answer the open questions regarding plasma simulations, e.g., accuracy, convergence, and stability of solutions. Based on

these considerations and motivated by these practical needs, development of a new software tool set was deemed necessary. The research goals were thus set to build a framework by identifying the computationally common elements of semiconductor manufacturing simulation, model reduction, and analysis methods. These elements were coded as a library of MATLAB functions that form a one-to-one correspondence between the subroutines and the elemental steps of weighted residual method solution procedures. These software tools can be applied to a range of distributed parameter systems such as plasma etch, rapid thermal chemical vapor deposition (RTCVD), and chemical vapor infiltration (CVI) processes [29, 30].

Spectral Discretization Methods

The computational spectral methods and their key elements of implementation can be conceptually put into the framework illustrated in Fig. 1.2. At the heart of this framework are the numerical methods used for defining sets of trial functions. All of the distributed states are then defined in terms of linear combinations of these trial functions – the trial function expansions. The type of functions used, explicitly or implicitly, determine the implementation procedure. Thus, each weighted residual method consists two major steps: generation of trial functions and definition of the residual minimization technique. Generic projection methods such as Galerkin or Tau method [31, 32] expand the solution with known functions, e.g., Fourier series or Jacobi polynomials. A substantial number of terms may be needed to obtain an accurate solution because of the poor choice of general trial functions. The eigenfunctions generated from a Sturm-Liouville problem based on the linear operator of the modeling equation with the given

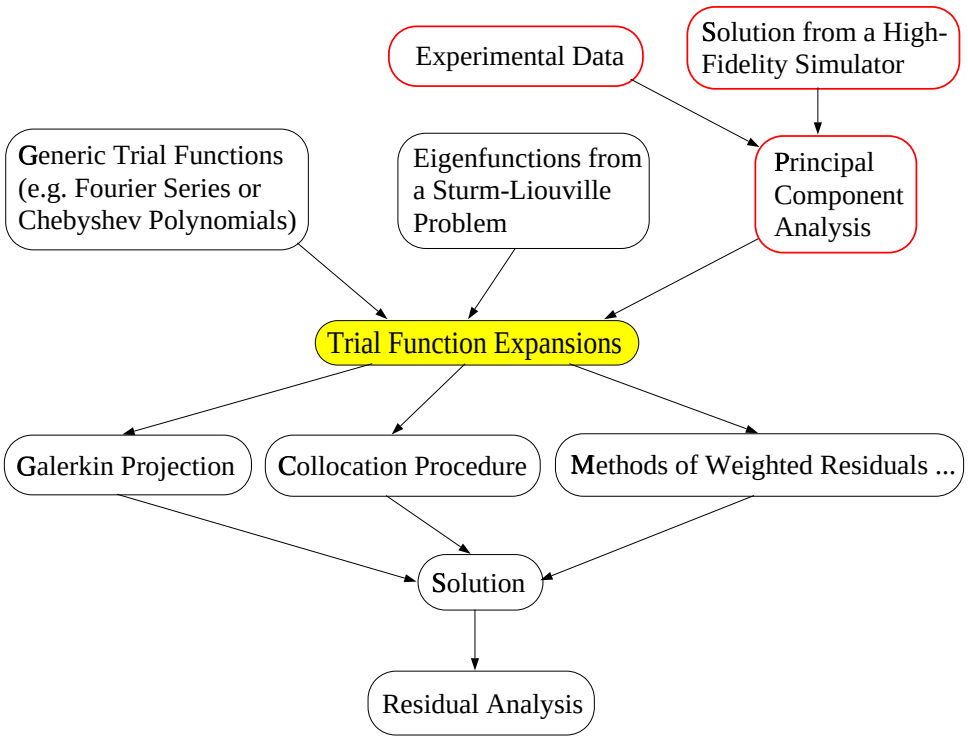

Figure 1.2: Computational framework for Spectral Discretization Methods

boundary conditions may also be used to define the trial functions. The method may not be the most efficient available for solving a modeling equation, especially when nonlinearity is involved. Statistical methods, such as PCA, extract the empirical trial functions from data produced by high-fidelity simulators or spatially resolved process/experimental data. If the state variables are highly correlated, a relatively small number of trial functions (modes) may be sufficient to produce a rapidly convergent trial function expansion. This produces a set of trial functions specially tailored to particular systems under a given set of operating conditions. Additionally, some physical meaning can be ascribed to these computed modes [27, 33]. The number of modes that are required to define these reduced bases depend on the simulation accuracy requirements and

the individual physical systems.

Projection Methods

Once the trial function expansion is determined, the remaining computational procedures are purely mathematical operations. The methods are distinguished by the way the residual function, formed by the substitution of trial function expansions of the distributed states into the modeling equations, is minimized. All methods reduce to a certain form of projecting the residual function onto a sequence of test functions. The Galerkin method uses the trial functions as the test functions in the projection operation used to determine the mode coefficients. Collocation methods demand the residual function vanish at selected spatial positions. Other weighted residual methods, such as the least-squares projection and the method of moments, are conceptually similar [34]. Even some finite element methods (FEM) can be explained using this framework because weighted residual methods are applied in each subdomain [35]. The weak solution equations from the variational formulation is a projection operation carried out by hand calculations. In each subdomain, the trial functions are low order polynomials and vanish in the subdomains that are not contiguous. Due to this nature of the trial functions, the resulting structure of the matrix for the global system of equations is sparse. The implementation of FEMs is distinguished from the global basis function methods by the methods of constructing the global matrix.

Computational Methods

The implementation of the different simulation elements shown in Fig. 1.2 requires differentiation operations, function integration, weighted inner products,

function orthogonalization, and interpolation methods. To efficiently and accurately perform integration and differentiation for arbitrary given functions, the Gauss-Lobatto quadrature method was chosen. The required toolbox functions are all based on the definition of functions in a discretized form. Therefore, a computational method for computing quadrature locations and associated weights was needed. A method calculating the elements of the discrete differentiation arrays was also required. Integration (including weighted inner products) and differentiation of discretized functions thus becomes vector operations in this framework. Discrete function generation, root finding for a discretized function, and Sturm-Liouville problem solution were all required to implement the methods shown in Fig. 1.2. The development of these functions constitute the software library MWRTOOLS.

Dissertation Overview

In summary, the original contributions of the dissertation research are listed as follows:

1. An "open" research framework for simulation, model reduction, and solution analysis was established;

2. Based on this framework, a MATLAB software tool box was written where the individual functions have one-to-one correspondence to the elemental steps of spectral numerical methods. The tool box substantially simplifies the implementation of the numerical methods;

3. The software tools were rigorously tested on the difficult problem of RF plasma simulation;

4. A spectral numerical method based on the global basis functions was first applied to the plasma simulations as an alternative for FEM or FDM. The high order global method was previously thought not appropriate for the solution of such a stiff problem;

5. The first study on the solution convergence of plasma simulations was performed;

6. The PCA based model reduction technique was first applied to a RF plasma model, and several new limitations of the technique were discovered.

The dissertation is organized to provide the necessary information for presenting these contributions. Between this introduction and the conclusion chapter, the material is classified in three chapters. The plasma processing modeling issues are found in Chapter Two. After a short description of plasma fundamentals, the general modeling approaches are presented and the classification of the submodels is introduced. The discussion for fluid type simulations are then followed. The general modeling equations and associated boundary conditions are reviewed. Chapter Three is dedicated to numerical issues involved in this study, including the detailed description of the software toolbox functions, model reduction methodologies used, and relevant nonlinear analysis techniques. In Chapter Four, two major plasma simulations in this study are presented. DC simulations are performed along with solution convergence and bifurcation analysis. One detailed RF simulation is first performed and followed by the model reduction study. The performance and limitations of the model reduction approach are discussed in the end of the Chapter Four.

Chapter 2

Plasma Processing Modeling

The basic principles of plasma processing and common terminology are briefly reviewed in this chapter. For details on various aspects of the technology, there are several excellent texts available: Chapman [36] on the basics of glow discharge, Chen [37] on plasma physics, Manos and Flamm [38] on plasma etching, Boenig [39] on the chemistry and technology of a wide variety of plasma processes, Sherman [40] on PECVD, and a handbook on plasma processing [41].

2.1 Glow Discharge Fundamentals

"Plasma" has long been the subject of scientific study. Before the nineteenth century, it was considered as the fundamental element constituting more than 99% of the known material in the universe. Nowadays, it is commonly referred as the "fourth state of matter," defined as an electrically neutral collection of randomly traveling charged particles. In the 1960's and 1970's, plasma research was dominated by thermonuclear fusion studies. Over the last two decades, plasma processing of semiconductor materials has provided major challenges for

plasma practitioners and theorists.

The classification of plasma systems is often displayed in an electron temperature versus density phase-space plot as Fig. 2.1 (after [42]). In this thesis research, we focus on the glow discharge region. A review of various applications of plasma can be found in the MRS special issue [42].

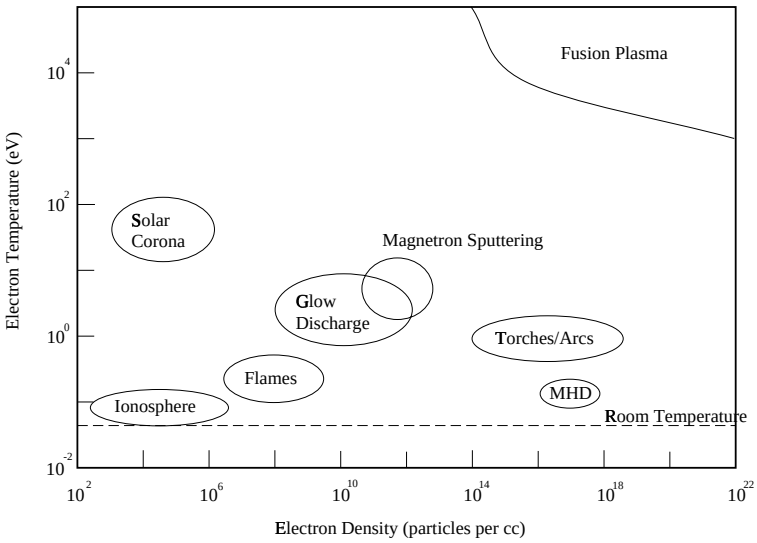

Figure 2.1: Classification of plasma research according to the electron density and temperature. The electron temperature unit is normally expressed in electron volts (eV). 1eV is approximately equal to 11,600 Kelvin (K).

Plasma processing reactors use energy from an external power source (direct current (DC), radio frequency (RF), or microwave) to maintain a self-sustained glow discharge. Because of the low gas pressure and their small mass compared to the gas atoms (molecules), the electrons gain tremendous kinetic energy from the applied electric field but do not lose the energy significantly from the numerous elastic collisions with the background gas. Therefore, the background gas and heavy ions remain relatively cold while the electrons can reach a very high level of

energy (of several eV). The inelastic collisions between the high energy electrons and the gas molecules create reactive and nonreactive fragments responsible for the etching and deposition processes. A variety of electron-impact reactions occur in the discharge. Some examples (from reference [39]) are:

Excitation (vibrational, rotational)	$e + A \rightarrow A^* + e$
Deexcitation	$A^* \rightarrow A + h\nu$
Ionization	$e + A_2 \rightarrow A_2^+ + 2e$
Dissociative ionization	$e + A_2 \rightarrow A^* + A + 2e$
Dissociation	$e + A_2 \rightarrow 2A + e$
Dissociative attachment	$e + A_2 \rightarrow A^- + A^+ + e$
Attachment	$e + A_2 \rightarrow A_2^-$
	$e + A \rightarrow A^-$.

Inelastic collisions between heavy particles also occur leading to other chemical reactions besides the electron-impact reactions. These chemical activities result in a partially ionized discharge consisting of electrons, ions, atoms, radicals, other neutral fragments, and the parent gas (excited or unexcited). This system is hardly in thermodynamic equilibrium. Indeed it is the deviation from thermodynamic equilibrium that is responsible for the effectiveness of a discharge in materials processing and permits low-temperature processing. In order words, the nonequilibrium is the very reason that the system can undergo high temperature chemistry at low temperature.

The above examples are relevant to the processes in the plasma discharge phase. Several heterogeneous reactions occurring on the wafer, electrode, and reactor walls also are important to complete the plasma processing model. The

details of the important surface activity involving the emission of secondary electrons by the impact of electrons and positive ions on the surface can be found in [36]. Likewise, details regarding surface chemistry can be found in [39].

2.2 Plasma Modeling: Goals and Approaches

2.2.1 Plasma Simulator Inputs/Outputs and Goals

The path to developing a complete plasma process model can be organized as in Fig. 2.2 (after [11]). The process figures-of-merit are the goals of process modeling. These quantities are routinely measured and are readily available for comparison against modeling results. However, they are the computed quantities derived from the true process variables. These "primitive" variables, which are shown in the third row of Fig. 2.2, may include gas velocity, gas temperature, density of each neutral species, and electron and ion characteristics. The electron and each type of ion are completely characterized by knowing their density, mean energy, and directed velocity. These are found as solutions to a process model. Once these variables are known, several other variables of interest may be easily determined: electron current, ion current, displacement current, total current, current and voltage at the electrode, ion flux and energy at the wafer, electric field, plasma potential, sheath thickness, rates of various inelastic processes, power distribution in the plasma, power loss mechanisms, and neutral radical flux at the wafer, to name a few.

For the model to produce the quantities of interest, one must identify the critical input parameters and specify the process operating conditions. Ideally, the simulator inputs are shown as the first row of the Fig. 2.2. They are similar

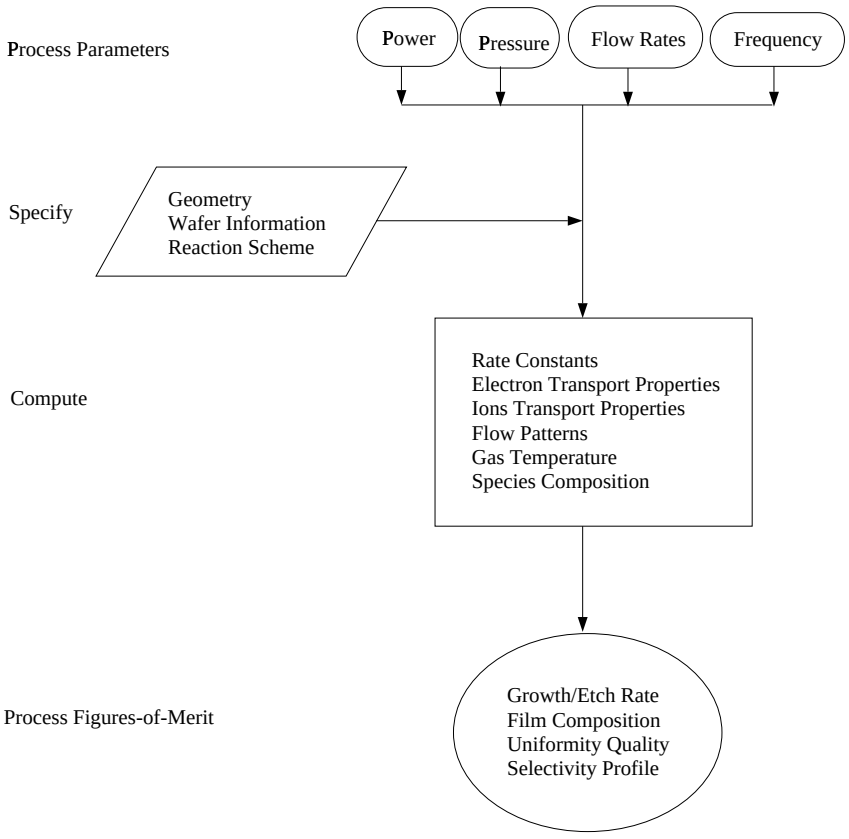

Figure 2.2: Schematic diagram for plasma process modeling goals (after [11]).

to the knobs on the control panel of the reactor. The flow rates of various feed gas streams, reactor pressure, and the power (RF or microwave) input thus can be "dialed" into the simulator. If the generator frequency can be changed at will in the plasma reactor system, it must also be included as an input parameter to the model. However, the power setting may not be the actual power delivered to the plasma since it depends on the matching network employed in the system. If the matching network is not considered, electrode current or voltage, which normally are not input parameters, should be included.

Besides the modeling outputs and inputs described above, a complete processing model should also specify the modeling conditions including reactor geometry and relevant dimensions, gas inlet and outlet locations, location and size of the electrodes, location of the wafer, and the size and number of wafers. To develop a meaningful process simulation, the reaction mechanisms in the plasma and surfaces should be also known. For neutral reactions, the dependence of the reaction rate coefficients should be known. For reactions involving charged species, collision cross-sections must be provided to compute the associated reaction rate constants. The surface reactions are usually characterized in terms of sticking coefficient or reaction probability and sputtering yield parameter. A complete plasma processing model should include the information shown from the first to the third row in Fig. 2.2.

2.2.2 Utility of the First Principles Models

Plasma simulations for etching and deposition have been widely used to predict the performance of the processes. However, most current models are developed using heuristic rules rather than physical-based first principles. One of

the reasons is that the simulations based on the first principles models demand considerable computing resources compared with the much simpler simulations based on the heuristic rules. As the dimensions of the microelectronic devices decrease, the prediction of the process performance by the first principles based simulation becomes increasingly important. It is believed that these models can be effective when coupled to present process models as are shown schematically in Fig. 2.3 (after [43]).

The data provided by the first principles models can be used as input for both statistical yield models like FABRICS and topographic simulation models like SIMPL [43]. This coupling will extend the utility of present process models by reducing their requirements for the results of process test experiments. The first principles models also can be used to guide process test experiments and design plasma processing reactors.

The first principles model should be capable of describing all important plasma physical and chemical processes, including electron impact ionization and dissociation, gas phase chemical reactions, and surface chemical reactions. Ionization mechanisms produce electrons and ions, and sustain the discharge, i.e., electrons and ions are continuously lost to the walls and are replenished by ionization. Ions are more chemically active than their parent gases and are directly related to the surface energy modification. Electron impact ionization is a dissociative process for most of the molecules used in plasma processing. Dissociation of the feed stock gas produces neutral fragments that are chemically active. In fact, this neutral dissociation channel is typically as important or more important than the dissociative ionization channel in producing the chemically active species which drive the plasma processes. Gas phase reactions are

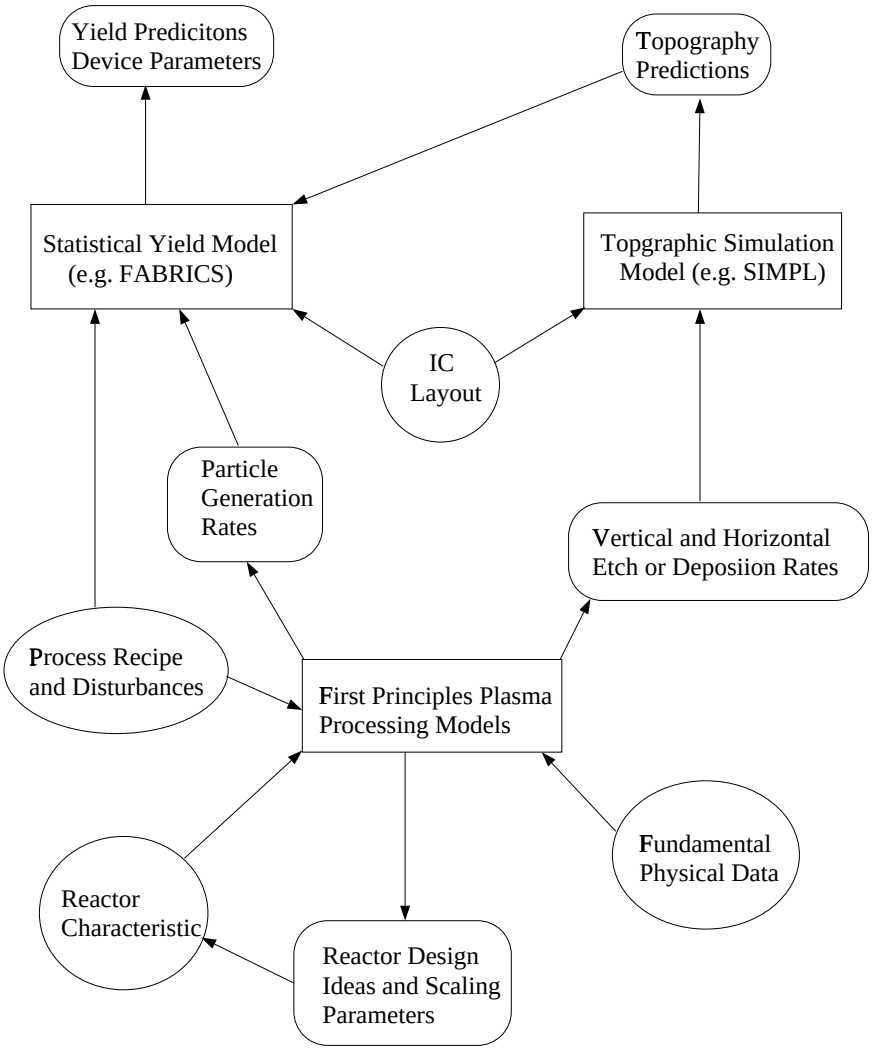

Figure 2.3: Schematic diagram showing the use of a first principles plasma processing model to provide input data to currently available statistical yield and topographic simulation models (after [43]).

important primarily as a loss process for these chemically active species. Gas phase reactions convert chemically active species to stable species and compete with surface processes.

2.2.3 Modular Approach

A full physically based model has not yet been successfully developed. There are many different simplified formulations that have been used. One popular formulation [44] is shown in Fig. 2.4. This formulation conceptually breaks the modeling task into three submodels which treat the discharge physics (plasma physics or glow discharge), the neutral transport (plasma chemistry), and the surface reaction processes as three separate models. The discharge physics model computes the temporally and spatially varying local electric field and densities of charged particles with given electron kinetics. The neutral transport model calculates the densities of neutrals, radicals, and saturated species (including depletion of the feed stock gases). These two models are used to specify the fluxes of radicals and ions bombarding the substrate surface. With these input fluxes, the surface reaction model then predict the modification of the surface properties.

The "submodels" shown in Fig. 2.4 cannot be developed independently because the processes may be tightly coupled and shared by different models. For instance, the fluxes of electrons computed by the discharge physics submodel are used as inputs to conservation equations for neutral species (including radical and metastable species) in the plasma chemistry submodel; the change of neutral densities calculated by the chemistry model are then fed back to the discharge kinetics to modify the local electric field. Similarly, the processes described by

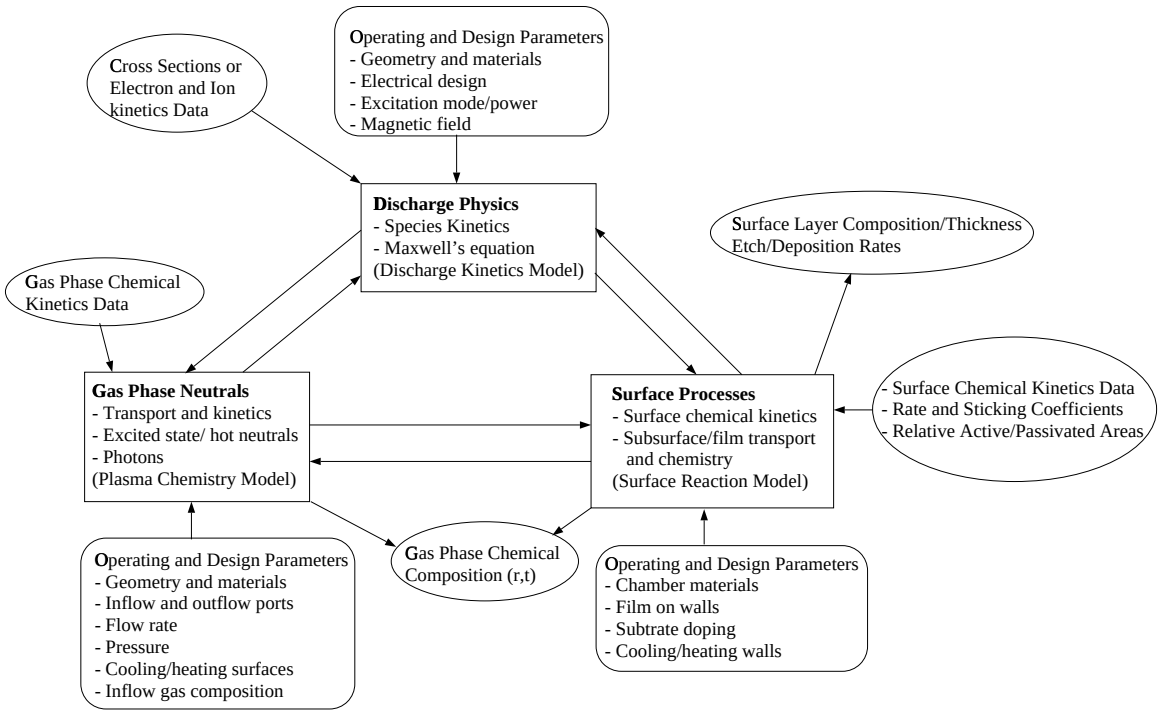

Figure 2.4: Schematic diagram showing the submodels and the interrelationships among models for a first principles plasma processing model. The primary boxes involve equations describing discharge physics, gas phase neutrals, and surface processes, respectively. Each box has associated with its data concerning collisions, and operating and design parameters.

the surface reaction submodel specify the flux of species that flows back into the plasma phase thereby perturbing the plasma chemistry and physics.

Solving the complete first principles model is thus challenging. As a first approach, researchers usually deal with one submodel at a time under applications of interest. The following three subsections provide short descriptions about each submodel with the associated working assumptions.

Discharge Physics Submodel

A model considering only the discharge physics aspects and disregarding gas flow, gas and wafer heating, and reactor issues can be created if the loss of charged particles due to gas convective flow is negligible. The degree of ionization for plasma processing discharges are typically 10^{-4} or lower. In such discharges, recombination in the bulk plasma and on surfaces is the primary mechanism for the loss of charged particles as long as the gas residence time is much longer than the lifetime of the charged species. Under conditions normally encountered in etching and deposition rectors, the fraction of electrons and ions lost with the flowing gas is small. We are therefore allowed to study the transport of electrons and ions in response to the applied electric field in a stationary background gas.

This submodel is used to predict the physical features of the discharge such as electrical characteristics and utilization of applied power. The goal is to develop a set of scaling rules that define the relations between process input parameters and densities, plasma potential, sheath thickness, ion flux, energy, and so forth.

Plasma Chemistry Submodel

This model element is sometimes also known as gas phase neutral model or reactor model. We can consider an idealized reactor model that ignores the details of the glow discharge by assuming an electron density (n_e) profile in the reactor. In addition, the rate constants are taken either from experiments or evaluated using some assumed form for electron energy distribution function (EEDF). Either a constant electron density or an ambipolar profile has been used in reactor models in the literature. However, a constant n_e assumption is somewhat better than an ambipolar profile [11]. The EEDF has been taken as

either Maxwellian or Druyvesteyn.

There are not many reactor model studies reported in the literature. The reason is due to lack of knowledge of n_e and EEDF. Using incomplete or incorrect plasma chemistry cannot accurately predict etch and film deposition rates. Nevertheless, reactor models with the above simplified assumptions have served to illustrate the effect of gas flow and heat transfer on processing rates and etching uniformity. The idealized reactor models provide a framework for understanding gas flow and neutral species transport, and provide a foundation to couple with other submodels for development of complete process models.

The reactor model shares the same foundation of numerical analysis with the computational fluid dynamics (CFD) research. Many computational techniques, particularly in the field of combustion science, have been well-developed to address the problems of nonisothermal flows with several reactive species. Chemical vapor deposition (CVD) modeling, in semiconductor processing, is an excellent example for computational modeling of reactive flows. Representative conservation equations, similar to fluid dynamics equations, for mass, momentum, and energy, respectively can be found in [45] and will be presented later.

Surface Reaction Submodel

In semiconductor manufacturing, thin film deposition or patterning of a thin film are the desired end results; therefore, surface reactions play a key role in plasma processing. Unfortunately, among all three submodels, the surface reactions are the least well understood, and the limited understanding has hindered the development of such models. It is well known that anisotropic etching can be obtained by using a plasma. However, the physical and chemical mechanisms

which produce anisotropic etching are still subject to considerable controversies.

There are typically three different approaches to surface kinetic models. The surface models take the arriving fluxes of species which are predicted by the plasma physics and chemistry models as inputs, and predict the resulting etching and/or deposition rates. The simplest approach to surface kinetic modeling describes the surface reaction processes in terms of net sticking rates. A more complete description can be obtained by writing rate equations which describe the kinetics of the various species which adsorb and react on the substrate surfaces. The most detailed models are Monte-Carlo models that consider the interactions between impinging ions and radicals and the first few layers of the substrate surface in detail. Detailed discussions can be found in [43].

Summary

After this short review of the three submodels (plasma physics, plasma chemistry, and surface reaction), it is clear that the plasma physics submodel is the model with a high priority that needs to be solved. The plasma chemistry (neutral transport) is relatively more advanced than the physics model, and the surface reaction model relies more on an understanding of solid state physics. Once the physics model is finished, the code can be coupled with the transport model with an existing CFD package such as FLUENT or FIDAP. Therefore, in this research, the modeling work will focus on the plasma physics submodel. The remainder of the chapter is devoted to this model.

2.3 Fluid Modeling for Plasma Discharge Physics

The most suitable method for describing the discharge physics is the Boltzmann equation along with Maxwell's equations. However, all the information contained in the Boltzmann distribution function may not be needed. An alternative fluid-type approach based on the moments of the distribution may be used to obtain information on the macroscopic properties of the discharge. In this section, the modeling components of this fluid simulation approach are described in terms of the fluid equations, the reaction kinetics, Maxwell's equations, and the boundary conditions.

2.3.1 The Boltzmann Equation and the General Fluid Model

The Boltzmann Equation

A species j in a discharge can be characterized by a distribution f_j depending on seven variables: three position coordinates $\vec{x}$, three velocity coordinates $\vec{c}$, and time t [46]. The number density of the species at $(\vec{x}, t)$ with velocity components between $\vec{c}$ and $\vec{c} + d\vec{c}$ can be derived from f_j, i.e.,

$$n_j(\vec{x}, t) = \int_{-\infty}^{\infty} f_j(\vec{x}, \vec{c}, t) d\vec{c}.$$

The function f_j may be written as

$$f_j(\vec{x}, \vec{c}, t) = n_j(\vec{x}, t) \hat{f}_j(\vec{x}, \vec{c}, t)$$

where $\hat{f}_j$ is a probability such that

$$\int_{-\infty}^{\infty} \hat{f}_j(\vec{x}, \vec{c}, t) = 1.$$

The Boltzmann distribution function f_j is a special function that satisfies the Boltzmann equation (BE) [46]

$$\frac{\partial f_j}{\partial t} + \vec{c} \cdot \nabla_x f_j + \frac{\vec{F}}{m_j} \cdot \nabla_c f_j = (\frac{\delta f_j}{\delta t})_{collision}. \tag{2.1}$$

In this equation, ∇_c, ∇_x, and m_j represent the gradient in velocity space, the gradient in the (x, y, z) space, and the mass of the particle j, respectively. $\vec{F}$ denotes external forces: if only the electromagnetic field is under consideration, $\vec{F}$ can be $q_j(\vec{E} + \vec{c} \times \vec{B})$ where q_j is the particle charge, and $\vec{E}$ and $\vec{B}$ are time and space-dependent electric and magnetic fields. Finally, the right hand side of (2.1) describes elastic and inelastic collisions that result in redistribution of species j in velocity space as well as in gain or loss of these species.

Moments Approach – Fluid Simulation

The direct integration of the seven-dimensional Boltzmann equation (2.1) is difficult. Pseudo-particle techniques using the Monte-Carlo method are computationally intensive, and the solution f_j often provides more information than is needed for practical applications. An alternate approach, based on the moments of the distribution, may be used to obtain information on the macroscopic properties of the discharge. In general, any number of moment equations do not form a determinate set since each moment equation contains a variable from the next higher moment, which results in more unknowns than the available number of equations. Thus, theoretically, an infinite set of moment equations is equivalent to BE (2.1) and closure relations are then needed to form a determinate set. Three moment equations typically are used to adequately describe the discharge behavior; the physical interpretation of higher-order moments is not clear and for that reason the higher moments are usually not written. Derivation of the

moment equations and closure relations have been discussed in a number of texts and articles such as Chen [37], Lister [47], Ingold [48], and Sawin [49]. In the following, a summary is provided for the first three moments of BE, which are statements of mass, momentum, and energy balances for each species j in the absence of a magnetic field.

The moment equations are obtained by first multiplying Boltzmann equation (2.1) by ϕ, where ϕ is a constant or a function of the velocity $\vec{v}$, and then integrating this product over the velocity space to obtain the "average" quantity. For example, when $\phi = 1$, the species j number density continuity equation is obtained as the zeroth moment,

$$\frac{\partial n_j}{\partial t} + \nabla \cdot n_j \vec{v}_j = \sum_i R_{ij} \tag{2.2}$$

where n_j, $\vec{v}_j$, and R_{ij} are the number density, the average or directed velocity, and the rate of generation or consumption of species j through inelastic collision i.

The first moment is the (vector) momentum equation derived by setting $\phi = m_j \vec{v}$,

$$\frac{\partial (n_j m_j \vec{v}_j)}{\partial t} + \nabla \cdot (n_j m_j \vec{v}_j \vec{v}_j) = -\nabla P_j + q_j n_j \vec{E} - n_j m_j \nu_j \vec{v}_j \tag{2.3}$$

where $(n_j m_j \vec{v}_j)$ and ν_j denote particle momentum and elastic collision frequency; P_j is species partial pressure defined as $n_j k_b T_j$ where k_b is Boltzmann constant. The terms in the momentum equation (2.3) respectively represent time rate of change of momentum, convective acceleration or inertia, pressure gradient, particle drift due to electric field, and finally, momentum loss (or drag) due to electron/gas, ion/gas elastic collisions.

The second moment of the Boltzmann equation is the (scalar) energy con-

servation equation which can be derived by setting $\phi = m_j \vec{v} \cdot \vec{v} = \Im_j$,

$$\frac{\partial \Im_j}{\partial t} + \nabla \cdot \vec{v}_j \Im_j = q_j n_j \vec{v}_j \cdot \vec{E} - \nabla \cdot P_j \vec{v}_j + \nabla \cdot (K_j \nabla T_j) - \sum_i R_{ij} H_i \qquad (2.4)$$

where $\Im_j$, T_j, and K_j are particle energy, species temperature, and thermal conductivity; and H_i is energy loss following inelastic collision process i. Note that the total energy consists of the kinetic energy associated with directed motion and the thermal energy, i.e, $\Im_j = n_j(\frac{1}{2} m_j v_j^2 + U_j)$. The terms in (2.4) respectively represent time rate of change of total energy, convective transport of energy, energy gained from the electric field, rate of work done by pressure forces, energy transport by conduction, and finally, energy loss due to inelastic collisions. The heavy ions exchange energy efficiently with the background gas and so their temperature is close to that of the gas. For this reason, discharge models commonly do not include an energy equation for ions and (2.4) is used only for electrons.

The moment equations (2.3) and (2.4) represent the conservation of momentum and total energy, respectively. For convenience, these equations may be rearranged to yield two equations for nonconserved quantities: velocity $\vec{v}$ and temperature T. The derivations are very similar to the ones in [45] and can also be found in [10, 43]. For convenience, the subscript j in (2.3) and (2.4) is dropped.

The kinetic energy ($\frac{1}{2} nmv^2$) balance that also known as mechanical energy balance in fluid dynamics literature [45] is given as:

$$\frac{\partial(\frac{1}{2} nmv^2)}{\partial t} + \nabla \cdot (\frac{1}{2} nmv^2 \vec{v}) = -\vec{v} \cdot \nabla P + qn\vec{v} \cdot \vec{E} - nm\nu v^2 - \sum_i R_i (\frac{1}{2} nmv^2). \quad (2.5)$$

The terms assume similar meaning as in the total energy equation (2.4). The third term on the right side denotes loss due to elastic collisions. The last term

arises from the energy necessary to raise the energy of newly created electrons to the mean energy of the group. Since $\Im = (\frac{1}{2}nmv^2 + nU)$, a self-consistent equation for thermal energy may be obtained by subtracting mechanical energy balance (2.5) from the total energy balance (2.4):

$$\frac{\partial(nU)}{\partial t}+\nabla\cdot nU\vec{v} = -P\nabla\cdot\vec{v}+\nabla\cdot K\nabla T-\sum_i R_i H_i+nm\nu v^2+\sum_i R_i(\frac{1}{2}nmv^2). \quad (2.6)$$

Note that the last term in equations (2.5) and (2.6) are the same except for a difference in sign. This denotes the interconversion of kinetic and thermal energy. Also note that (2.6) can be solved instead of (2.4) without any loss of accuracy since no approximations were made in going from (2.4) to (2.6) and only simple rearrangements were performed. Equation (2.6) may be more convenient to use than (2.4) since electron temperature is often the quantity of interest. Equation (2.6) is the self-consistent equation for thermal energy and must be used along with (2.2), (2.3), and (2.18) which will be derived later.

Necessary Number of Moments

The full three moment modeling approach consists of the continuity (2.2), momentum (2.3), and thermal energy (2.6) equations along with Poisson's equation (2.18). Based on practical considerations, sometimes one or two moments may be sufficient to form a complete discharge model.

Consider the momentum equation (2.3) and suppose that under some "favorable" conditions, the terms on the left side can be neglected [10]. The result is a relation for $\vec{v}$, or more appropriately, for the flux $n\vec{v}$:

$$n\vec{v} = \frac{1}{m\nu_m}(qn\vec{E} - \nabla nk_bT). \quad (2.7)$$

The particle mobility μ and diffusivity D are defined as

$$\mu = \frac{|q|}{m\nu_m}; \tag{2.8}$$

$$D = \frac{k_b T}{m\nu_m}. \tag{2.9}$$

Combination of (2.8) and (2.9) results in Einstein's relation,

$$\frac{D}{\mu} = \frac{k_b T}{|q|}. \tag{2.10}$$

Taking the variation in T to be small, the second term in (2.7) becomes $D\nabla n$. Then the flux relation, also known as "drift and diffusion relation," is

$$n\vec{v} = sign(q)\mu n\vec{E} - D\nabla n. \tag{2.11}$$

Substituting (2.11) into the continuity equation (2.2) and together with (2.6) form the two-moment approach, which has one less partial differential equation (per species) in each direction than the three-moment approach, potentially reducing the computational efforts required for solving the system of equations.

The assumption for the one-moment approach is that the mean energy is in equilibrium with the electric field. Then the transport and rate constants may be defined and used as a function of E/p instead of U where p is gas pressure. Therefore, the thermal energy equation to compute U is not needed. The "drift and diffusion relation" (2.11) can be used again to further eliminate the momentum equation. The conditions under which various approaches are valid should be carefully examined. Validity arguments were presented in [43] and will not be repeated here.

Validity of Continuum Models

If a discharge can be practically maintained at a given set of pressure, frequency, and power levels, it means that λ, the representative mean free path, is suffi-

ciently smaller than the interelectrode spacing, d. Plasma processes of interest, such as reactive ion etching and some deposition processes, are run at a pressure that is typically less than 0.5 torr. It appears that the three-moment approach will be valid for describing transport within that electrode gap. However, as pressure is further decreased, λ becomes comparable to or larger than sheath thickness d_s. The question of validity of a continuum model arises. It is reasonable to push the limits of utility of continuum models to very low pressures. However, it is necessary to define transport properties and rate expressions appropriately. The utility and validity can only be confirmed by comparison against experiments and self-consistent PIC/MCC simulations, or direct Boltzmann equation solutions.

2.3.2 Reaction Kinetics

For general collisional processes, the total number of collisional reactions occurring per unit volume per second is given by:

$$R = N_1 N_2 \sigma(v) v$$

where N_1 and N_2 represent the densities of the respective interacting species, $\sigma(v)$ is the cross section for the reaction at electron speed v, and v is the relative speed of the reacting particles. The product $\sigma(v)v$ is considered to be the reaction rate per pair of particles in m^3/sec.

For monoenergetic electrons of speed v, this expression is valid. However, the collision cross section can be a very strong function of electron velocity (particularly for inelastic collisions), and the electron velocities are generally described by a distribution. To obtain a realistic representation of the processes

occurring within a plasma we should therefore determine the distribution of velocities of the electrons (or other particles) within the plasma and the mean value of $\sigma(v)v$ should be used, i.e., $< \sigma(v)v >$, which is generally accepted as reaction rate coefficient.

To be precise, we should solve the distribution equations for each and every particle separately. In that case, we would have on the order of 10^{15} to 10^{26} separate equations to describe the plasma behavior in 1 m^3 of space. It is infeasible and also unnecessary. The properties of a plasma that we can observe are due to the contributions of very large numbers of particles and so a statistical description is perfectly adequate. The statistical description is provided by the distribution function.

In order to give a complete specification of the properties of a system of particles, it is necessary to know the position and velocity of each particle: x, y, z, v_x, v_y, and v_z. These six axes define "phase space." The entire system at any instant of time is specified by the positions of the points in phase space where each point represents a particle. As a necessity for the validity of the statistical approach, each elemental volume in phase space must contain a large number of particles. The number of particles in any elemental volume of the phase space is then specified by a distribution function f such as Boltzmann (see (2.1)) or Maxwellian distribution. Therefore,

$$dn = f(\vec{r}, \vec{v}, t) d^3\vec{r} d^3\vec{v} \tag{2.12}$$

represents the number of particles in a volume of phase space

$$d^3\vec{r} d^3\vec{v} = (dxdydz)(dv_x dv_y dv_z)$$

at a point specified by $\vec{r}(x, y, z)$ and $\vec{v}(v_x, v_y, v_z)$. Since this is a time varying

quantity, the distribution function f is also a function of time. As can be seen from the equation (2.12), the distribution function is such that

$$\int_{-\infty}^{\infty} f(\vec{r}, \vec{v}, t) d^3\vec{v} = n(\vec{r}, t)$$

where n is the number density.

Once the distribution function is defined, it can be used to compute averages of quantities representing the collective behavior of particles. For example, the average speed of all particles is

$$< v >= \frac{1}{n} \int_{-\infty}^{\infty} v f(\vec{r}, \vec{v}, t) d^3\vec{v}$$

and the average energy is

$$< \varepsilon >= \frac{1}{n} \int_{-\infty}^{\infty} \frac{mv^2}{2} f(\vec{r}, \vec{v}, t) d^3\vec{v}.$$

Of particular interest is the use of the distribution function to calculate collisional rates. The reaction rate coefficient mentioned before is thus

$$< \sigma(v)v >= \frac{1}{n} \int_{-\infty}^{\infty} \sigma(v) v f(\vec{r}, \vec{v}, t) d^3\vec{v}.$$

As we would expect, an equilibrium distribution function for neutral species is isotropic in velocity space. In other words, there is no preferred direction of motion of the electrons under such circumstances. In this case, and for any other isotropic distribution function, it is worthwhile to define the distribution function $f(\vec{r}, v, t)$ that describes the distribution of the speeds of the particles. To do this, we convert $d^3\vec{v}$ to spherical coordinates in velocity space

$$d^3\vec{v} = d\vec{v_x} d\vec{v_y} d\vec{v_z} = v^2 \sin\theta d\theta d\phi dv.$$

Therefore,

$$\begin{aligned} n(\vec{r},t) &= \int_0^\infty \int_0^\pi \int_0^{2\pi} f(\vec{r},\vec{v},t) v^2 \sin\theta d\theta d\phi dv \\ &= \int_0^\infty 4\pi v^2 f(\vec{r},\vec{v},t) dv. \end{aligned}$$

Since we are considering distribution functions that have no θ or ϕ dependence in velocity space

$$\begin{aligned} n(\vec{r},t) &= \int_0^\infty 4\pi v^2 f(\vec{r},\vec{v},t) dv \\ &= \int_0^\infty f(\vec{r},v,t) dv \end{aligned}$$

so that

$$4\pi v^2 f(\vec{r},\vec{v},t) = f(\vec{r},v,t)$$

can be considered as a distribution function for speed and represents the number of particles in the unit volume $d^3\vec{r}$ at $\vec{r}$ that have speeds in the unit speed interval dv at v. In a slightly simpler notation, neglecting the $\vec{r}$ and t dependence,

$$4\pi v^2 f(\vec{v}) = f(v)$$

if and only if $f(\vec{v})$ is isotropic in velocity space.

This definition is particularly useful in determining the mean values of scalar quantities such as the speed (v), the energy ($\frac{mv^2}{2}$), and collisional excitation rates. In this case, the reaction rate coefficient is then expressed as

$$< \sigma(v)v >= \frac{1}{n} \int_0^\infty \sigma(v) v f(v) dv.$$

Usually the cross sections are expressed in terms of the relative energy of the reacting particles rather than their relative speeds, so it is convenient to

reexpress the speed distribution as an energy distribution by defining

$$\int_0^\infty f(v)dv = \int_0^\infty nf(\varepsilon)d\varepsilon$$

with the aid of $\varepsilon = \frac{mv^2}{2}$. The energy distribution function has been normalized so that

$$\int_0^\infty f(\varepsilon)d\varepsilon = 1.$$

2.3.3 Maxwell's Equations

Self-consistent plasma simulations must solve for the electromagnetic fields that develop in the reactor. The electromagnetic field intensity and flux density vectors are related to each other, to the sources of the field, and to the electric charges and currents by Maxwell's equations. In differential form, Maxwell's equations are

$$\nabla \times \vec{E} = -\frac{\partial \vec{B}}{\partial t}, \tag{2.13}$$

$$\nabla \times \vec{H} = \vec{J} + \frac{\partial \vec{D}}{\partial t}, \tag{2.14}$$

$$\nabla \cdot \vec{D} = \rho, \tag{2.15}$$

$$\nabla \cdot \vec{B} = 0 \tag{2.16}$$

where $\vec{E}, \vec{D}, \vec{H}, \vec{B}, \vec{J}$, and ρ represent the electric field intensity, electric field flux, magnetic field intensity, magnetic field flux, current density, and charge density, respectively. These equations can be augmented with the constitutive relations $\vec{B} = \mu\vec{E}$ and $\vec{D} = \epsilon\vec{E}$ where μ is the permeability and ϵ is the permittivity of the medium.

If the magnetic field is not a function of time (as is the case of a typical GEC cell, see Section 2.4.1), $\frac{\partial \vec{B}}{\partial t} = 0$. Then, the Faraday's law (2.13) implies that the electric field can be written as the divergence of a scalar, namingly the electric potential,

$$\vec{E} = -\nabla V. \tag{2.17}$$

Substituting (2.17) into (2.15) with a position independent dielectric constant results in the Poisson's equation,

$$\nabla^2 V = -\frac{\rho}{\epsilon} \tag{2.18}$$

where $\rho = \sum_j q_j n_j$ is the net charge density. In the equation, the sign of q_j must be used: "+" for positive ions and "−" for electrons and negative ions. When solving the equation over a domain that includes different material properties, the dielectric constant should be kept inside the differential operator.

2.3.4 Boundary Conditions Used in Fluid Simulations

The statements of appropriate boundary conditions are necessary to complete the description of the fluid model. In this section, several popular boundary conditions are summarized for electron number density, ion number densities, electron mean energy, and for the Poisson's equation.

Electron Number Density

The fundamental boundary conditions for electron density are determined from mass balances on the surfaces. The net flux arriving at the surface consists of two contributions: electrons lost due to recombination and secondary electrons generated due to ion bombardment. The flux of electrons to the electrode is given

by $nv_t/4$ where v_t is thermal velocity given by $(8kT_e/\pi m)^{1/2}$. Sometimes this flux is written as $k_r n$ where k_r is a recombination coefficient; comparison with the previous expression gives $k_r = v_t/4$. Including secondary electron emission, the boundary condition for electrons becomes

$$\vec{j_e} = \frac{n_e v_t}{4}\vec{n} - \gamma \vec{j}_+ \tag{2.19}$$

where $\vec{j_e} = -n_e \vec{v_e}$ is the flux and γ is the secondary electron emission coefficient (see [36] for different values of γ). Equation (2.19) is written for a single type of ion striking the surface. For a multi-ion plasma, additional terms should be included to account for the different ions.

Sometimes, zero boundary condition $n_e = 0$ is used by assuming that the secondary electron emission is negligible and electrons are perfectly absorbed by the surface. However, both kinetic and fluid simulations have shown that a substantial electron density can exist near the electrode, especially during the anodic part of an RF cycle [10]. Therefore, Chantry [50] suggests

$$\frac{1}{n_e}\frac{\partial n_e}{\partial x} = \frac{1}{\beta} \tag{2.20}$$

where β is a linear extrapolation length and given as

$$\beta = \frac{2D}{v_t}\left(\frac{1+R}{1-R}\right). \tag{2.21}$$

Here R is the reflection coefficient; v_t and D are thermal velocity and diffusion coefficients, as before. Equation (2.20) implies that the density extrapolates to zero at a distance β beyond the electrode. Chantry shows that if the dimensional scaling variable $\ell\beta/\Lambda$ is much less than unity (ℓ is characteristic container length and Λ is the zero-mode diffusion length), then (2.20) gives results close to $n_e(wall) = 0$. For argon at a pressure below 1 torr, the latter boundary condition is reasonable [11].

Positive Ion Number Density

Although positive ions are presumably completely neutralized at the wall, this happens only within a distance approximately $10^{-8}cm$ from the wall, which would require resolution of a steep ion boundary layer [5]. Setting $n_+ = 0$ at the electrode is thus neither appropriate nor desirable from a numerical point of view. The following expression has served as a good numerical boundary condition:

$$\vec{j}_+ = \mu_+ n_+ \vec{E}. \tag{2.22}$$

The alternative expression

$$\frac{\partial n_+}{\partial x} = 0 \tag{2.23}$$

also has been used. These boundary conditions show that the flux at the electrode is dominated by electric drift due to the large value of the electric field.

For an electronegative discharge, $n_+ > n_- > n_e$ at the electrode, and the condition

$$\frac{\partial E}{\partial x} \approx (\frac{q}{\epsilon_0}) n_+,$$

as inferred from the Poisson's equation, has been used. Setting the positive ion density gradient to zero then means $\frac{\partial^2 E}{\partial x^2} = 0$, which gives that E varies linearly with x. Paranjpe [51] points out that this is incorrect and for mobility-limited ion motion through the sheath, $E \sim x^{1/2}$. The latter can be satisfied by setting the divergence of the flux to zero at the electrode; this indeed is not incorrect since all the generation/loss processes in the continuity equation are negligible near the electrode. The zero-flux gradient condition may be easy to implement in a three-moment approach; however, in a two-moment approach that uses (2.7), implementation of $\frac{\partial (nv)}{\partial x}$ may be more complex.

Negative Ion Number Density

The negative ions in RF discharge are repelled from the electrodes unless ω is small. Therefore, negative ion density at the wall may be set to zero,

$$n_- = 0.$$

Electron Mean Energy

The boundary condition for electron mean energy is written essentially in the form of an energy balance at the electrode [44, 52, 53]:

$$\vec{q}_e = \left(\frac{5}{2}k_b T_e\right)\frac{n_e v_t}{4}\vec{n} - \gamma_+ \left(\frac{5}{2}k_b T_{se}\right)\vec{j}_+ \tag{2.24}$$

where T_{se} is the temperature for the secondary electrons emitted from the surface. When γ_+ is zero, (2.19) and (2.24) suggest that the electron temperature gradient is zero at the electrode. In some models, a constant electron temperature is assumed at the electrode (e.g., [5]); though this condition works well in practice, in general it is not clear what this value should be.

For the three-moment approach, additional conditions are required in the numerical solution procedure to conveniently close the discretized set of governing equations. For this purpose, second-order extrapolation conditions (zero-second derivatives) for the electron and ion velocities are normally used [54].

Poisson's Equation

A zero-voltage condition is imposed to the grounded surface. On the RF driven electrode, a sinusoidal voltage is normally used:

$$V = V_{RF}\sin(\omega t) + V_{DC}. \tag{2.25}$$

The self-bias voltage V_{DC} must be found as part of the solution procedure. The usual approach is to specify V_{RF} and then adjust the value of V_{DC} during the simulation so that the net charged particle (electrons and ions) current at the capacitively coupled electrode is zero [7, 9].

As an alternative, the current boundary condition is also used [53, 55]:

$$I = I_{RF} \sin(\omega t) \tag{2.26}$$

where I is the total current, consisting of all conduction and displacement currents, i.e.,

$$I = \sum_j q_j J_j + J_D \tag{2.27}$$

where

$$J_D = -\epsilon_0 \frac{\partial(\nabla V)}{\partial t}. \tag{2.28}$$

Strictly, the boundary condition at the powered electrode also must include the effects of the external matching network and the surface charge [13, 56].

2.4 Fluid Simulation for Argon Discharge

Plasma discharges used in processing are notoriously complex [4, 57] and the characteristics of the discharges are also strongly affected by the configuration of the reactor [58]. Although the fundamental effects of these factors are generally acknowledged, there have been few systematic studies to determine their influence on the discharges. Owing to the large number of interrelated parameters, it is difficult to isolate the problems that cause different experimental results varying from apparatus to apparatus. The problems have stimulated researchers to share an experimental platform by designing a standard reactor. The reactor

uses RF power sources and the project is patronaged by the Gaseous Electronics Conference [57]. The reactor is thus called Gaseous Electronics Conference RF reference Cell (GEC).

A series of experiments using planar laser-induced fluorescence (PLIF) technique for metastable argon were conducted by McMillin and Zachariah [59, 60] on the GEC reference cell at National Institute of Standards and Technology (NIST) in Gaithersburg, Maryland. The reference [59] provides an ideal source of data to verify the simulations. The authors used a PLIF imaging technique to spatially resolve a two-dimensional argon metastable density field in a low-pressure RF glow discharge. The discharge gas was pure argon. The conditions examined covered a pressure range of 13.3-133.3 Pa ($100mtorr$ to $1000mtorr$) and applied peak-to-peak voltages of $75 - 300$ V. The gas flow rate was fixed at 10 sccm. The measurements include the current waveforms at the surface of the powered electrode, the phase of the voltage with respect to current, the DC self-bias, and the power dissipated in the plasma as a function of gas pressure and the applied peak-to-peak RF voltage. It was found that the metastable argon density field in axial and radial directions varied significantly with the pressure and applied voltage. Pressure had greater influence on the system than voltage did.

Besides the experimental results and the given GEC reactor, argon is considered in this thesis study because of its well-known discharge mechanisms and simple discharge structure. There have been plentiful literature reporting the argon discharge simulations with various numerical techniques such as finite element methods (FEM) [44, 61, 52], direct finite difference methods (FDM) [6, 55, 62, 63], and Sharfetter-Gummel exponential FDM [7, 9]. The discharge

models used were similar to those used for GEC argon simulations. In Section 2.4.1, a model used for GEC is introduced as an example for argon discharge simulations. Then, in Section 2.4.2 the argon discharge literature is reviewed, not limited by GEC system.

2.4.1 Fluid Model, Reaction Kinetics, and Transport Data

A fluid model with the argon reaction recipe and kinetics used for GEC simulation [4, 9, 10, 64, 44] is summarized in this section. The modeling geometry for GEC, the working assumptions, the reaction mechanisms, reaction kinetics using Maxwellian electron energy distribution function, the modeling equations, and the gas flow simulation for a cylinder are introduced in that order.

The GEC System and Modeling Geometry

GEC cell is a parallel plate, capacitively-coupled, RF plasma reactor. It is a research type reactor designed for the studies of basic discharge phenomena, and provides the common ground for the verification of theoretical modeling and comparison of measurements. The design of a standard GEC RF reference cell has been presented in detail in [57]. Figure 2.5 shows the schematic diagram of a standard cell (after [65]). Based on the working assumptions as designed, the geometry of a GEC reference RF cell can be simplied as in Fig. 2.6. In the figure, only does the central chamber of the cell need to be considered. The central part consists of two disk-shaped electrodes with $10.16cm$ in diameter and separated by $2.54cm$. The gas is supplied to the discharge region through the "shower head" in the top electrode, and pumped out from the side and down to the bottom by the symmetric pumping manifold. The entire geometry is symmetric

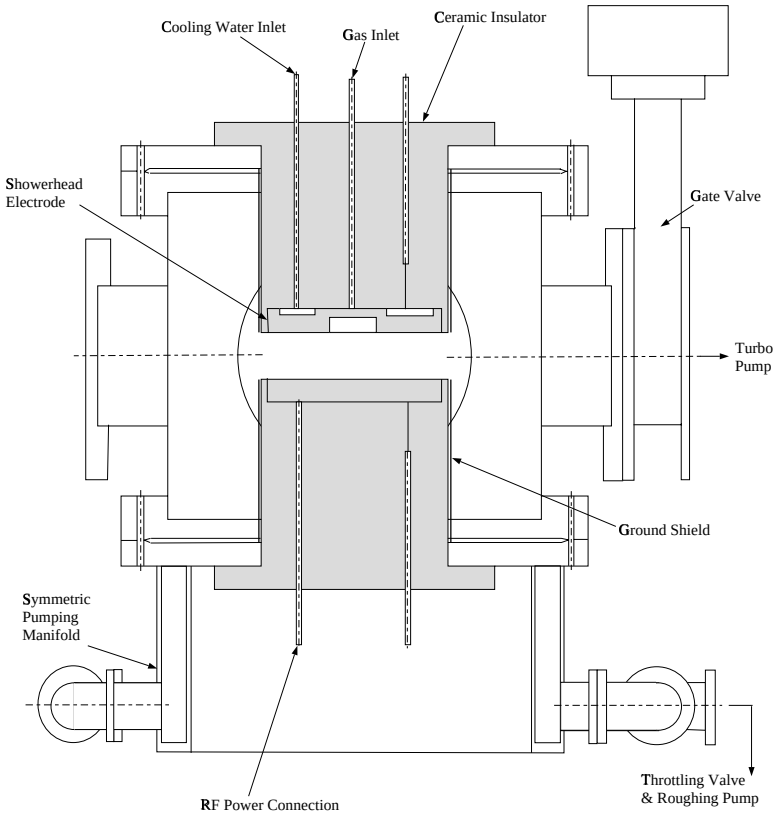

Figure 2.5: Schematic cross-sectional diagram of a standard-configuration Gaseous Electronics Conference RF Reference Cell (after [65]).

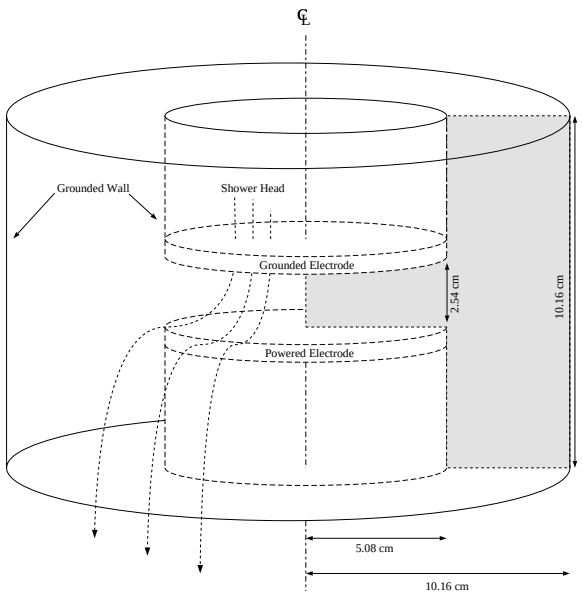

Figure 2.6: Schematic diagram of the simplified capacitively-coupled GEC reference Cell.

around the central line. The bottom electrode is powered while the top electrode is grounded. The dimensions are shown on the figure.

In an effort to produce a more symmetric discharge, GEC cells have also been operated in a symmetric manner, the so-called push-pull mode, where both electrodes are powered in such a way that the applied voltages are 180^0 out of phase [66]. This mode is considered easier to model since no DC bias voltage develops on the powered electrode, but it is more complex to set up and operate, and it may be incompatible with some diagnostics. McMillin and Zachariah's experiments [59] were not operated at the push-pull mode while Lymberopoulos and Economou's simulation [10] was set to this mode.

Assumptions

Basic assumptions used in [4, 9, 10, 44, 64] are summarized below. The assumptions are commonly employed for fluid model and are specific to the two moment approach for argon.

1. The gas is weakly ionized so that only charged-particle-neutral collisions occur, and no magnetohydrodynamic effects need to be considered.

2. The gas pressure is low enough for a glow discharge to be obtained (rather than an arc) but high enough to treat the electrons and ions collectively as fluids. The pressure range is roughly to be 0.5-5.0 torr.

3. The discharge is formed between two parallel conductive electrodes. The discharge properties change along the direction normal and parallel to the electrodes. The system is axially symmetric.

4. The particle flux is described by the diffusion-drift approximation and the effect of convective gas flow is negligible for argon. (Convective gas flow will not be an important factor as long as the gas residence time is much longer than the particle diffusion or reaction time).

5. The electron energy distribution function (EEDF) is not treated explicitly. Instead, an energy equation is solved for the electron "temperature" as if the EEDF were Maxwellian.

6. Since ions are much heavier than electrons, they gain little energy from the applied field and can exchange energy efficiently in collisions with neutral species. Therefore, the ion temperature is assumed constant and equal to

the neutral species temperature. An energy equation for the ions, therefore, is not needed.

7. The electron mobility and diffusivity dependence on electron temperature is negligible in comparison to the electron impact ionization rate on electron temperature.

8. Magnetic field effects are not included.

9. The formation of negative ions is negligible.

10. Molecular ions Ar_2^+ are neglected. Ar^+ is the only ion species under consideration.

Reaction Mechanisms

The reaction recipe used by Lymberopoulos and Economou [10] is shown in table 2.1. Before around 1990, researchers usually treated ground state ionization as the only channel to generate electrons (and ions). It has been found that this assumption results in underestimated electron density and current. In their reaction recipe [10], there are two more methods for producing electrons: stepwise ionization and metastable pooling. Their threshold energies are much lower than the ground state ionization. The discharge becomes easier to sustain and is closer to reality.

Table 2.1 (after [10]) also shows that the four rate coefficients can be treated as constants while four others (k_{ex},k_i,k_{si}, and k_{sc}) cannot. This has been discussed in [10] by Lymberopoulos and Economou. They used zero-dimensional (spatially-averaged) Boltzmann equation solver to produce the kinetics data.

More details about the kinetics will be discussed in the next section. The transport parameters used are listed in table 2.2 (after [44]). The neutral gas density N is computed according to the idea gas law, a reasonable assumption since the gas pressure is low.

Distribution Function for Electron Energy and Reaction Coefficients

As discussed earlier in Section 2.3.2, a reaction rate coefficient is derived from a electron velocity distribution function (EVDF) with a given cross-section data. Unlike Monte-Carlo simulations whose outputs include an EVDF, fluid models take a distribution function as an input to compute the reaction rate coefficients. The popular methods to find EVDF include the experimental EVDF and the solution of a spatially-averaged Boltzmann equation [11]. In this section, we use Maxwellian distribution as an example to demonstrate how to compute the rate coefficients once an EVDF is provided.

It is useful, first, to consider the distribution function of a system which is not subject to any external forces and is in thermodynamic equilibrium. Most texts on Statistical Mechanics and Kinetic Theory give very good treatments of the derivation of such equilibrium distributions based on the determination of the "most probable" distribution. The distribution function for a gas in thermodynamic equilibrium is the Maxwellian distribution

$$f(\vec{v}) = n\left(\frac{m}{2\pi k_b T}\right)^{3/2} \exp\left(-\frac{mv^2}{2k_b T}\right)$$

where k_b is the Boltzmann constant and T is the temperature in Kelvin. Of course, a distribution which is completely Maxwellian is not expected since this would preclude, for example, any current flow in the discharge. Nevertheless, this form can be used to compute some important collisional rates.

Process	Reaction	H_j (eV)	Rate Coefficient
Ground state excitation	$Ar + e \rightarrow Ar^* + e$	11.56	k_{ex}
Ground state ionization	$Ar + e \rightarrow Ar^+ + 2e$	15.7	k_i
Step-wise ionization	$Ar^* + e \rightarrow Ar^+ + 2e$	4.14	k_{si}
Superelastic collisions	$Ar^* + e \rightarrow Ar + e$	-11.56	k_{sc}
Quenching to resonant	$Ar^* + e \rightarrow Ar^r + e$	$\cdots$	$k_r = 2 \times 10^{-7}$
Metastable pooling	$Ar^* + Ar^* \rightarrow Ar^+ + Ar + e$	$\cdots$	$k_{mp} = 6.2 \times 10^{-10}$
Two-body quenching	$Ar^* + Ar \rightarrow 2Ar$	$\cdots$	$k_{2q} = 3 \times 10^{-15}$
Three-body quenching	$Ar^* + 2Ar \rightarrow Ar_2 + Ar$	$\cdots$	$k_{3q} = 1.1 \times 10^{-31}$

Units are $\frac{cm^3}{sec}$ except for k_{3q} which is in $\frac{cm^6}{sec}$.

Table 2.1: Important collision processes included for modeling the argon discharge.

Parameter	Symbol	Value
Electron diffusivity	ND_e	$3.86 \times 10^{22}(cm \cdot sec)^{-1}$
Positive ion diffusivity	ND_+	$2.07 \times 10^{18}(cm \cdot sec)^{-1}$
Metastable atom diffusivity	ND_*	$2.42 \times 10^{18}(cm \cdot sec)^{-1}$
Electron mobility	$N\mu_e$	$9.66 \times 10^{21}(V \cdot cm \cdot sec)^{-1}$
Positive ion mobility	$N\mu_+$	$4.65 \times 10^{19}(V \cdot cm \cdot sec)^{-1}$
Secondary electron coefficient	γ	0.01

Table 2.2: Argon transport parameters.

In this case, the Maxwellian energy distribution is found to be

$$f(\varepsilon) = \frac{2\sqrt{\varepsilon}}{\sqrt{\pi}(k_b T_e)^{3/2}} \exp\left(-\frac{\varepsilon}{k_b T_e}\right)$$

where $\varepsilon = \frac{m_e v_e^2}{2}$. Thus, for the rate coefficients,

$$\begin{aligned} < \sigma(v_e)v_e > &= \int_0^\infty \sigma(v_e)v_e f(\varepsilon)d\varepsilon \\ &= \sqrt{\frac{8}{\pi m_e}}\frac{1}{(k_b T_e)^{3/2}}\int_0^\infty \sigma(\varepsilon)\varepsilon \exp\left(-\frac{\varepsilon}{k_b T_e}\right)d\varepsilon \end{aligned}$$

and for mean electron energy $< \varepsilon >$,

$$\begin{aligned} < \varepsilon > &= \int_0^\infty \varepsilon f(\varepsilon)d\varepsilon \\ &= \frac{3}{2}k_b T_e. \end{aligned}$$

Model Formulation and Boundary Conditions

The Model

A comprehensive self-consistent fluid model used to describe the GEC reference cell can be written as below (following [10]). The derivation of the model is very similar to the continuum model described previously. The details will not be provided here.

Continuity equations:

$$\begin{aligned}
\frac{\partial n_e}{\partial t} + \nabla \cdot \vec{J}_e &= \sum_j R_{ej} \\
\frac{\partial n_+}{\partial t} + \nabla \cdot \vec{J}_+ &= \sum_j R_{ej} \\
\frac{\partial n_*}{\partial t} + \nabla \cdot \vec{J}_* &= \sum_j R_{*j}
\end{aligned}$$

Electric field equations:

$$\begin{aligned}
\nabla \cdot \vec{E} &= \frac{e}{\epsilon_o}(n_+ - n_e) \\
\frac{\partial \vec{E}^{eff}}{\partial t} &= \nu_{mi}(\vec{E} - \vec{E}^{eff})
\end{aligned}$$

Electron energy equation:

$$\frac{\partial \left(\frac{3}{2} n_e k_b T_e\right)}{\partial t} + \nabla \cdot \vec{q}_e + e\vec{J}_e \cdot \vec{E} + 3\nu_{me}\frac{m_e}{M} n_e k_b (T_e - T_g) + \sum_j R_{ej} H_{ej} = 0$$

where the auxiliary equations are

$$\begin{aligned}
\sum_j R_{ij} &= k_i N n_e + k_{si} n_* n_e + k_{mp} n_*^2 \\
\sum_j R_{*j} &= k_{ex} N n_e - k_{si} n_* n_e - k_{sc} n_* n_e - k_r n_* n_e - 2k_{mp} n_*^2 - k_{2q} N n_* - k_{3q} N^2 n_* \\
\vec{J}_e &= -D_e \nabla n_e - \mu n_e \vec{E} + \vec{v} n_e \\
\vec{J}_+ &= -D_+ \nabla n_+ + \mu n_+ \vec{E}^{eff} + \vec{v} n_+ \\
\vec{J}_* &= -D_* \nabla n_* + \vec{v} n_* \\
\vec{q}_e &= -K_e \nabla T_e + \frac{5}{2} k_b T_e \vec{J}_e \\
K_e &= \frac{3}{2} k_b D_e n_e.
\end{aligned}$$

The particle fluxes $\vec{J_i}$ are the superposition of drift under the influence of an electric field, diffusion in a concentration gradient, and convection due to bulk gas flow $\vec{v}$. A drift term was not used for the metastable species since these species are not affected by the electric field. The influence of bulk gas flow on the total flux of charged species is generally small. It is even true for metastable argon provided the effective lifetime of the metastables is much shorter than the gas residence time [44]. However, gas flow can be important in a reactive gas plasma where the radical density depends on flow velocity. In such a case one must also include the momentum and overall mass continuity equations for the neutral gas in order to obtain the $\vec{v}$. A simple flow field computation is provided later in this section.

Boundary Conditions

The boundary conditions also follow [10]. For the sake of completeness, they are listed below.

For Electrons,

$$\vec{J_e} = \frac{v_t n_e}{4}\hat{n} - \gamma_+ \vec{J_+}$$

where electron thermal velocity $v_t = \sqrt{\frac{8k_b T_e}{\pi m_e}}$

For Positive Ions,

$$\text{If} \quad \hat{n} \cdot \vec{E} \geq 0, \qquad \vec{J_+} = \mu_+ n_+ \vec{E}^{eff}$$

$$\text{If} \quad \hat{n} \cdot \vec{E} < 0, \qquad \vec{J_+} = 0$$

For Electric Field,

$$\text{at the powered electrode} \quad V = V_{DC} + V_{RF}\sin(\omega t)$$

$$\text{at the grounded electrode} \quad V = 0$$

For Electron Temperature,

$$\vec{q}_e = \left(\frac{5}{2}k_b T_e\right)\frac{v_t n_e}{4}\hat{n} - \gamma_+\left(\frac{5}{2}k_b T_{se}\right)\vec{J}_+$$

Gas Flow in a Cylinder

The purpose of this subsection is to provide a simple two dimensional gas flow field in the cylindrically shaped chamber. The governing equations for the problem are the equation of continuity, Navier-Stokes equations, and the pressure expression (from the Bernoulli equation). Under the assumptions of steady state, constant density and viscosity, axial symmetry, and ignoring gravity, they are written in cylindrical coordinate system as below [45] (Please note that "$*$" denotes the dimensional quantity in this section.):

Equation of continuity:

$$\frac{1}{r^*}\frac{\partial}{\partial r^*}(r^* v_r^*) + \frac{\partial v_z^*}{\partial z^*} = 0;$$

Navier-Stokes equations:

$$v_r^*\frac{\partial v_r^*}{\partial r^*} + v_z^*\frac{\partial v_r^*}{\partial z^*} = -\frac{1}{\rho_g}\frac{\partial p^*}{\partial r^*} + \nu\left[\frac{\partial}{\partial r^*}\left(\frac{1}{r^*}\frac{\partial}{\partial r^*}\left(r^* v_r^*\right)\right) + \frac{\partial^2 v_r^*}{\partial z^{*2}}\right]; \tag{2.29}$$

$$v_r^*\frac{\partial v_z^*}{\partial r^*} + v_z^*\frac{\partial v_z^*}{\partial z^*} = -\frac{1}{\rho_g}\frac{\partial p^*}{\partial z^*} + \nu\left[\frac{1}{r^*}\frac{\partial}{\partial r^*}\left(r^*\frac{\partial v_z^*}{\partial r^*}\right) + \frac{\partial^2 v_z^*}{\partial z^{*2}}\right]; \tag{2.30}$$

Pressure expression:

$$p_o^* - p^* = \frac{\rho_g}{2}[v_r^{*2} + v_z^{*2}].$$

Instead of solving the full Navier-Stokes equations, the flow problem can be separated into two parts [67]. The exact solution of Navier-Stokes equations is solved for the flow near the bottom surface, where the viscous effect is important.

At a large distance from the surface, the flow is solved with stream function approach (inviscid flow). The two sets of solutions are matched at the interface of the boundary layer. The stream function part is solved first.

To satisfy the equation of continuity automatically, the stream function ψ^* is defined as

$$v_r^* = \frac{1}{r^*}\frac{\partial \psi^*}{\partial z^*} \qquad \text{and} \qquad v_z^* = -\frac{1}{r^*}\frac{\partial \psi^*}{\partial r^*}. \tag{2.31}$$

An irrotational flow satisfies

$$\boldsymbol{\nabla}^* \times \mathbf{v}^* = 0.$$

In this case, it can be written as

$$\frac{\partial v_r^*}{\partial z^*} - \frac{\partial v_z^*}{\partial r^*} = 0. \tag{2.32}$$

Substituting in v_r^* and v_z^* defined above, it becomes

$$r^* \frac{\partial}{\partial r^*}\left(\frac{1}{r^*}\frac{\partial \psi^*}{\partial r^*}\right) + \frac{\partial^2 \psi^*}{\partial z^{*2}} = 0$$

with boundary conditions

$$v_z^*(z^* = 0) = 0$$

$$v_z^*(z^* = L_u) = -U_o$$

and the velocities are finite as $r^* \to 0$ and symmetric around the center. To solve the model, a special form of ψ^* is assumed

$$\psi^* = r^{*2} f(z^*).$$

Thus,

$$v_r^* = r^* f'(z^*) \qquad \text{and} \qquad v_z^* = -2f(z^*). \tag{2.33}$$

Substituting v_r^* and v_z^* into (2.32) results in

$$f''(z^*) = 0 \qquad \text{or} \qquad f(z^*) = az^* + b$$

where a and b are integration constants. Imposing the boundary conditions, the result is $f(z^*) = (\frac{U_o}{2L_u})z^*$, i.e.,

$$\begin{aligned} \psi^* &= Kr^{*2}z^* \\ v_r^* &= Kr^* \\ v_z^* &= -2Kz^* \end{aligned}$$

where $K = \frac{U_o}{2L_u}$. The pressure is then

$$p_o^* - p^* = \frac{\rho_g}{2}K^2[r^{*2} + 4z^{*2}].$$

The dimensionless quantities are defined as

$$r = \frac{r^*}{R_w}; \qquad z = \frac{z^*}{L_u}; \qquad \psi = \frac{\psi^*}{U_o R_w^2}; \qquad v_r = \frac{v_r^* L_u}{R_w U_o}; \qquad v_z = \frac{v_z^*}{U_o};$$

$$\begin{aligned} \psi &= (\frac{1}{2})r^2 z \\ v_r &= (\frac{1}{2})r \\ v_z &= -z. \end{aligned}$$

For the flow near the wafer surface, the same method is applied, i.e.,

$$\psi^* = Kr^{*2}G(z^*)$$

and v_r^* and v_z^* are again defined as (2.31). Therefore,

$$v_r^* = Kr^*G'(z^*) \qquad \text{and} \qquad v_z^* = -2KG(z^*) \tag{2.34}$$

with different boundary conditions:

$$\text{at } z^* = 0,\ v_r^* = 0 = v_z^* \qquad \text{and} \qquad \text{at large } z^*,\ v_r^* = Kr^*$$

with the assumed pressure expression

$$p_o^* - p^* = \frac{\rho_g}{2} K^2 [r^{*2} + F(z^*)]. \tag{2.35}$$

Substitution of (2.34) and (2.35) into (2.29) and (2.30) results in

$$(\frac{\nu}{K}) G'''(z^*) + 2G(z^*)G''(z^*) + [1 - G'(z^*)^2] = 0$$

$$G(z^*)G'(z^*) = \frac{F'(z^*)}{8} - \frac{\nu}{2K} G''(z^*).$$

Defining dimensionless quantities

$$\begin{aligned} \eta &= \sqrt{\frac{2K}{\nu}} z^* \\ G(z^*) &= \sqrt{\frac{\nu}{2K}} g(\eta) \\ F(z^*) &= \frac{4\nu}{K} f(\eta), \end{aligned}$$

the equations become

$$g'''(\eta) + g(\eta)g''(\eta) + \frac{1}{2}[1 - g'(\eta)^2] = 0 \tag{2.36}$$

$$g(\eta)g'(\eta) = f'(\eta) - g''(\eta) \tag{2.37}$$

with the transformed boundary conditions

$$g(\eta = 0) = 0; \quad g'(\eta = 0) = 0; \quad f(\eta = 0) = 0; \quad \eta \to \text{a large value} \quad g'(\eta) \to 1. \tag{2.38}$$

Since (2.36) and (2.37) are decoupled, $f(\eta)$ can be obtained from (2.37) with $f(\eta = 0) = 0$. The direct integration results in

$$f(\eta) = \frac{g(\eta)^2}{2} + g'(\eta). \tag{2.39}$$

The problem becomes simply integrating (2.36) with related initial and boundary conditions in (2.38). It is a two-point boundary value problem and has been solved in [68]. An example computed flow field is shown at Fig. 2.7.

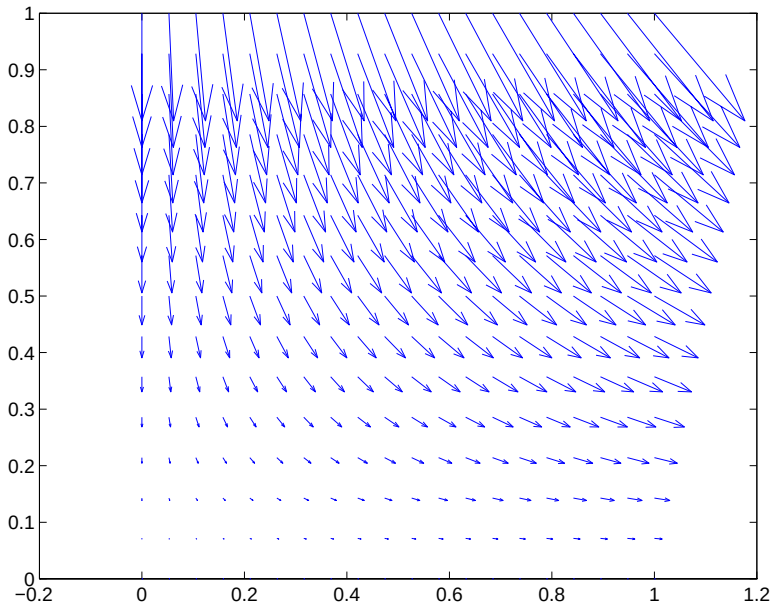

Figure 2.7: An example for the flow field. The vertical coordinate is z and the horizontal axis is for r.

With several tests using the above method of generating the flow field, we found that the bulk phase velocity is not important for argon discharges within the range of interests as mentioned before. This observation is consistent with the results reported in the literature.

2.4.2 Literature Review for DC and RF Argon Discharge Simulation

A fluid model can be used in different simulations for various power sources with minor modification of the modeling equations. The major power sources are di-

rect current (DC), radio frequency (RF), and microwave. Low pressure RF and microwave applications are most interesting to the microelectronic manufacturing industry. However, DC has its own long history and numerous applications, and can serve as a good test for modeling the RF reactor. For RF cases, DC modeling equations are similar to the RF modeling equations without the time dependent terms. For the numerical implementation to be described, the DC results can be treated as the steady state of the time integration. DC results reveal major characteristics of the discharge such as cathode dark space (CDS), negative glow (NG), and plasma potential. In this section, the major characteristics of DC and RF discharges are briefly reviewed.

Direct Current Discharge

Direct current is the first and most completely studied source for low pressure discharge simulations. The DC discharge was used to study the behavior of the current-voltage relation and the regimes of the discharge. The positive column regime was used to study the kinetic and transport parameters. Due to lack of experimental results for transport and kinetics results for high frequency discharges, the DC results are used in RF simulations and the parameters are assumed to be constant. In the numerical implementations, the DC case can be treated as the (time) steady state of the unforced RF simulation. Thus, it is a good idea to solve the DC case before solving a complete RF case when developing a new numerical simulation method [5, 69].

In this section, numerical modeling results for self-consistent low pressure DC discharges are reviewed without reviewing the basic discharge physics. For the references, basic glow discharge physics have been described by Chapman [36].

For brief reviews of DC modeling in terms of surface processing, Lister [47, 70] gives excellent details.

Simulations of the gas discharge structure with a globally defined model are rare although a good deal of work has been done for the positive column region of DC discharge (e.g. [71]). There are one-dimensional models [5, 16, 69, 72] and two-dimensional models [73, 74].

Graves and Jensen [5] apparently first attempted to simulate the entire discharge structure in a self-consistent manner. In that paper, equations for electron and positive ion continuity, the Poisson equation, and an electron energy balance were solved numerically. The discharge simulation was confined between two parallel plate electrodes. Discharge variables were assumed to vary only with axial positions between the electrodes, and gas properties were estimated based on typical values for electropositive gases. They indicated that a systematic study for the entire discharge physics with continuum approach is possible and yields powerful insights. The results show the similarity between the structure of the DC and RF discharges. The CDS region, NG region, and plasma potential were also clearly shown, providing evidence that the electron impact reactions may not only happen inside the CDS region. The ionization occurring in the NG is also possible and important. Therefore, the ionization rate profile consists two peaks, one in the sheath and a smaller one in the bulk.

Meyyappan and Kreskovsky [69] presented a continuum model for glow discharges which include complete momentum balances for both electrons and ions. In the sheath regions, the transport is essentially nonequilibrium in nature due to high electric fields, and particle inertia was considered. Their result only qualitatively confirmed Graves and Jensen's because Meyyappan and Kreskovsky used

real argon data but Graves and Jensen did not. The paper also showed that the well-known relationship pd = constant is valid, where d is the sheath thickness and p is the gas pressure. Additionally, the secondary electron emission was shown to favor ionization. The additional secondary electrons in the sheath increase the local space charge which results in an electric field distribution favoring higher ionization and higher electron temperature peaks.

To our knowledge, after Graves and Jensen [5], the continuum approach became a major approach to be used in modeling glow discharge physics. However, besides Meyyappan and Kreskovsky [69] researchers did not report their DC results except Bogaerts and Gijbels [16]. The main purpose of the paper [16] is not for modeling DC discharge for manufacturing microelectrons. They aimed at modeling the atomization-excitation-ionization sources for analytical spectrometry. Their model equation is the same, the continuum approach, with the exception of higher applied voltage ($1000 volts$). However, their numerical approach is similar to most hybrid models. In their model, they divided the electrons into two groups: slow and fast electrons. The fast electrons have energy higher than the electron ionization threshold energy and are the main contributors to the electron impact reactions. The Monte-Carlo simulation was performed along with the fluid simulation. In this study, the electrons found to have energy lower than the ionization energy were defined as the slow electrons. The simulation results were very similar to those described previously [72]. However, the fast electron density is high in the CDS and gradually decreases to the anode, but the average density is five orders lower than that for the slow electrons. These results are very similar to so-called multiple beam models, which assume an energy distribution function for electrons inside CDS or sheath.

Bogaerts and Gijbels [72] applied the same method in [16] and included the metastable argon effect. The metable argon was found to play a minor role in the ionization of argon atoms, but have a significant effect on the secondary electron emission at the cathode.

A one-dimensional model shows the basic discharge structure while a two-dimensional model reveals the radial discharge structure. The geometry effect that plays a key role in the discharge can be studied in the multidimensional simulation. Boeuf [73] assumed a linear relationship for voltage along the side wall. His results indicated that radial electric field at the plasma-sheath boundary tends to draw electrons towards the center of the negative glow and positive ions away from it. The stability of the discharge in the normal regime is due to this radial electric field.

Bogaerts and Gijbels [74] used the same method as in [16, 72] with the extension to the radial direction. They found that the average behavior is similar to the one-dimensional model. Inside the CDS there are large electric field gradient both in axial and radial directions. In the NG region, the electric field was linear both in axial and radial directions.

According to the above discussions for DC glow discharge, a short summary can be drawn as follows. Ions and electron profiles essentially overlap in the bulk phase (NG). Since the sheath region is thin, the system can be said to be quasineutral. Ionization occurs both in the sheath and bulk region although it occurs primarily near the sheath-bulk boundary. A fairly small group of electrons are in charge of the ionization rate. They gain energy from the field and are accelerated from the cathode to the sheath-bulk boundary, where they reach the highest energy. Most of them collide with neutrals near the boundary. Some do

not collide with neutrals or still have enough energy after collisions. They can ionize the neutral in the bulk phase. The potential is always positive relative to both electrodes. It is flat in the bulk phase and drops quickly to the cathode. The specific shape of the profile is decided by the reactor geometry. The electron temperature profile exhibits a sharp peak inside the cathode sheath and a fairly flat profile in the bulk before a drop in the anode sheath region. The sharp rise in temperature is due to electrons gaining energy from the high electric field in the cathode sheath. Since ionization is an endothermic process, it is followed by a local electron temperature drop.

Radio Frequency Discharge

As indicated before, RF simulation is very similar to the DC simulation with the difference being the time dependent terms. As will be shown, the major difference is defined by the voltage boundary condition. The voltage boundary condition at the powered electrode is expressed in terms of a sine (or cosine) function. Therefore, we can expect a symmetric result around the center, and the discharge structure consists of two sheaths near the electrodes with a bulk phase in the center.

In fact, the electron and ion density profiles both look much like cosine profiles. The bulk phases of the two profiles are almost unchanged and overlap. Inside the sheaths, electron density is modulated by the RF cycle while the ion profile is essentially fixed. This is because the heavy ions are unable to follow the instant electric variations. Also as expected, the potential field is modulated by the RF field. The electron energy peak, which is inside the momentary cathodic sheath, switches between two sheaths with time.

The majority of RF discharge simulations are still one-dimensional [52, 54, 61, 75, 76, 77, 78] (e.g., for Argon). Two-dimensional simulations [7, 9, 44, 64] begin to emerge around 1990; there are still few three-dimensional simulations (e.g., [79] in 1996). Due to their computational intensiveness (even for fluid simulations), the number of publications for two- and three-dimensional models is still limited.

Since current-voltage characteristics are fundamental to the understanding of discharge behavior and are routinely measured, it is important to compare model predictions against experimental data. Such comparisons often reproduce the functional I-V relation exactly; however, the predicted current for a given voltage tends to be smaller than the experimental results. This means that the model predicts a higher voltage than actually needed to sustain a given current [49, 62, 80]. The reported experimental errors alone do not account for this discrepancy. It is more likely due to the limited number of ionization channels considerered in the simulations. For example, the argon simulations only accounted for direct ionization. However, it has been shown that inclusion of metastables and two-step ionization in argon results in a significant increase in plasma density and current [52]. Lymberopoulos and Economou [52] accounted for the two-step ionization and metastable quenching by two and three-body reactions and pooling in addition to the usual single-step ionization and excitation. This comprehensive set of inelastic processes resulted in a fivefold increase in plasma density at 1000 mtorr than the simulations which did not consider metastables. These findings indicate that the neutral transport must be coupled to discharge studies in a self-consistent manner even for inert gases.

Boeuf and Pitchford [9] used an approach very similar to that of Lymberopou-

los and Economou [44, 64] except that they did not include metastable neutral transport. They compared their simulation results with the data by Overzet and Hopkins [81] and they found good agreement with those measurements. The agreement was much better at $33.3Pa$ than at $13.3Pa$ which is surprising since Boeuf and Pitchford did not include metastables in their calculation and the metastable contribution is expected to be more significant at the higher pressure [10].

Lymberopoulos and Economou [10] also showed that higher voltages and/or pressures enhance the off-axis radial peak in electron density. As voltage increases the radial electric field increases as well which in turn increases the ionization rate near the radial edge of the plasma.

Young and Wu [82] simulated a 13.56 MHz helium discharge in a geometry relevant to the capacitively coupled GEC cell. They truncated the surrounding chamber by placing a cylindrical solid wall confining the discharge to a radius of $5.08cm$. The electrode spacing in their simulation was $2.54cm$ as in the standard GEC reference cell. They used a fluid approximation with the full momentum and energy equations for the electrons and the drift-diffusion approximation with an effective electric field for ions. They did not consider metastable transport in their simulation. Electron-impact reaction rate coefficients and transport properties were obtained by a zero-dimensional DC Monte Carlo simulation. They also showed that a peak in the radial profile of the time-average ion density appears in this case as well. They attributed this peak to the presence of a radial electric field which provides extra heating of the electrons in the region close to the radial wall. In this case the radial electric field is present because of the sheath that forms naturally near the radial wall. It is interesting to note that

their result is similar to that obtained in the open GEC geometry where the radial confining wall is aways from the electrodes [9, 44, 64].

Davie et al. [53] also observed an off-axis radial peak in the charge density in a reactor with radial confining wall. They used the fluid equations with the drift-diffusion approximation without considering the inertia of heavy ions. They used Arrhenius form for ionization and excitation rates of argon as a function of electron temperature. They also did not include the metastable transport. They used a sinusoidal total current boundary condition at the powered electrode. The radial wall was an insulator which was grounded on the opposite side. When the insulator was "thick," the discharge was nearly symmetric since the resistance was too high for displacement current to flow through the insulator. Local maxima in ionization are seen near the discharge corners which they attributed to extra electron heating at the corners due to the focusing of the RF current by the radial sheath. As in the cases of the simulation by Young and Wu [82] and Lymberopoulos and Economou [44, 64], the presence of a radial sheath contributes to extra electron heating. Since the spatial distribution of ionization and excitation rates in argon are similar, the local maxima would produce a local enhancement in the density of metastable species, should they have included metastables in the calculation [10].

Fluid models have also successful predicted mode transitions (such as α to γ transition) [14, 49, 62] and discharge behavior near extinction [49, 62]. Two dimensional simulations for electropositive discharge have begun to emerge [64, 82, 83]. For a two-dimensional three-moment model, one RF simulation reportedly needed 100 hours of CRAY-XMP time [83]. The results showed that plasma variables in the center of the discharge are only about 5% different from

the corresponding one-dimensional results [64, 82, 83]. It is near the edge, as expected, that the density is different from that in the center. Indeed, the density near the wall is higher. The electrons tend to diffuse from the electrode zone toward the walls. but they experience a strong space-charge field near the electrode edge regions, which results in a local pileup of electrons. This emphasizes the need for multidimensional simulations to investigate plasma nonuniformities across the reactor.

Chapter 3

Weighted Residual Methods and Model Reduction

There has been a considerable amount of research devoted to developing numerical techniques for solving boundary-value problems (BVPs) [84, 85, 86, 87]. This reflects the prevalence of BVPs in chemical engineering modeling problems involving transport and distributions defined on finite domains. For many of these problems, it is natural to pose solutions $u(x, y, z, t)$ in the form of trial function expansions

$$u(x, y, z, t) = \sum_{i,j,k=1}^{N_x, N_y, N_z} a_{i,j,k}(t)\psi_{i,j,k}(x, y, z) \tag{3.1}$$

where each trial function $\psi_{i,j,k}(x, y, z)$ is defined over the entire physical domain Ω and its boundaries $\partial\Omega$. Partial differential equation solution procedures based on this form of trial function expansion fall under the broad classification of the spectral methods. In this study, we focus on developing a set of computational procedures for implementing these discretization procedures.

Substituting (3.1) into the partial differential modeling equations

$$\frac{\partial \mathbf{u}}{\partial t} = \mathbf{G}(\mathbf{u}) \quad \text{in } \Omega,$$

the boundary conditions $\mathbf{F}(\mathbf{u}) = \mathbf{0}$ that are not satisfied by the individual $\psi_{i,j,k}$ on $\partial\Omega$, and the initial conditions $\mathbf{u}(x, y, z, 0) = \mathbf{u}_0(x, y, z)$ in Ω defines one or more residual functions. There are a number of different methods for minimizing residual function norms and the most appropriate choice depends on the problem to be solved. The process of choosing the spatial mode amplitude coefficients $a_{i,j,k}$ to minimize the residual norm distinguishes the different weighted residual methods, but they all involve (exactly or approximately) the projection of the residual function R onto individual test functions ϕ_m using the weighted inner product

$$(R, \phi_m)_\omega = \int_\Omega R\phi_m \, \omega(x, y, z) \, dv. \tag{3.2}$$

We note that this inner product definition separates the overall weight function into the weight associated with any assumed problem symmetries contained in the definition of the differential element dv and the additional weight function $\omega(x, y, z)$.

It is the method by which the projection operation is carried out or the definition of the test or weight function that differentiates the MWR. *Eigenfunction expansions* are based on expressing the solution in terms of trial functions defined by the eigenfunctions of a Sturm-Liouville problem related to the BVP to be solved; the overall accuracy of this solution procedure normally depends on the accuracy to which the nonhomogeneous terms and initial conditions are approximated by the eigenfunction expansions. The *Galerkin method* is based on choosing a trial function expansion and projecting the residual onto each function, making the residual orthogonal to the sequence of trial functions. This method is applicable to nonlinear problems, especially when a *pseudospectral* formulation is used to simplify the implementation of the Galerkin projection.

Finally, the *orthogonal collocation* method is a pseudospectral technique based on a specific collocation point selection procedure that tends to reduce aliasing errors for nonlinear systems, giving a good and sometimes exact analog to the Galerkin method. The discrete-ordinate formulation of this method makes it convenient to use and provides much "intuitive feel" to the solution procedure.

3.1 Spectral Discretization Methods

3.1.1 Current MWR Software

There have been a large number of important contributions to the collection of numerical techniques available for solving BVPs by the different MWR. We present a partial survey of *computational* techniques based on globally-defined and spatially-localized trial function methods. Algorithms based on shooting techniques are not discussed.

PDECOL is a package written by Madsen and Sincovec [88] to solve systems of nonlinear partial differential equations in one space and one time dimension. The package implements finite element collocation methods based on piecewise polynomials for the spatial discretization. The boundary value problem solver COLSYS by Ascher et. al. [89], or the enhanced version COLNEW, solves the mixed-order systems of BVPs defined by ordinary differential equations. In this spline collocation method, solutions are represented by B-spline functions evaluated at the Gaussian points defined in each subinterval. An adaptive spline point placement algorithm is used, based on minimizing a residual norm. The Fortran codes `jcobi.f, intrp.f, dfopr.f` and `radau.f` written by Villadsen and Michelsen [87] are a set of subroutines for solving BVPs with the orthogonal

collocation method; the subroutines are used to compute the differentiation and quadrature arrays, and for interpolating solutions between the collocation points.

The general chemical engineering software package Octave [90] developed by Rawlings and Ekerdt contains an orthogonal collocation subroutine to compute the collocation arrays based on the original algorithms of Villadsen and Michelsen [87]. The pseudo-spectral differentiation software package PseudoPack [91] written by Don and Solomonoff computes differentiation arrays at the Gauss-Lobatto quadrature points using three different collocation methods. Fast transform and filtering algorithms are included in this package to enhance the speed and stability of computations.

The MATLAB PDE toolbox [11] integrates a mesh generation algorithm, finite element technique, and a graphical user interface to solve BVPs in complex 1D or 2D geometries. The package is applicable to single partial differential equation models with piecewise-constant forcing terms. MacCluer [92] includes a number of Mathematica examples of solving linear, 1-dimensional BVPs, and Articolo [93] presents a comprehensive overview of eigenfunction expansion solutions to 1- and 2-dimensional linear BVPs using Maple V. Analytical solution methods for linear and nonlinear partial differential equation problems are combined with MATLAB-based numerical techniques in [94]. A survey of BVP solvers that includes programs based on finite-difference, spline collocation, and projection methods with globally defined trial functions can be found in [95].

Much emphasis has been placed on the numerical accuracy of computed quantities such as collocation array elements; as pointed out in [84], error analysis of computed solutions has been, for the most part, restricted to the comparison of numerical solutions to exact solutions. An example of one study that examined

the convergence of solutions produced by BVP solvers is the paper of Denison and Hamrin [96], which analyzed the numerical errors in BVP solvers DD04AD and COLSYS with respect to two test examples.

3.1.2 MWRTOOLS Discretization Techniques

The numerical techniques developed in this thesis are distinguished from the studies cited in the previous section in that the goal was to develop a computational toolbox consisting of a common set of numerical tools for implementing the different MWR techniques inside the MATLAB computational environment. The intention was to identify the numerical elements common to the different MWR and then to develop MATLAB functions that form a one-to-one correspondence between the subroutines and the elemental steps of an MWR solution procedure. Furthermore, the accuracy of the elements of MWR implementation (such as the collocation arrays, inner product calculations, etc.) was assessed, and tools and techniques for assessing the accuracy of the solutions computed with these methods were provided. The conceptual goal of making simple weighted inner product computations, computing eigenfunction sequences, etc., was to provide the next step in doing "back-of-the-envelope" type calculations for distributed parameter systems with methods for accurately assessing the discretization error.

Since the trial functions ψ_n of (3.1) can be defined by polynomials, trigonometric functions, Bessel's functions, or any other special function, the key concept that made possible an interchangeable set of MWR computational tools was establishing a numerical technique for accurately representing these functions while retaining the maximum flexibility in choosing the form of the functions[1].

[1]Note that the same concept applies to the factors making up $\psi_{i,j,k}(x,y,z) =$

The method starts with a discrete representation for a given arbitrary function at its discretized points:

$$f(x) = \sum_{i=1}^{M} \ell_i(x) f_i \qquad \text{with} \qquad \ell_i(x) = \prod_{\substack{j=1 \\ j \neq i}}^{M} \frac{x - x_j}{x_i - x_j}. \tag{3.3}$$

This is Lagrange's classical formula consisting of M terms, each a polynomial of degree $M-1$ and each constructed to be zero at all of the x_i except at $x = x_i$, at which it is constructed to be f_i. Then, the (quadrature) integration of the function with a weighted function $w(x)$ can be approximated as

$$\begin{aligned} \int_o^1 w(x) f(x) dx &\approx \int_0^1 w(x) \left(\sum_{i=1}^{M} \ell_i(x) f_i \right) dx \\ &= \sum_{i=1}^{M} f_i \int_0^1 w(x) \ell_i(x) dx \\ &= \sum_{i=1}^{M} f_i w_i \end{aligned}$$

and the differentiation operations become

$$\begin{aligned} \frac{df(x)}{dx} &= \sum_{i=1}^{M} \frac{d\ell_i(x)}{dx} f_i; \\ \frac{d^2 f(x)}{dx^2} &= \sum_{i=1}^{M} \frac{d^2 \ell_i(x)}{dx^2} f_i. \end{aligned}$$

In the following subsections, the open issues regarding how to distribute the discretized positions x_i and how to compute w_i will be discussed. The implementation issues including construction of differentiation arrays, interpolation for values not on the grids, and finding roots of an arbitrary discrete function will be also discussed.

$X_i(x)Y_j(y)Z_k(z)$ in higher-dimensional systems.

Quadrature Position x_i and Weights w_i

The method for choosing the number M and positions x_i of fine-scale discretization points depends strongly on the problem and aspects of the MWR solution procedure. In general, the number M must be larger than the trial function truncation number N; for polynomial trial functions the minimum M is the maximum trial function degree q plus one, and for other trial functions the minimum M depends on the accuracy of the trial function approximation desired. Furthermore, accurate residual calculations for strongly nonlinear problems require more than the minimum M. For example, an accurate spectral decomposition of a residual generated by a quadratic function requires $M = 2q + 1$. As it will be demonstrated, however, that accurate inner product calculations do not necessarily require $M = 2q + 1$ (as a result of the product of two functions) by the choice of the quadrature weights.

Many of the numerical difficulties encountered in solving BVPs are attributable to slow convergence rates of the residual in the neighborhood of the boundary condition locations. Thus, the choice of x_i positions must balance interpolation performance against the accuracy of quadrature weights. Given all these considerations, the fine-scale discretization point locations as $x_1 = 0$ and $x_M = 1$ are chosen, and the interior points are the roots of the $(M-2)$-order Jacobi polynomial $J_{(M-2)}^{(1,a+1)}(x)$, where $a = 0, 1$, and 2, and corresponds to the slab, cylindrical, and spherical geometries. These polynomials are orthogonal with respect to weight function $(1-x)x^{a+1}$ in the unit interval. The roots are distinct, are all located inside the unit interval [97], and are spaced in such a manner that the fine-grid discretization point density increases towards each end of the interval.

This choice of fine-scale discretization points also guarantees that the quadra-

ture weights $\mathbf{w}$, used to compute

$$\int_0^1 f(x)\, x^a dx = \mathbf{w}^T \mathbf{f}$$

where $\mathbf{f} = [f(x_1), \ldots, f(x_M)]^T$ result in exact integral evaluations when the degree of f is less than $q = 2M + 1$. Therefore, in the context of the inner product definition (3.2), the w_i can be considered as the discrete approximations to the differential element dv.

Accurate and efficient algorithms for computing the values of $\mathbf{x}$ as the roots of a Jacobi polynomial and the associated quadrature weights $\mathbf{w}$ have been developed [34, 97, 98]. However, these algorithms can be modified to improve their numerical accuracy and efficiency, and to take advantage of vectorized MATLAB operations. Our algorithm starts with placing $3M$ points at the extrema of a $(3M-1)$th degree Chebyshev polynomial (see Eqn. (4.2)). Corresponding Jacobi polynomial values and their derivatives are evaluated with the general recursive formula that generates these polynomials. The sign change intervals are identified and linear interpolation is used to determine initial guesses as the first step of the Newton-Raphson method. Roots that do not satisfy a specified accuracy tolerance are refined with the Newton-Raphson iterations until they do so. This defines the parallelized algorithm used to compute the root location vector $\mathbf{x}$.

Since the x_i are roots of a polynomial, the node spacing in the limit of the endpoints is inversely proportional to the square of the total number of points used. This suggests that these polynomial trial functions can resolve features with length scales of order M^{-2} in the boundary layers while retaining good convergence properties in the bulk phase (see the discussions in [31], page 40).

For a given M and geometry constant a, the analytic formula for w_i is given

by Villadsen [34] as

$$w_i = \frac{(2M+a-1)c_M^{(1,a+1)}}{\left[\frac{dP_M(x_i)}{dx}\right]^2} \cdot K_i$$

where $P_M = \prod_{j=1}^{M}(x - x_j)$ and $K_i = \frac{1}{a+1}$ for $i = 1$; $K_i = 1$ otherwise. The coefficient $c_M^{(1,a+1)}$ is evaluated using

$$c_M^{(1,a+1)} = \frac{(M-2)!\Gamma(M+a+1)\Gamma(M+a)\Gamma(M)}{(2M+a-1)\Gamma^2(2M+a)}.$$

As M increases, the machine accuracy of the operations used to compute the constant soon saturate with round-off errors due to the evaluation of the product and quotient of Gamma functions. To overcome this problem, special form of w_i is realized as $\frac{CK_i}{\left(\frac{dP_M(x_i)}{dx}\right)^2}$ where $C = (2M+a-1)C_M^{(1,a+1)}$. Since $\sum_{i=1}^{M} w_i = \frac{1}{a+1}$ must be true,

$$\frac{1}{C} = (\alpha+1)\sum_{j=1}^{M} \frac{K_j}{\left(\frac{dP_M(x_j)}{dx}\right)^2}.$$

This algorithm eliminates the need to compute Gamma function values, improving the accuracy of the computed w_i and extending the range of the maximum value of M.

Discrete Differentiation Operations

Because the Lagrangian interpolation polynomials $\ell_i(x)$ are continuous and differentiable over the entire domain, explicit formulas for derivatives of functions represented by these trial function expansions up to order $(M-1)$ can be obtained that are valid for all $x \in [0,1]$. In the discrete-ordinate formulation of the collocation method, differentiation is a matrix operation, i.e., $\frac{d\hat{\mathbf{T}}}{dx} = \hat{\mathbf{A}}\hat{\mathbf{T}}$ and $\nabla^2\hat{\mathbf{T}} = \hat{\mathbf{B}}\hat{\mathbf{T}}$ where the elements $\hat{A}_{ji}$ and $\hat{B}_{ji}$ are defined as

$$\hat{\mathbf{A}}_{ji} = \frac{d\ell_i(x_j)}{dx} \text{ and } \hat{\mathbf{B}}_{ji} = \frac{1}{x_j^a}\frac{d}{dx}\left(x_j^a \frac{d\ell_i(x_j)}{dx}\right) \qquad i,j = 1,2,\cdots,M. \tag{3.4}$$

The terms in each array are computed by directly differentiating the Lagrange interpolation equations, and the values of the nodal polynomial derivatives at the fine-scale discretization points $\hat{\mathbf{x}}$ are computed with the recurrence formulas derived by Michelsen and Villadsen [98].

$$\hat{A}_{ji} = \begin{cases} \frac{1}{2}\frac{P_M^{(2)}(x_j)}{P_M^{(1)}(x_j)} & j = i \\ \frac{1}{(x_j - x_i)}\frac{P_M^{(1)}(x_j)}{P_M^{(1)}(x_j)} & j \neq i \end{cases}$$

and

$$\hat{b}_{ji} = \frac{d^2\ell_i(x_j)}{dx^2} = \begin{cases} \frac{1}{3}\frac{P_M^{(3)}(x_j)}{P_M^{(1)}(x_j)} & j = i \\ 2\hat{A}_{ji}\left[\hat{A}_{jj} - \frac{1}{x_j - x_i}\right] & j \neq i \end{cases}$$

where $P_M^{(1)}$, $P_M^{(2)}$, and $P_M^{(3)}$ are calculated from the following recurrence formulas

$$\begin{aligned} P_0(x) &= 1 \\ P_j(x) &= (x - x_j)P_{j-1}(x) \\ P_j^{(1)}(x) &= (x - x_j)P_{j-1}^{(1)}(x) + P_{j-1}(x) \\ P_j^{(2)}(x) &= (x - x_j)P_{j-1}^{(2)}(x) + 2P_{j-1}^{(1)}(x) \\ P_j^{(3)}(x) &= (x - x_j)P_{j-1}^{(3)}(x) + 3P_{j-1}^{(2)}(x) \end{aligned}$$

where $j = 1, \cdots, M$ and $P_0^{(1)} = P_0^{(2)} = P_0^{(3)} = 0$. The definition of the discrete Laplacian operator $\hat{\mathbf{B}}$ is then constructed from these differentiation arrays, using asymptotic values for the operator at the origin in the case of cylindrical and spherical geometries to eliminate the numerical singularity caused by the $1/x^a$ term. The numerical discretization techniques described for constructing the fine-grid quadrature weights, differentiation arrays, and collocation point locations build on the computational techniques of [87].

Sturm-Liouville Problem Solver

A time-consuming step in the implementation of an eigenfunction expansion solution procedure is the actual computation of the eigenvalues and definition of the eigenfunctions. In our solution framework, the `sl.m` function was to developed [99] to compute solutions (λ_n, ψ_n) to the subset of Sturm-Liouville problems defined by

$$\frac{1}{x^\alpha v(x)} \frac{d}{dx}\left(x^\alpha p(x)\frac{d\psi}{dx}\right) + q(x)\frac{d\psi}{dx} + g(x)\psi = \lambda\psi \qquad x \in (0,1). \tag{3.5}$$

The solutions $\psi(x)$ are subject to boundary conditions

$$\begin{aligned} a\frac{d\psi(0)}{dx} + b\psi(0) + a_1\frac{d\psi(1)}{dx} + b_1\psi(1) &= 0, \\ c\frac{d\psi(1)}{dx} + d\psi(1) + c_0\frac{d\psi(0)}{dx} + d_0\psi(0) &= 0. \end{aligned} \tag{3.6}$$

Therefore, Dirichlet, Neumann, mixed, periodic, and semiperiodic boundary conditions can be satisfied.

The λ_n and ψ_n are computed as the eigenvalues and eigenvectors of an array defined by the differentiation arrays corresponding to the differential operators and discretized functions $\hat{\mathbf{v}}$, $\hat{\mathbf{p}}$, $\hat{\mathbf{q}}$, and $\hat{\mathbf{g}}$. In the first step of this procedure, the boundary conditions are used to define a linear relationship between the values of ψ at the interval endpoints, and is used to reduce the discretized eigenvalue problem (3.5) to homogeneous form. After computing the $M-2$ eigenvalues and eigenvectors, the endpoint values of the discretized eigenfunctions are computed to satisfy the boundary conditions, giving the matrix of discretized eigenfunctions $\mathbf{\Psi}^{M\times(M-2)}$. Error control is performed by evaluating the eigenvalue problem residuals generated when the eigenfunctions are interpolated to a finer discretization grid; eigenfunctions that produce residuals exceeding an infinity-norm bound are discarded [99].

Spectral Polynomial Interpolation

The interpolation is based on Lagrange's formula. The classical algorithm (3.3) gives no error estimates, and it is numerically infeasible to directly compute the coefficients of high-order interpolating polynomials. Neville's algorithm [100] is used to obtain the same interpolation result. It is numerically stable and provides an error estimate with no extra cost.

Let P_i, $i = 1, \cdots, N$, be the zero degree polynomial passing through the point (x_i, y_i); thus, $P_i = y_i$. Let $P_{i(i+1)}(x), i = 1, \cdots, N-1$, be the degree one polynomial passing through (x_i, y_i) and (x_{i+1}, y_{i+1}). Likewise, the highest order polynomial $P_{12\cdots N}(x)$, the desired answer, is the value of the unique interpolating polynomial through all N points. The various $P's$ form a "tableau" with "ancestors" on the left leading to a single "descendant" at the extreme right. For example, with N = 4,

$$
\begin{array}{lllll}
x_1: & y_1 = P_1 & & & \\
 & & P_{12}(x) & & \\
x_2: & y_2 = P_2 & & P_{123}(x) & \\
 & & P_{23}(x) & & P_{1234}(x) \\
x_3: & y_3 = P_3 & & P_{234}(x) & \\
 & & P_{34}(x) & & \\
x_4: & y_4 = P_4 & & &
\end{array}
$$

Neville's algorithm is a recursive way of filling in the numbers in the tableau a column at a time, from left to right. It is based on the relationship between a "descendant" and its two immediate "ancestors,"

$$P_{i\cdots(i+m)}(x) = \frac{(x - x_{i+m})P_{i\cdots(i+m-1)} + (x_i - x)P_{(i+1)\cdots(i+m)}}{x_i - x_{i+m}}. \qquad (3.7)$$

This recurrence works because the two "ancestors" already agree at points x_{i+1} $\cdots$ x_{i+m-1}; any points x on $P_{i\cdots(i+m)}(x)$ should pass through "two points": $(x_i, P_{i\cdots(i+m-1)}(x))$ and $(x_{i+m}, P_{(i+1)\cdots(i+m)}(x))$. The algorithm is in fact the same as recursively rearranging the Lagrange's classical formula.

An improvement on the recurrence (3.7) is to keep track of the small differences between "ancestors" and "descendants", namely define

$$\begin{aligned} C_{m,i} &= P_{i\cdots(i+m)}(x) - P_{i\cdots(i+m-1)}(x); \\ D_{m,i} &= P_{i\cdots(i+m)}(x) - P_{(i+1)\cdots(i+m)}(x) \end{aligned}$$

for $m = 1, 2, \cdots, N-1$. Thus, with the aid of (3.7)

$$\begin{aligned} C_{m+1,i} &= \frac{(x_i - x)(C_{m,i+1} - D_{m,i})}{x_i - x_{i+m+1}}; \\ D_{m+1,i} &= \frac{(x_{i+m+1} - x)(C_{m,i+1} - D_{m,i})}{x_i - x_{i+m+1}}. \end{aligned} \tag{3.8}$$

Therefore, at each level m, the $C's$ and $D's$ are the corrections that make the interpolation one order higher. The final answer $P_{12\cdots N}(x)$ is equal to the sum of any y_i plus a set of $C's$ and/or $D's$ that form a path through the family three to the rightmost descendant.

The implementation can be initiated with the linear interpolation formula for $P_{i(i+1)}(x)$, $i = 1, \cdots, N-1$:

$$P_{i(i+1)}(x) = \begin{cases} P_i + \frac{(x_i - x)(P_{i+1} - P_i)}{x_i - x_{i+1}} &= P_i + C_{1i} \\ P_{i+1} + \frac{(x_{i+1} - x)(P_{i+1} - P_i)}{x_i - x_{i+1}} &= P_{i+1} + D_{1i} \end{cases}$$

and continue with (3.8). The last correction is considered as the error estimate.

The above algorithm puts no constraints on the positions of x_i. However, for a uniform distribution, as N increases, the interpolation errors near end-points

grow faster than those in the center. This is so-called Runge Phenomenon (see e.g. [101]). The errors can be almost evenly distributed if the x_i positions are quadratically clustered towards the ends. The improvement is attributive to using the well-behaved interpolation polynomials $\ell_i(x)$ (in 3.3 and also see the plots in [101]). This explains the high accuracy of our differentiation and interpolation routines.

Roots of Discrete Functions

An immediate use of spectrally accurate interpolation is to find the roots of a discrete function. Most numerical methods find roots of a function with a given analytic formula of the function. For a polynomial, successive deflation of the polynomial for the previously found roots is popular [100]. However, the procedure is a sequential algorithm and may be subject to error accumulation.

A better algorithm for implementation with MATLAB is based on using Newton-Raphson method to refine the roots and Neville's interpolation algorithm to find the required function values. For a given discrete function and its first derivative, the Newton-Raphson formula for each distinct root is a independent, point-wise operation, i.e., for i-th root

$$x_i^{k+1} = x_i^k - \frac{f(x_i^k)}{f'(x_i^k)}$$

where k is the number of refinement and $'$ denotes the derivative. The implementation starts with a linear interpolation and refines the roots simultaneously using MATLAB vector operations. The algorithm is well-suited for finding the real, distinct roots of a discrete first order continuous function.

3.1.3 The MWRtools Functions

The library of functions developed for implementing the weighted residual methods contains computational procedures for defining the problem domain and sets of trial functions, and general functions for spectrally discretizing problems, including collocation methods, that are described below. The notation describing the function input and output variables is $\mathbf{Q}$ for arrays, $\mathbf{q}$ for column vectors, q for scalar inputs, q for alphanumeric input, and {q} for parameters contained in MATLAB cell arrays.

$[\mathbf{Q},\ \mathbf{w},\ \mathbf{A},\ \mathbf{B}] = \texttt{colmat}(\mathbf{\Phi}, \mathbf{x}, \hat{\mathbf{x}}, \hat{\mathbf{w}}, \hat{\mathbf{A}}, \hat{\mathbf{B}})$

Computes the collocation differentiation arrays $\mathbf{A}$ and $\mathbf{B}$, discrete transformation array $\mathbf{Q}$, and quadrature weights $\mathbf{w}$ at the collocation points $\mathbf{x}$ based on the discretized set of trial functions $\mathbf{\Phi}$. Other inputs include the fine-grid discretization point locations $\hat{\mathbf{x}}$, quadrature weights $\hat{\mathbf{w}}$, and the discrete first-order differentiation and Laplacian operator arrays $\hat{\mathbf{A}}$ and $\hat{\mathbf{B}}$, respectively. If only one fine-grid discretization array is specified in the input, the output is its corresponding collocation array. This function is normally called after `colpts.m`.

$[\mathbf{x}] = \texttt{colpts}(\mathbf{\Phi}, \hat{\mathbf{x}}, \hat{\mathbf{w}}, \mathbf{x_p}, \hat{\mathbf{A}})$

Computes collocation points $\mathbf{x}$ from a set of discretized trial functions $\mathbf{\Phi}$ as the union of a set of pre-selected points $\mathbf{x_p}$ and the roots of one of the trial functions. Roots are determined after the trial functions are orthonormalized with respect to quadrature weights $\hat{\mathbf{w}}$ if specified; the roots of each trial function are computed in a reverse sequence until the total number of collocation points equals the number of trial functions N.

If $\mathbf{x_p}$ is empty, $N-1$ roots are computed corresponding to an interior collection method. Since the roots are computed by the Newton-Raphson-based function `rdf.m`, increased accuracy can be obtained if the (optional) first-order differentiation array $\hat{\mathbf{A}}$ is provided.

[s] = `fsf`(ν, N)

Produces a vector of Fourier-space filter coefficients s used in the trial function expansions to reduce the oscillations associated with the Gibb's phenomenon (Gottlieb and Shu, 1997). These oscillations result from projecting a discontinuous function (represented in discretized form) onto globally defined, smooth trial functions generated by either `gdf.m` or `sl.m`. The filter order is ν, and N is the number of trial functions.

[$\mathbf{\Psi}$] = `gdf`($\hat{\mathbf{x}}$, 'f(x̂,p)', 'x̂', {'p', $\mathbf{p}$})

Generates discretized representations of a sequence of trial functions $\mathbf{\Psi}$ according to the alphanumeric input formula f(x̂,p), the fine-scale discretization grid $\hat{\mathbf{x}}$ and the parameter p. The cell array contents consist of the parameter name 'p' and its numerical value(s) $\mathbf{p}$. Additional parameters can be specified by concatenating the parameter name/value pairs. The functions can be polynomials, eigenfunctions generated by the explicit solution to a Sturm-Liouville problem, or an arbitrary sequence of functions chosen as part of a Galerkin discretization. This function is normally called after `pd.m`.

$[\mathbf{\Phi}] = \mathtt{gs}(\mathbf{\Psi}, \hat{\mathbf{w}})$

A modified Gram-Schmidt orthogonalization procedure that provides better control of round-off errors than its classical counterpart. Starting with the first column (discretized function) in $\mathbf{\Psi}$, the orthogonalization algorithm proceeds by removing all components of the remaining functions not orthogonal to the current function in each iteration. Orthogonality is defined by the discretized weight function $\hat{\mathbf{w}}$. Each trial function is also normalized during this process. Frequently, this function is used in conjunction with `gdf.m`.

$[\hat{\mathbf{x}}, \hat{\mathbf{w}}, \hat{\mathbf{A}}, \hat{\mathbf{B}}, \hat{\mathbf{Q}}] = \mathtt{pd}$('geom', M)

Sets up the physical domain in terms of discrete points in the unit interval and defines the differentiation operators according to any imposed problem symmetries. This function is normally called first in the solution procedure. The inputs are the geometry ('slab', 'disk', 'sphe', or 'peri') and the number of discretization points M. The output consists of the discretization grid $\hat{\mathbf{x}}$, quadrature weights $\hat{\mathbf{w}}$, the first-order differentiation array $\hat{\mathbf{A}}$, and the discrete equivalent to the Laplacian operator $\hat{\mathbf{B}}$. This function also computes the discretized set of M Jacobi polynomials $\hat{\mathbf{Q}}$, a discrete transformation array used for filtering and spectral decomposition applications.

The discretization point locations and quadrature weights are based on the modified Gaussian quadrature method (Gauss-Lobatto method). The two end points (0 and 1) are preassigned and interior positions are the roots of the $(M-2)$th degree Jacobi polynomial $J_{M-2}^{(1,\alpha+1)}(x)$ where α is the geometry

factor. The quadrature weights are computed after the discretization grid point locations are determined. The differentiation arrays are based on the Lagrange interpolation polynomial with the given M points. In this study, the recursive formula of the polynomial is used to construct the differentiation arrays.

[**y**, **dy**] = `polyint`(**xi**, **yi**, **x**)

Lagrange polynomial interpolation based on Neville's algorithm. This recursive formula is obtained by rearranging the order in which the implementation of Lagrange interpolation calculations are performed. The result is spectrally accurate and provides an error estimate **dy**. The function takes the input interpolants **yi** with respect to **xi** and the positions **x** to be interpolated, producing the interpolated result **y**.

[**r**] = `rdf`(**x**, **f**, **df**, ϵ)

Computes the roots **r** of a discretized function **f**. This function can be used to compute eigenvalues described by nonlinear relationships, and is also used for computing collocation point locations in `colmat.m`. The inputs consist of any discretization grid **x** and the corresponding function values **f** (and the optional first order derivative values **df**). The intervals bracketing the roots are found first and a linear interpolation in each interval is performed to find the roots. If the first-order derivatives are given, the roots are refined using the Newton-Raphson iterations (and `polyint.m`) until given tolerance ϵ is satisfied.

$[\boldsymbol{\lambda}, \boldsymbol{\Psi}, \boldsymbol{\Phi}, \mathbf{w_{ef}}, \mathbf{w_{ad}}] =$ `sl`('geom', $\hat{\mathbf{A}}$, $\hat{\mathbf{x}}$, a, b, c, d, $\hat{\mathbf{w}}$, $\hat{\mathbf{v}}$, $\hat{\mathbf{p}}$, $\hat{\mathbf{q}}$, $\hat{\mathbf{g}}$, *errtol*, a_1, b_1, c_0, d_0)

A Sturm-Liouville problem solver, for problems of the type described by equations (3.5) and (3.6), that computes the vector of eigenvalues $\boldsymbol{\lambda}$, discretized, orthonormal eigenfunctions $\boldsymbol{\Psi}$, adjoint eigenfunctions $\boldsymbol{\Phi}$, discretized weight function $\mathbf{w_{ef}}$ used to define the orthogonality of the eigenfunctions, and discretized weight function $\mathbf{w_{ad}}$ corresponding to the adjoint eigenfunctions. Input includes the problem geometry factor "geom" (geom='slab' or 'peri' corresponds to $\alpha = 0$; geom='disk' to $\alpha = 1$; and geom='sphe' to $\alpha = 2$), and the differentiation, discretization point, and quadrature arrays, $\hat{\mathbf{A}}$, $\hat{\mathbf{x}}$, and $\hat{\mathbf{w}}$, respectively. The remaining parameters correspond directly to the terms in (3.5) and (3.6) or should be otherwise self-explanatory [99]. This function is normally called after `pd.m`. The maximum value *errtol* of the infinity-norm bound is used to discard inaccurate eigenfunctions; a negative value disables error control.

$[\mathbf{I_p}] =$ `wip`$(\hat{\mathbf{F}}, \hat{\mathbf{G}}, \hat{\mathbf{w}})$

The weighted inner product of two sets of discretized functions $\hat{\mathbf{F}}$ and $\hat{\mathbf{G}}$. This is one of the most heavily used subprograms since inner products are used in nearly every MWR step. The array of inner products $\mathbf{I_p}$ is computed as the vector dot product of the quadrature weight array $\hat{\mathbf{w}}$ with the term-by-term (Hadamard-Schur) product of all combinations of the discretized functions represented in $\hat{\mathbf{F}}$ and $\hat{\mathbf{G}}$. The number of rows in $\mathbf{I_p}$ corresponds to the number of trial functions in $\hat{\mathbf{G}}$; the columns correspond to the functions in $\hat{\mathbf{F}}$.

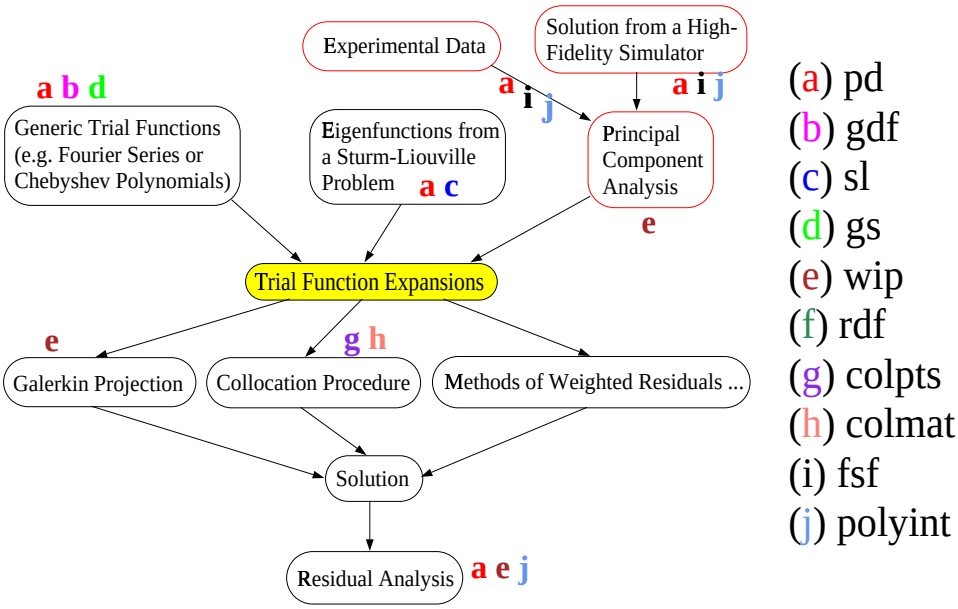

Figure 3.1: The MWRTOOLS functions as the fundamental operational elements on the computational framework (cf. Fig. 1.2) for Spectral Discretization Methods

These functions are the basic elements of a spectral numerical method. Their possible usage and the calling sequence in a method are illustrated in Fig. 3.1. The applications of the functions to practical Chemical Engineering problems are available in [29] and more complicated, industry-related problems have been reported in [30]. They are the simulation tools used in this dissertation for plasma simulation and subsequent model reduction studies.

3.2 Model Reduction Methodologies

3.2.1 Reduced Basis Discretization Methods

Principal Component Analysis (PCA)

Consider the ensemble $\{u^k\}$ of scalar fields, each being a function $u = u(x)$ defined on the domain $[0,1]$. In the context of Hilbert space $L^2([0,1])$, we want to find a basis $\{\phi_j(x)\}_{j=1}^{\infty}$ for a subspace of L^2 that is optimal for the data set in the sense that finite-dimensional representations of the form

$$u_N(x) = \sum_{j=1}^{N} a_j \phi_j(x)$$

describe typical member of the ensemble better than representations of the same dimension in any other basis.

The mathematical statement of optimality is that ϕ is chosen to maximize the averaged projection of u onto ϕ, suitably normalized:

$$\max_{\phi \in L^2([0,1])} \frac{< |(u,\phi)|^2 >}{||\phi||^2}$$

where $|\cdot|$, $||\cdot||$, $(\cdot)$, and $<>$ denote the modulus, L^2-norm, inner product, and ensemble average, respectively. This is a calculus of variations problem: to extremize $< |(u,\phi)|^2 >$ subject to the constraint $||\phi||^2 = 1$. The corresponding function for this constrained variational problem is

$$J(\phi) = < |(u,\phi)|^2 > \ - \lambda(||\phi||^2 - 1).$$

The necessary condition for extrema is that the functional derivative vanish for all variations $\phi + \delta\psi \in L^2([0,1])$, $\delta \in R$. This condition is expressed as

$$\frac{d}{d\delta}[J(\phi + \delta\psi)]_{|\delta=0} = 0.$$

Thus,

$$\begin{aligned} & \frac{d}{d\delta}[J(\phi+\delta\psi)]_{|\delta=0} \\ = \; & \frac{d}{d\delta}[< (u,\phi+\delta\psi)(\phi+\delta\psi,u) > -\lambda(\phi+\delta\psi,\phi+\delta\psi)]_{|\delta=0} \\ = \; & 2R_e[< (u,\psi)(\phi,u) > -\lambda(\phi,\psi)] \qquad (3.9) \\ = \; & 0 \end{aligned}$$

where the property $(f,g) = \int fg^* dx = (\int f^* g)^* = (g,f)^*$ of the (complex) L^2 inner product is used, $*$ denotes the complex conjugate, and R_e means taking the real parts. The quantity in the brackets of (3.9) may be written as

$$\begin{aligned} & < \int_0^1 u(x)\psi^*(x)dx \int_0^1 \phi(x')u^*(x')dx' > -\lambda \int_0^1 \phi(x)\psi^*(x)dx \\ = \; & \int_0^1 \left[\int_0^1 < u(x)u^*(x') > \phi(x')dx' - \lambda\phi(x) \right] \psi^*(x)dx \\ = \; & 0. \end{aligned}$$

Finally, since $\psi(x)$ is an arbitrary variation, the above condition reduces to an eigenproblem:

$$\int_0^1 < u(x)u^*(x') > \phi(x')dx' = \lambda\phi(x). \qquad (3.10)$$

The averaged autocorrelation function may be defined

$$< u(x)u^*(x') >= R(x,x').$$

It has been long realized that the difficulty of the PCA expansion is to solve the integral equation (3.10) to obtain the eigenvalues and eigenvectors (see e.g. [103]). An explicit solutions can be obtained only in rare cases. Traditionally, discrete versions of PCA have been used to obtain the solutions numerically, i.e., take time-sampled data, compute the autocorrelation matrix, and then find the eigenvalues and eigenvectors. The MWRTOOLS developed in this study

are capable of integrating arbitrary discrete functions. Therefore, the integral equation can be solved directly and accurately.

Properties of PCA

In this section, we describe some important PCA properties, which are directly related to the studies that follow. The properties can be identified during the procedure of proof for the mean square error due to the truncation of the empirical eigenfunctions.

The proof starts with the orthogonality of the eigenfunctions generated from the solution of the eigenvalue problem (3.10), i.e.,

$$\int_0^1 \phi_i(x)\phi_j^*(x)dx = \delta_{i,j}. \tag{3.11}$$

In general, an infinite number of $\phi_j(x)$ are required to form a complete solution, i.e., $u(x) = \sum_{j=1}^{\infty} a_j\phi_j(x)$ where $x \in [0,1]$. With the aid of orthogonality condition (3.11), the inversion operation of $u(x)$ gives

$$\int_0^1 u(x)\phi_j^*(x) = a_j. \tag{3.12}$$

The mean square error due to the truncation of function series is defined as

$$\begin{aligned}
\bar{\varepsilon}^2 &= < \int_0^1 (u(x) - u_N(x))(u(x) - u_N(x))^* dx > \\
&= < \int_0^1 \left(\sum_{j=N+1}^{\infty} a_j\phi_j(x) \right) \left(\sum_{j=N+1}^{\infty} a_j\phi_j(x) \right)^* dx > \\
&= \sum_{j=N+1}^{\infty} < a_j a_j^* >
\end{aligned}$$

because of (3.11). However,

$$< a_j a_j^* > = \int_0^1 \int_0^1 < u(x')u^*(x) > \phi_j(x')\phi_j^*(x)dx'dx$$

$$
\begin{aligned}
&= \int_0^1 \int_0^1 R(x,x')\phi_j(x')\phi_j^*(x)dx'dx \\
&= \int_0^1 \lambda_j \phi_j(x)\phi_j^*(x)dx \\
&= \lambda_j
\end{aligned}
$$

where (3.12), (3.10), and (3.11) have been used in steps one, three, and four, respectively. Therefore, the mean square error due to the truncation is

$$\bar{\varepsilon}^2 = \sum_{j=N+1}^{\infty} \lambda_j.$$

Or, in other words, the "energy" captured is the sum of the eigenvalues used in the solution expansion $u_N(x)$. The properties are summarized below:

1. The empirical eigenfunctions need not form a complete basis for L^2 norm space;

2. The PCA is optimal on average in the class of representations by linear superposition: the first n PCA basis functions capture more energy on average than the first n functions of any other basis;

3. The "energy" can be expressed in terms of the associated eigenvalues;

4. The PCA mode coefficients $a_j(t)$ are uncorrelated.

Method of Snapshots

The eigenvalue problem presented in (3.10) results in a $N \times N$ system matrix to be solved. In high dimensional simulations, the size of the data can be larger than the memory capacity of a computer. This is the reason why the original PCA methods did not receive the popularity expected in CFD literature. The

problem could be solved by the method of snapshots or strobes [24], which is the method used in this thesis. The method is described below.

Suppose that $\{u^i\}_{i=1}^M$ are the snapshots of the real field u and that the inner product on the N-dimensional vector space is denoted by $(\cdot,\cdot)$; that is the discretized version of the inner product in $L^2(\Omega)$. If ϕ is an eigenvector then

$$\phi = \sum_{k=1}^{M} a_k u^k$$

where the coefficients a_k remain to be determined. The N-dimensional eigenfunction problem analogous to (3.10) may then be written

$$\left(\frac{1}{M}\sum_{i=1}^{M} u^i \otimes u^i, \sum_{k=1}^{M} a_k u^k\right) = \lambda \sum_{k=1}^{M} a_k u^k \tag{3.13}$$

where $\otimes$ is the tensor product. The left-hand side of (3.13) may be rearranged to give

$$\sum_{i=1}^{M}\left[\sum_{k=1}^{M}\frac{1}{M}(u^i, u^k)a_k\right] u^i(x),$$

and the sufficient condition for the solution of (3.13) will be to find coefficients a_k such that

$$\sum_{k=1}^{M}\frac{1}{M}(u^i, u^k)a_k = \lambda a_i; \qquad i = 1, \cdots, M.$$

This is now an $M \times M$ eigenvalue problem for a_i. Note that the snapshots $\{u^i\}_{i=1}^M$ have to be linearly independent to generate M orthogonal eigenfunctions defined by a_i. Unfortunately, the method does not give a criterion in choosing M; therefore, numerical tests must be conducted to determine when a sufficiently "converged" basis is found.

3.2.2 Inertial Manifolds

It it well-known that long-term behavior of certain classes of infinite-dimensional systems and their evolutionary modeling equations exhibit low-dimensional dy-

namics. When applicable, the theory of inertial manifolds [20, 104] makes a solid connection between infinite- and finite-dimensional systems. Inertial manifolds are finite dimensional, positive invariant Lipschitz manifolds that contain the global attractor and attract all the orbits at an exponential rate. They are also physically and computationally relevant: the manifolds define an interaction law between the small and large wavelength components of a state variable described by distributions, i.e., the small wavelength modes are generally enslaved by the dynamics of the long wavelength modes. Computationally, they reproduce the coarse structure of the attractor while neglecting the fine details. Detailed simulations, stability and bifurcation calculations can be performed at a small fraction of the computational effort required to perform them on large-scale discretization of the original equations. Systems previously prohibitively large may become at least tractable.

The powerful theory, however, is new and not sufficiently general to cover all evolutionary equations. The existence of the inertial manifolds must be proved in a case-by-case basis. Since in only some cases, the Navior-Stokes equation (fluids type) has been proved to possess such a property, in this section only the practical method for constructing the approximate inertial manifolds is described.

Approximation Inertial Manifolds

Consider a general evolution equation

$$\frac{du}{dt} + Au + F(u) = 0$$

where u belongs to a Hilbert space. A is a linear operator along with the corresponding boundary conditions. If we denote the projection onto the span of the

first n eigenfunctions of A by P, and let $Q = I - P$, the equation can be split as

$$\begin{aligned} \frac{dp}{dt} + Ap + PF(p+q) &= 0 \\ \frac{dq}{dt} + Aq + QF(p+q) &= 0 \end{aligned}$$

where $p = Pu$ and $q = Qu$. The traditional (flat) Galerkin approximation assumes $q = 0$ by truncation. Under the assumption that the evolutionary equation has an inertial manifold which can be realized as the graph of a function $\Phi : PH \to QH$, the projection of the inertial form onto PH is given by

$$\frac{dp}{dt} + Ap + PF(p + \Phi(p)) = 0.$$

The objective then becomes to approximate Φ. There are at least four methods that are available for the determination of Φ [20]. The Sacker method is the simplest. It assumes

$$q(t) = \Phi(p(t)), \qquad \text{for t } \geq 0,$$

and by elimination we have

$$-\Phi'(p)\left(PF(p + \Phi(p)) + Ap\right) + A\Phi(p) + QF(p + \Phi(p)) = 0 \tag{3.14}$$

where Φ' is the first spatial derivative. In other words, the high frequency modes are slaved by the low frequency modes (the masters) through the relationship (3.14).

3.3 Nonlinear Analysis

3.3.1 Numerical Continuation

In many applications, a nonlinear system of equations must be solved. If the number of independent equations is equal to the number of unknowns M, the set of solutions usually consists of M discrete values. If there are M equations for $M+1$ unknowns, the solution usually consists of curves in $M+1$ dimensions. Continuation methods are used to approximate these curves by starting from a known point on a curve and then trying to find another nearby point on the curve. The repeating procedure can approximate a part of the curve.

There are two types of the situations that are candidates for solution by numerical continuation:

1. A system $\mathbf{F}(\mathbf{y}, \lambda) = \mathbf{0}$ depends on M unknowns $[y_1, y_2, \cdots, y_M]^T$ and an additional parameter λ. The behavior of the system is characterized by the change of the parameter.

2. A good initial guess for Newton-Raphson method for a nonlinear set of equation $\mathbf{F}(\mathbf{y}) = \mathbf{0}$ is not available. With a "simpler" system $\mathbf{G}(\mathbf{y})$ where a solution $\mathbf{y}_0$ is known and $\mathbf{x} = [\mathbf{y}, \lambda]^T$, a new system can be defined as

$$\mathbf{H}(\mathbf{x}) = (1 - \lambda)\mathbf{G}(\mathbf{y}) + \lambda\mathbf{F}(\mathbf{y}), \qquad \text{where} \quad \lambda \in [0, 1].$$

   Since $\mathbf{x}_0 = [\mathbf{y}_0, 0]^T$ is known, we can follow the curve from $\lambda = 0$ to $\lambda = 1$, which is the solution of $\mathbf{F}(\mathbf{y}) = \mathbf{0}$.

A predictor-corrector continuation technique, with an Euler-type predictor and Newton-Raphson corrector step [105, 106], is implemented in this thesis.

The algorithm is an arc length continuation consisting of three key elements: computation of tangent direction, Euler-predictor, and Newton-corrector. With a given starting point, the corresponding tangent direction is obtained using QR factorization of the Jacobian of the system with respect to all variables.

$$\mathbf{QR} = [\mathbf{H}'(\mathbf{x})]^{\mathbf{T}}$$

where $\mathbf{H}'(\mathbf{x})$ is the Jacobian of $\mathbf{H}(\mathbf{x})$ in the dimension of $M \times (M+1)$ and $\mathbf{x}$ is a column vector of M. The last column of the Q matrix is taken as the tangent $\mathbf{U}$. The next increment is predicted along the direction with a given initial step size Δs, i.e.,

$$\mathbf{z} = \mathbf{x} + \Delta s \ \mathbf{U}.$$

It serves as the initial guess to the Newton-corrector followed. The corrector solves the original system of equations as well as the predictor equation, i.e., the following nonlinear set of equations for "unknown $\mathbf{z}$" must be solved:

$$\begin{bmatrix} \mathbf{H}(\mathbf{z}) \\ \mathbf{U}^T(\mathbf{z}-\mathbf{x}) - \Delta s \end{bmatrix} = \mathbf{0}. \tag{3.15}$$

Once convergence is achieved, the $\mathbf{z}$ becomes the new $\mathbf{x}$. The marching along the solution curve continues by performing the QR factorization again for the new point.

3.3.2 Stability Analysis for a Large Scale AE/ODE System

Along the solution curve computed using the continuation technique, we are not only interested in solution convergence but also the stability of the solution for a given parameter. The discretized system from the PDE model consists a large set of AEs and ODEs, which makes manual analysis of stability hardly feasible.

In this study, a means of numerically folding the AE into the ODEs is utilized to obtain the necessary information with a minor cost of computation. It uses parts the augmented Jacobian computed while searching for the tangent direction in the continuation computations.

Consider a physical system described by the following vectors of equations:

$$\begin{aligned} \frac{d\mathbf{x}}{dt} &= \mathbf{P}(\mathbf{x}) \\ \mathbf{0} &= \mathbf{G}(\mathbf{x}) \end{aligned}$$

where $\mathbf{x}$ is the state variable vector, and $\mathbf{P(x)}$ and $\mathbf{G(x)}$ are the resultant algebraic equations of $\mathbf{x}$ from discretization and not explicit functions of time t. Linearized at a steady state and defining the deviation vector $\bar{\mathbf{x}} = \mathbf{x} - \mathbf{x_s}$, the entire system can be written as

$$\mathbf{C}\frac{d\bar{\mathbf{x}}}{dt} = \mathbf{A}\bar{\mathbf{x}}$$

where $\mathbf{A}$ is the Jacobian matrix for the system of $\mathbf{P(x)}$ plus $\mathbf{G(x)}$, and $\mathbf{C}$ is so the called "capacitance" or "mass" matrix. The $\mathbf{C}$ matrix is singular if a least one AE is involved. Thefore, the stability analysis cannot be performed by finding the eigenvalues of $\mathbf{C^{-1}A}$.

The technique to solve this problem is demonstrated as following. The matrix $\mathbf{A}$ is partitioned according to the structure of the system (AEs or ODEs):

$$\mathbf{A}\bar{\mathbf{x}} = \begin{bmatrix} \mathbf{A_{11}} & \vdots & \mathbf{A_{12}} \\ \cdots & \cdots & \cdots \\ \mathbf{A_{21}} & \vdots & \mathbf{A_{22}} \end{bmatrix} \begin{bmatrix} \bar{\mathbf{x}}_\mathbf{1} \\ \cdots \\ \bar{\mathbf{x}}_\mathbf{2} \end{bmatrix}.$$

where $\bar{\mathbf{x}}_\mathbf{1} \in R^n$ and $\bar{\mathbf{x}}_\mathbf{2} \in R^m$. The singular capacitance matrix problem now can be solved because the system is rewritten as

$$\frac{d\bar{\mathbf{x}}_\mathbf{1}}{dt} = \mathbf{A_{11}}\bar{\mathbf{x}}_\mathbf{1} + \mathbf{A_{12}}\bar{\mathbf{x}}_\mathbf{2} \tag{3.16}$$

$$\mathbf{0} = \mathbf{A_{21}}\bar{\mathbf{x}}_\mathbf{1} + \mathbf{A_{22}}\bar{\mathbf{x}}_\mathbf{2}. \tag{3.17}$$

Solving $\bar{\mathbf{x}}_\mathbf{2}$ from the equation (3.17) gives

$$\bar{\mathbf{x}}_\mathbf{2} = -\mathbf{A}_\mathbf{22}^{-\mathbf{1}}\mathbf{A_{21}}\bar{\mathbf{x}}_\mathbf{1}.$$

Substituting the $\bar{\mathbf{x}}_\mathbf{2}$ into equation (3.16) gives

$$\begin{aligned}
\frac{d\bar{\mathbf{x}}_\mathbf{1}}{dt} &= \mathbf{A_{11}}\bar{\mathbf{x}}_\mathbf{1} - \mathbf{A_{12}}\mathbf{A}_\mathbf{22}^{-\mathbf{1}}\mathbf{A_{21}}\bar{\mathbf{x}}_\mathbf{1} \\
&= (\mathbf{A_{11}} - \mathbf{A_{12}}\mathbf{A}_\mathbf{22}^{-\mathbf{1}}\mathbf{A_{21}})\bar{\mathbf{x}}_\mathbf{1} \\
&= \mathbf{B}\bar{\mathbf{x}}_\mathbf{1}.
\end{aligned}$$

The final set of the equations are pure ODEs and completely represent the original mixed system; therefore, the analysis of the eigenvalues of the "folded" matrix $\mathbf{B}$ reflect the stability of the original system.

Note that the Jacobian matrix $\mathbf{A}$ at a given steady state has been computed during the corrector step of the continuation method. Solving the nonlinear system (Eqn. 3.15) with the Newton-Raphson method involves computing the Jacobian of the system, which is

$$\begin{bmatrix} \mathbf{H}'(\mathbf{x}) \\ \mathbf{U}^T \end{bmatrix}. \tag{3.18}$$

The $\mathbf{H}'(\mathbf{x}) = [\mathbf{H}(\mathbf{y}), \frac{\partial \mathbf{H}(\mathbf{y})}{\partial \lambda}]$, where $\mathbf{y}$ is the vector of the true state variables. Since $\mathbf{H}(\mathbf{x}) = [\mathbf{P}(\mathbf{x}), \mathbf{G}(\mathbf{x})]^\mathbf{T}$, here, $\mathbf{H}(\mathbf{y}) = \mathbf{A}$.

3.3.3 Solution Convergence as Bifurcation Analysis Problem

The numerical continuation algorithm discussed in Section 3.3.1 can proceed around points where the Jacobian of the original system is singular. These degenerated points are called bifurcation points. They characterize the dramatic

changes of solution behavior, which is of paramount importance in practice (see [107, 108, 109, 110, 111] for types of bifurcations and rigorous definitions). It can be said that a thorough understanding of bifurcations is essentially limited to the logistic system [110] and low-dimensional ordinary differential equation systems. For partial differential equation systems, however, the solution convergence presents a fundamental problem due to the infinite-dimensions from discretization. Since the bifurcation analysis must base on a true (convergent) solution, this again emphasizes the importance of the accurate residual analysis using the software tools developed in this study. In this section, a simple reaction-diffusion problem in a cylindrically shaped catalyst is presented as an example.

In [112], two numerically converged solutions were identified by residual analysis for the modeling equation

$$0 = \nabla^2 C - \phi^2 C^2$$

subject to boundary conditions $\frac{dC}{dr}(r = 0) = 0$ and $C(r = 1) = 1$. One is the regular solution reported in the literature while the other is a spurious solution existing only numerically. These two solutions coalesce at a saddle-node bifurcation point. Figure 3.2 (left) shows the bifurcation diagrams corresponding to different levels of discretization. A magnified view for the case $N = 2$ is also provided in Fig. 3.3. Figure 3.2 (right) confirms the convergence of both solutions. For a given ϕ, both modeling equations residual norm decreases as N increases.

Exactly the same solution analysis will be applied to the DC discharge simulations shown later in the next Chapter. For a given applied voltage at the powered electrode, simulations with different levels of discretization can be per-

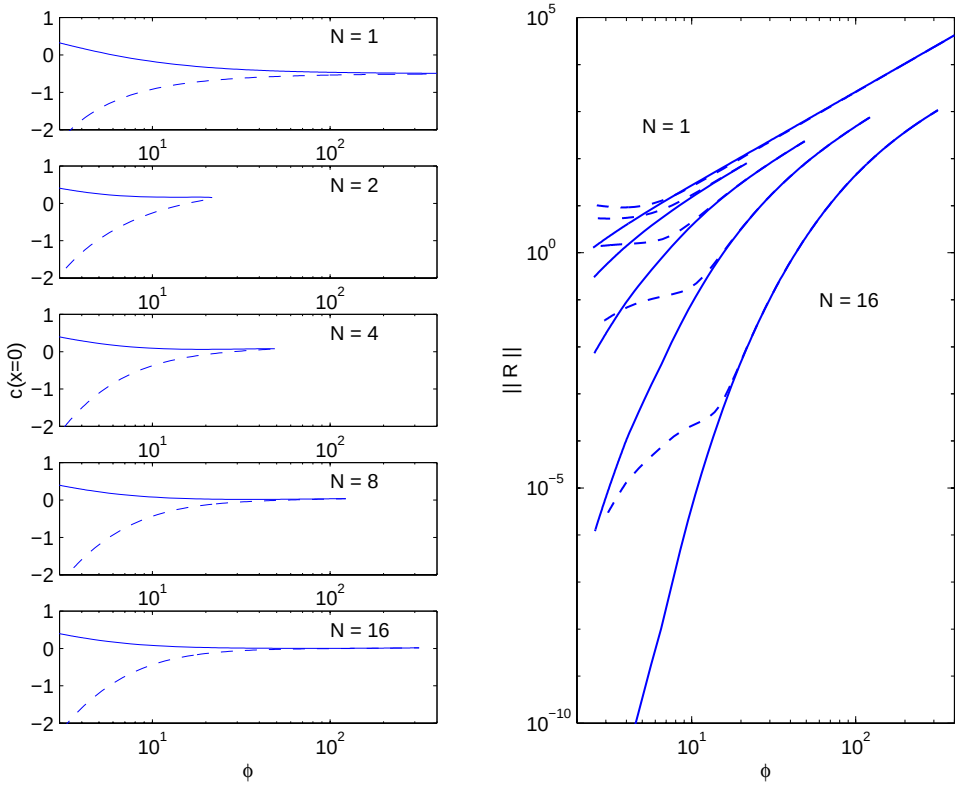

Figure 3.2: Continuation results for the collocation discretization method showing the reactant concentration at the catalyst pellet (left) and both solution residual norms (right) as a function for ϕ. Dashed curves represent spurious solutions and solid curves indicate true solutions. Saddle-node bifurcation point locations are $\phi \to \infty$ for $N = 1$, $\phi = 21.8634$ for $N = 2$, $\phi = 49.5011$ for $N = 4$, $\phi = 122.7844$ for $N = 8$, and $\phi = 318.2965$ for $N = 16$.

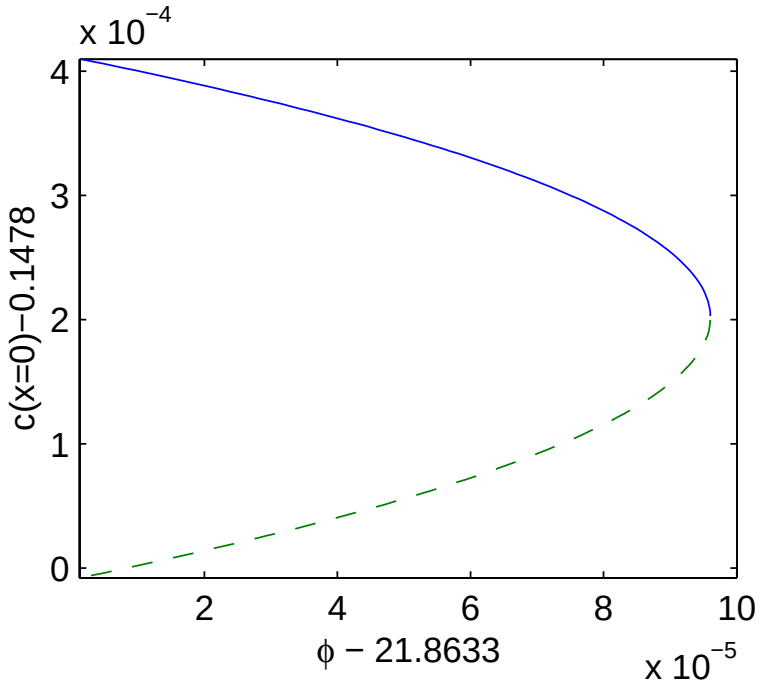

Figure 3.3: A magnified view of the solutions in the neighborhood of the saddle-node bifurcation point for the case $N = 2$.

formed. The weighted 2-norm of the model residual functions, formed by substitution of the interpolated results from the N point solution to the modeling equations, are plotted against the N to identify the convergent solution for a given set of operating conditions. The bifurcation plots for different levels of discretization can also be constructed in terms of the resulting total currents against the given applied voltages. As N increases, the solution curves approach an asymptotic limiting curve, which describes the change of the true solution along the controlled parameter.

Chapter 4

Simulation and Analysis – Computational Results

4.1 Direct Current Simulation and Analysis

A pseudospectral (PS) discretization method based on polynomial trial functions was used to solve a self-consistent direct current (DC) glow discharge model[1] to study the interplay between modeling assumptions and convergence of the numerical solution techniques. It was found that the assumed form of electron diffusivity temperature dependence strongly influenced the computed solutions. Simulation results demonstrate that the discretization method is an easy-to-implement, numerically stable technique capable of the resolution required in the plasma sheath regions.

This global basis function approach is presented as an alternative to localized basis function discretizations such as finite elements [5] and the block implicit

[1] The fluid type formulation for the plasma physics submodels [43] has been used successfully for simulating glow discharges with results comparable to those produced by Monte Carlo particle simulation techniques [11].

implementation of finite differences [69]. It is motivated by the excellent convergence property of the PS method [113], the transparency of its implementation to discretizing partial differential equations (PDEs) and their boundary conditions (BCs), and the capability of appropriately selected trial functions to resolve required the details of the thin sheath regions.

The focus on simulating the DC glow discharge was motivated by two facts. The first was the availability of previous DC discharge modeling studies in the literature; this provides a basis for comparing the different numerical techniques. While relatively simple compared to a full etch system model, the DC glow discharge model retains physical features that make the full model highly nonlinear and its solution spatially stiff. Secondly, the DC solution can serve as the reference state for accelerating convergence to a time-periodic steady state, which is a common problem for commercial etch reactors. The numerical techniques demonstrated in this study can be extended to analyze, design, and optimize a full plasma processing reactor.

4.1.1 Modeling Equations

The smallest set of self-consistent continuum modeling equations describing a glow discharge consists of four partial differential equations and their associated boundary conditions: Poisson's equation, electron and ion continuity equations, and the electron energy balance. These equations can be solved for potential field, electron and ion number densities, and electron temperature. Electric field strengths, particle fluxes, and ionization rates may then be computed as secondary quantities from these solutions.

The model used in this report is similar to Graves and Jensen's [5]. The

boundary conditions and parameters for an argon-like gas were also taken from [5]. One difference, however, are electron flux $\vec{j_e}$ and electron diffusivity D_e definitions

$$\begin{aligned} \vec{j_e} &= -D_e \vec{\nabla} n_e - \mu_e n_e \vec{E} \\ D_e &= \mu_e \frac{k_b T_e}{e} \end{aligned} \tag{4.1}$$

where n_e, μ_e, and T_e are electron number density, mobility, and temperature, respectively. $\vec{E}$ is the electric field strength, k_b is the Boltzmann constant, and e is the unit charge. The $\vec{j_e}$ definition is the same as the one in Chapter Two except the diffusivity is a function of electron temperature. This expression for temperature-dependent diffusivity implicitly assumes $T_e \nabla n_e \gg n_e \nabla T_e$, an assumption valid for the results presented in this study. The dimensionless modeling equations for DC simulation are listed below in the order of Poisson, electron and ion continuity, and electron energy equations. While only one-dimensional discharge simulations are reported in this study (so $\nabla = \zeta \frac{\partial}{\partial Z}$ and $\nabla^2 = \zeta^2 \frac{\partial^2}{\partial Z^2}$), the following nondimensional model is modified according to the new $\vec{j_e}$ and valid for two- and three-dimensional system geometries:

$$\begin{aligned} \nabla^2 \Phi &= -\epsilon(u_+ - u_e) \\ \vec{\nabla} \cdot \vec{J_e} &= k_2 u_e \\ \vec{\nabla} \cdot \vec{J_+} &= k_2 u_e \\ \vec{\nabla} \cdot \vec{Q_e} &= \varepsilon_e \vec{J_e} \cdot \vec{\nabla} \Phi - k_2 u_e. \end{aligned}$$

The four dimensionless variables are defined as $\Phi = \frac{V}{V_0}$, $u_e = \frac{n_e}{n_0}$, $u_+ = \frac{n_+}{n_0}$, and $T = \frac{T_e}{T_{e0}}$. The auxiliary equations for electron, ion, and electron energy fluxes,

and ionization rate coefficient are

$$\begin{aligned}
\vec{J}_e &= -\frac{T}{D}\vec{\nabla}u_e + P_e u_e \vec{\nabla}\Phi \\
\vec{J}_+ &= -\left(\frac{1}{D_{e+}}\right)\vec{\nabla}u_+ - \left(\frac{P_+}{D_{e+}}\right)u_+\vec{\nabla}\Phi \\
\vec{Q}_e &= \frac{5}{3H_i}\left(-\frac{Tu_e}{D}\vec{\nabla}T + T\vec{J}_e\right) \\
k_2 &= D_a e^{-\frac{E}{T}}.
\end{aligned}$$

The boundary conditions at $z = 0$ (grounded electrode) are

$$\begin{aligned}
\Phi &= 0 \\
u_e &= 0 \\
\nabla u_+ &= 0 \\
\frac{5}{3}\nabla T - \varepsilon_e H_i \nabla\Phi &= 0,
\end{aligned}$$

and at $z = 1$ (powered electrode)

$$\begin{aligned}
\Phi &= -\Phi_{DC} \\
-\left(\frac{T}{D}\right)\nabla u_e + P_e u_e \nabla\Phi &= \left(\frac{\gamma P_+}{D_{e+}}\right)u_+\nabla\Phi \\
\nabla u_+ &= 0 \\
T &= T_c.
\end{aligned}$$

The values and definitions of dimensionless parameters are given in Table 4.1. The gas properties and scaling parameters are listed in Table 4.2.

4.1.2 Numerical Methods

Discretization

The modeling equations and boundary conditions are discretized with a weighted residual method that combines elements of collocation and pseudospectral meth-

Symbol	Definition	Value	Symbol	Definition	Value
ϵ	$\frac{en_0R^2}{\epsilon_0 V_0}$	406	D_{e+}	$\frac{D_e}{D_+}$	10^4
D	$10^6/(\mu_e \frac{k_b T_{e0}}{e})$	5	E	$\frac{E_i}{k_b T_{e0}}$	24
D_a	$\frac{k_{io}R^2 N}{D_e}$	1.83×10^6	ε_e	$\frac{eV_0}{H_{ei}}$	29.5
P_e	$\frac{\mu_e V_0}{D_e}$	92	H_i	$\frac{H_{ei}}{\frac{3}{2}k_b T_{e0}}$	10.4
P_+	$\frac{\mu_+ V_0}{D_+}$	9200	ζ	$\frac{R}{L}$	1.44

Table 4.1: Dimensionless parameter values and definitions.

ods. If each state (Φ, u_e, u_+, or T) is represented by a linear combination of trial functions $\psi_i(z)$ defined over $0 \leq z \leq 1$, i.e.,

$$u(z) = \sum_{i=1}^{N} c_i \ell_i(z),$$

one set of residual functions over the domain and another set of functions at the boundaries can be defined with the partial differential equations (PDEs) and boundary conditions (BCs), respectively. The residuals then are minimized to determine the solution.

In this study, the building blocks of a Lagrangian interpolation polynomial are selected as the trial functions (see the definition in (3.3) for ℓ_i). An (N-1)th order Lagrangian interpolation polynomial $u_{(N-1)}$ can be defined by a linear combination of N polynomials of order $N-1$, i.e., $u_{(N-1)} = \sum_{i=1}^{N} c_i \ell_i(z)$. The coefficient c_i represents the value of the state $u(z)$ at the discretization point z_i because by definition (3.3), $\ell_i(z_j) = 1$ if $i = j$ and is equal to zero if $i \neq j$. Since the ℓ_i are continuous and differentiable over the entire domain, explicit formulas for derivatives of the state $u(z)$ up to order $(N-1)$ can be obtained that are valid for all $0 \leq z \leq 1$. Once the discretization points z_i are specified, differentiation becomes a matrix operation, i.e., $\frac{du}{dz} = \mathbf{Ac}$ and $\frac{d^2u}{dz^2} = \mathbf{Bc}$ where

Symbol	Description	Value
L	interelectrode spacing	$3.525cm$
R	electrode radius	$5.08cm$
N	neutral species density	$2.83 \times 10^{16} cm^{-3}$
n_0	charge particle reference density	$4 \times 10^{9} cm^{-3}$
V_0	reference voltage	$460V$
T_{e0}	reference electron temperature	$1eV$
D_+	ion diffusivity	$10^2 \frac{cm^2}{sec}$
μ_e	electron mobility	$2 \times 10^5 \frac{cm^2}{V \cdot sec}$
μ_+	ion mobility	$2 \times 10^3 \frac{cm^2}{V \cdot sec}$
E_i	ionization rate activation energy	$24eV$
H_{ei}	ionization enthalpy loss	$15.578eV$
γ	secondary electron coefficient	0.046
V_{DC}	direct current voltage	$77.4V$
k_{io}	ionization rate prefactor	$2.5 \times 10^{-6} \frac{cm^3}{sec}$
T_{ec}	electron temperature at cathode	$0.5eV$

Table 4.2: Gas physical properties and glow discharge system physical dimensions.

the elements A_{ji} and B_{ji} for the differentiation matrices are defined as (3.4) for $N = M$ and $a = 1$, and $\mathbf{c} = [c_1, c_2, \cdots, c_N]^T = [u(z_1), u(z_2), \cdots, u(z_N)]^T$. An additional advantage of using Lagrangian building blocks as trial functions is that the function value and derivatives of a Lagrangian polynomial can be evaluated with recurrence formulas [34].

Theoretically, any discretization grid can be used to construct the Lagrangian interpolation polynomial. However, the interpolated solutions between discretization points are accurate only if the individual building blocks behave well between the points. Lagrangian polynomials constructed with uniformly spaced discretization points will pass through all construction points exactly but will oscillate between points with increasing amplitude near the interval end points ($z = 0, 1$). It has been shown [101] that spacing of the discretization points according to a quadratic weight function will suppress the spurious oscillation near the ends. In this study, the discretization positions are chosen as the Chebyshev extrema distribution as suggested by Fornberg [101],

$$z_j = \frac{1}{2}\left(\cos\left(\frac{(j-1)\pi}{N-1}\right) + 1\right), \qquad j = N, N-1, \cdots, 1. \tag{4.2}$$

In the limit of the endpoints, the Chebyshev node spacing is inversely proportional to the square of the total number of points used. This suggests that these polynomial trial functions can resolve features with length scales of order N^{-2} in the sheath regions while retaining good convergence properties in the bulk phase (see the discussions in [113], page 40). Having defined the discretization points and the discrete differentiation operators, the four modeling PDEs are discretized to give $4(N-2)$ nonlinear equations plus eight linear and nonlinear equations from the boundary conditions.

Numerical Continuation

Plasma simulations are well-known to be highly sensitive to small disturbances and so poor initial guesses are unlikely to converge to the solution. A predictor-corrector continuation technique, with an Euler-type predictor and Newton-Raphson corrector step, is first used to find a converged, self-sustained solution corresponding to a low voltage drop, and then to study the solution dependence on the voltage drop. The general continuation technique has been discussed in Section 3.3.1. Following is a description for the implementation on this plasma simulation and analysis.

In the first step of this procedure, a uniform ionization rate was used in place of the temperature dependent terms $k_2 u_e$. This is similar to simulation of photoionization. Converged solutions were easily obtained with several iterations. Starting from this set of solution profiles, the ionization reaction term was gradually modified in the numerical continuation procedure until a self-sustained solution was obtained. The homotopy expression (see item two of Section 3.3.1) replacing the ionization term was (uniform rate) $\times (1-s) + (k_2 u_e) \times s$ with s as the continuation parameter. The continuation technique was started at $s = 0$, corresponding to the uniform reaction rate, and proceeded to the self-sustained solution at $s = 1$. Once a self-sustained solution was reached, the applied voltage at the powered electrode was used as a continuation parameter to study the solution dependence on the voltage drop across the system.

Different uniform ionization rates were chosen as initial continuation points to validate the converged, self-sustained solutions. All resulted in the same self-sustained solution. Solutions reported in the next section were found by starting with an ionization rate of 1×10^{-3} and a dimensionless voltage drop of 0.1521.

Once a self-sustained solution was reached, the voltage drop was varied as the continuation parameter for values up to 0.1683 (corresponding to 77.4 $volts$).

4.1.3 Computational Results and Discussions

Results for a Representative DC Case

A self-sustained solution for the one-dimensional model with a DC exciting source and fifty discretization points ($N = 50$) is shown in Fig. 4.1. The electric field and currents computed from the basic variables V, n_e, n_+, and T_e are also shown. The results corroborate with those previously reported in the literature [5, 69]. The discharge characteristics such as the plasma potential, cathode fall region, and the flat bulk phase are clearly shown in Fig. 4.1a. The electric field strength at both electrodes is nonzero and it is much greater at the powered electrode ($z = 1$) than at the grounded electrode ($z = 0$); thus ions bombard both electrode surfaces and with greater intensity at the powered electrode. The fact that the electric field passes through zero increases the difficulty of numerical simulation. It suggests that the "convection" changes direction in the center of the reactor and makes some traditional techniques, such as upwind finite difference methods, harder to implement.

The bulk phase and both sheaths can be seen in the particle number density profiles (Fig. 4.1b). Results obtained by numerical continuation show that if the voltage drop is increased, the difference between the two densities becomes smaller. Simulation results show that the electron number density in the cathodic sheath can be four orders of magnitude lower than that of the bulk phase. The electron density in the sheath, however, cannot be treated as zero because the sheath region is the source of charged particle generated by the electron impact

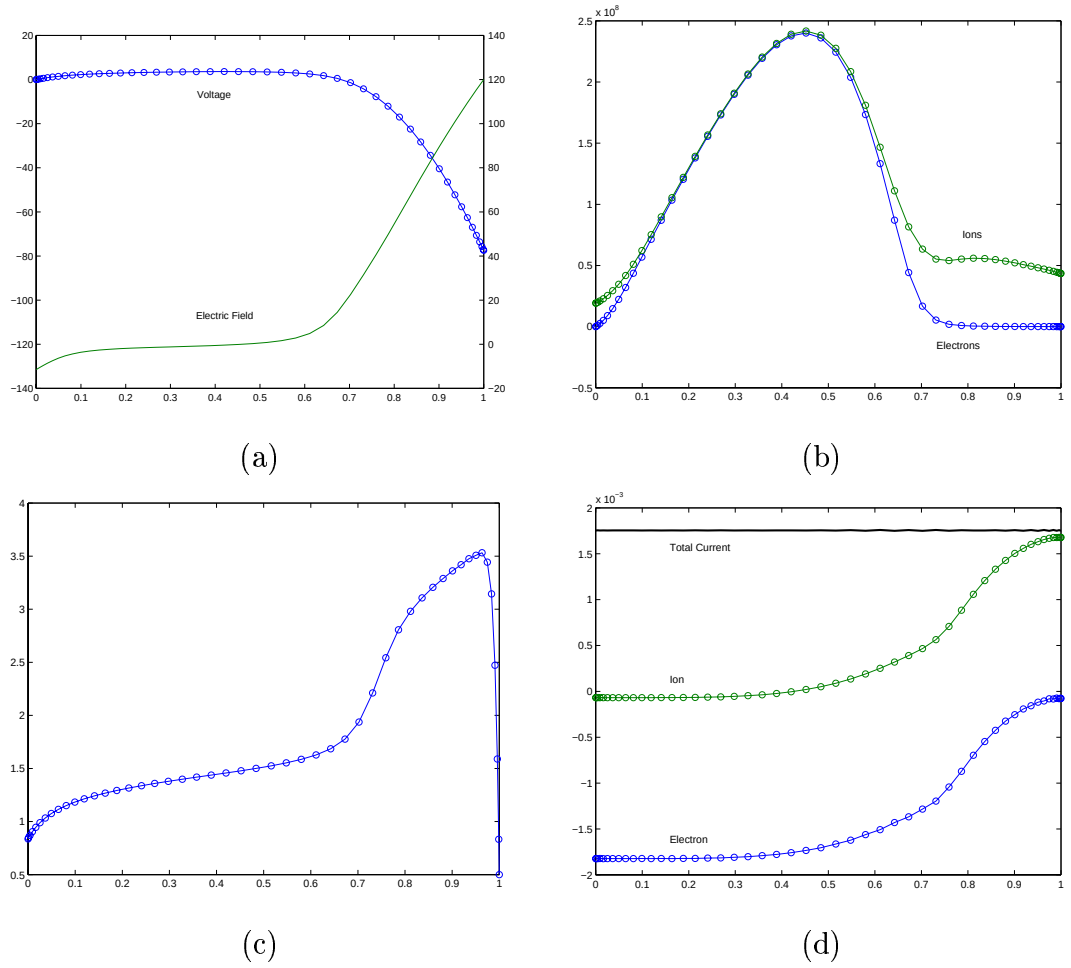

Figure 4.1: Self-sustained DC solutions. (a) voltage (V on the left axis) and electric field ($\frac{V}{cm}$ on the right axis), (b) electron and ion number densities (cm^{-3}), (c) electron temperature (eV), and (d) electron and ion currents ($\frac{mA}{cm^2}$) versus dimensionless position.

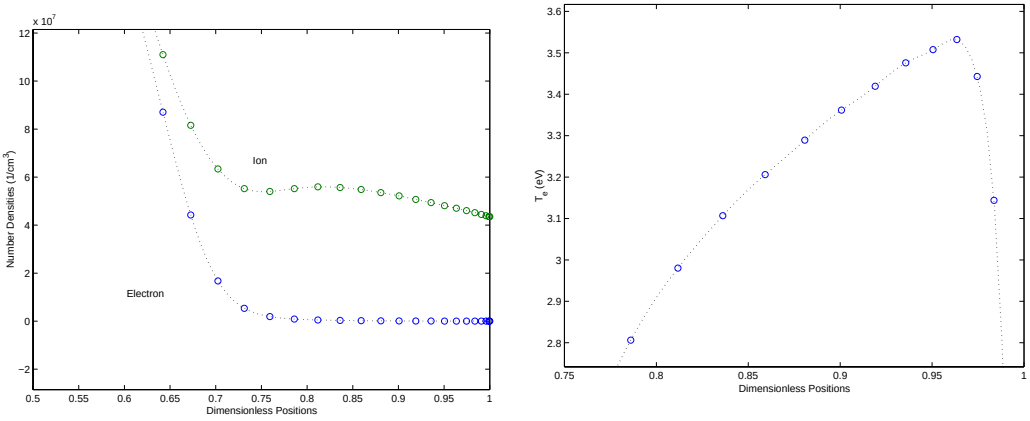

(a) (b)

Figure 4.2: The magnified profiles after interpolation: (a) shows electron and ion number densities near the powered electrode, and (b) is the electron temperature profile near the powered electrode. The circles represent the solutions at the collocation points while the dots represent the points obtained after reinterpolation with Lagrangian polynomials.

reaction. Zero density here means no reactions. If during the simulation the electron density profile oscillates around zero as a result of numerical errors generated by the discretization method, the adjacent regions of positive and negative ionization rates would cancel each other. To compensate for "negative" reaction values while retaining a significant total charged particle generation rate, the "positive" reaction node values increase, leading to oscillations in the electron temperature curve. Our interpolated curves in Fig. 4.2 show no such spurious oscillation. The mechanism described above is one of several responsible for the numerical stiffness encountered in solving these simulation problems - note that this problem can be encountered regardless of the discretization method.

The total current shown in Fig. 4.1d is constant with respect to z: this com-

putation provides an independent check of the validity of the DC simulation. Electrons are the major current carrier near the grounded electrode while ion current dominates near the powered electrode. The electron current at $z = 1$ does not vanish because of the secondary electron emission boundary condition. The electron temperature profile (Fig. 4.1c) also gives the electron energy distribution. Electron temperature increases dramatically near the powered electrode because electrons quickly gain energy from the electric field and are accelerated inwards. The curve then quickly dips down due to strong electron cooling by the highly endothermic ionization reactions. The bulk phase temperature is rather flat and becomes flatter with increasing voltage drop. The small temperature drop near the grounded electrode is attributable to electrons diffusing against the electric field.

Figure 4.3 shows the same results broken down to individual terms of the modeling PDEs and associated solution residuals. In Fig. 4.3a, the electric field gradient faithfully reflects the space charge; thus, the Poisson equation is completely satisfied. Fig. 4.3b shows that the major balancing forces in the electron continuity equation are diffusion and electric drift. The reaction is comparably smaller and may indicate that this discharge is sustained via the secondary electron emissions, i.e., the γ mode discharge. Fig. 4.3c shows that the two major terms are electric drift and ionization in the ion continuity equation. The diffusion term is small as expected. Finally, Fig. 4.3d shows a more complicated interaction among four forces. Different terms have different significance locally. The ohmic heating reflects the local electron heating effect. The residuals and the computed boundary conditions are also shown in Table 4.3. As shown in the table, all boundary conditions are satisfied to computational round-off error.

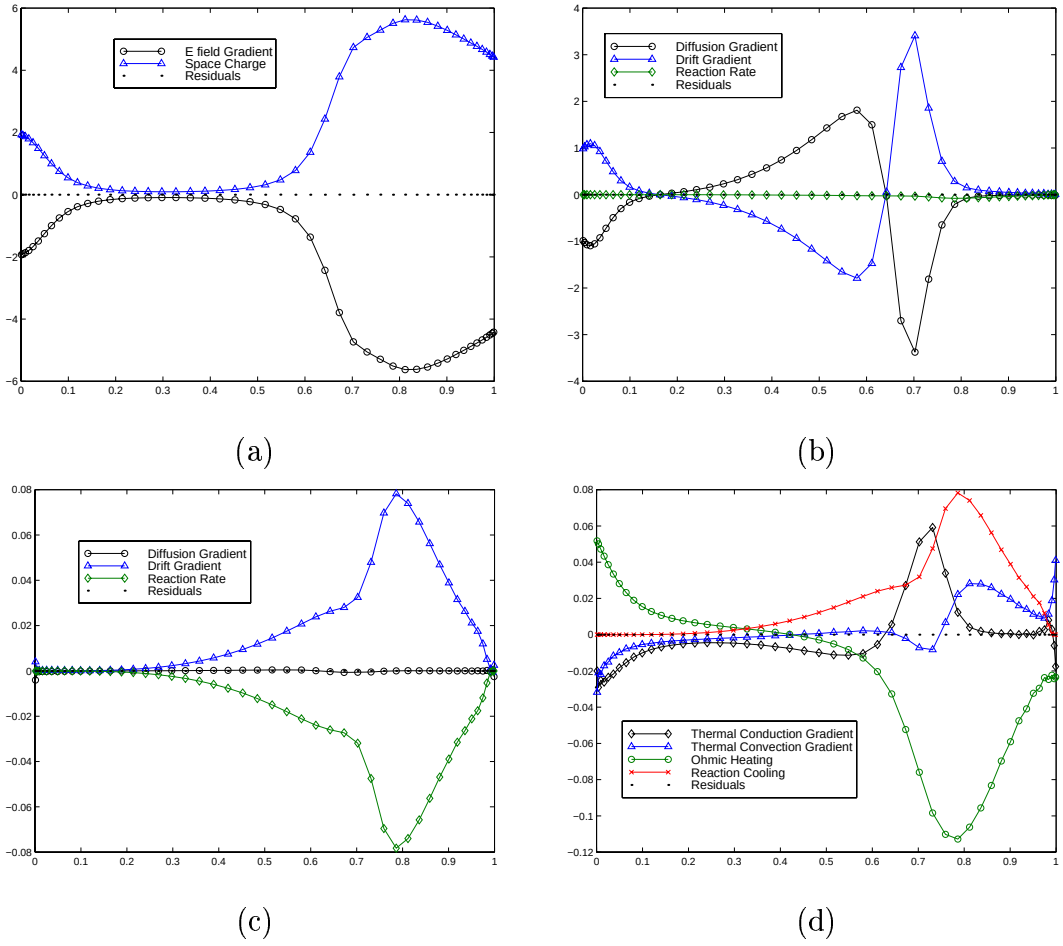

Figure 4.3: The individual terms in modeling equations with their associated residuals. (a) to (d) are for Poisson equation, electron particle balance, ion particle balance, and electron temperature balance, respectively. The values are in dimensionless form and in terms of dimensionless position.

	At $z = 0$	Residual
V	$\Phi = 0$	9.7047×10^{-28}
u_e	$u_e = 0$	-1.0768×10^{-27}
u_+	$\nabla u_+ = 0$	-7.9277×10^{-16}
T	$\frac{5}{3}\nabla T = 26.1517$ $-\varepsilon_e H_i \nabla\Phi = -26.1517$	2.3448×10^{-13}
	At $z = 1$	Residual
V	$\Phi = -0.1683$	0
u_e	$-\left(\frac{T}{D}\right)\nabla u_e = 1.2924 \times 10^{-8}$ $P_e u_e \nabla\Phi = -4.2510 \times 10^{-4}$ $\left(\frac{\gamma P_+}{D_{e+}}\right) u_+ \nabla\Phi = -4.2509 \times 10^{-4}$	-2.2630×10^{-19}
u_+	$\nabla u_+ = 0$	0
T	$T = 0.5$	0

Table 4.3: The residuals of the boundary condition definitions.

Temperature-Dependent Electron Diffusivity

Plasma fluid models based on the "diffusion-drift" approximation assume constant diffusivities, which is valid when local acceleration and convection acceleration (inertia) in the momentum balance for each species are negligible (see [11]), and each species temperature is constant. The last assumption is reasonable for heavy species (such as ions) due to their effectiveness of energy exchange with background species, but may not be valid for electrons. Many RF simulations rely on this assumption, while reported DC simulations either take diffusivity temperature dependence explicitly into account [5] or are formulated in terms of the three moment approach [69] and so cannot be directly compared with the diffusion-drift modeling equations. To test the effects of this assumption on the solution behavior, simulations were performed with equation (4.1) and were compared to results obtained with a constant $D_e = 10^6$ $(\frac{cm^2}{sec})$.

As shown in Fig. 4.4, the temperature dependence of the electron diffusivity significantly influences the solutions. For constant D_e, the number densities are one order of magnitude smaller (compared with Fig. 4.1b). The density difference is larger; thus, the bulk phase voltage profile is not flat. The currents are also smaller than the temperature dependent case. One of the most significant differences, however, is seen in the behavior of the electron temperature as a function of voltage drop. It was found that when the voltage value at $z = 1$ reaches approximately 80 $volts$, the temperature at the grounded electrode reaches zero and continues below zero for larger voltage drops when a constant D_e is used.

This observation can be explained by examining the electron energy equation and the solution curves of Figs. 4.1 and 4.4. Near $z = 0$, both the ohmic heating $(-\varepsilon_e \vec{J}_e \cdot \vec{\nabla}\Phi)$ and reaction cooling $(k_2 u_e)$ terms contribute to electron cooling.

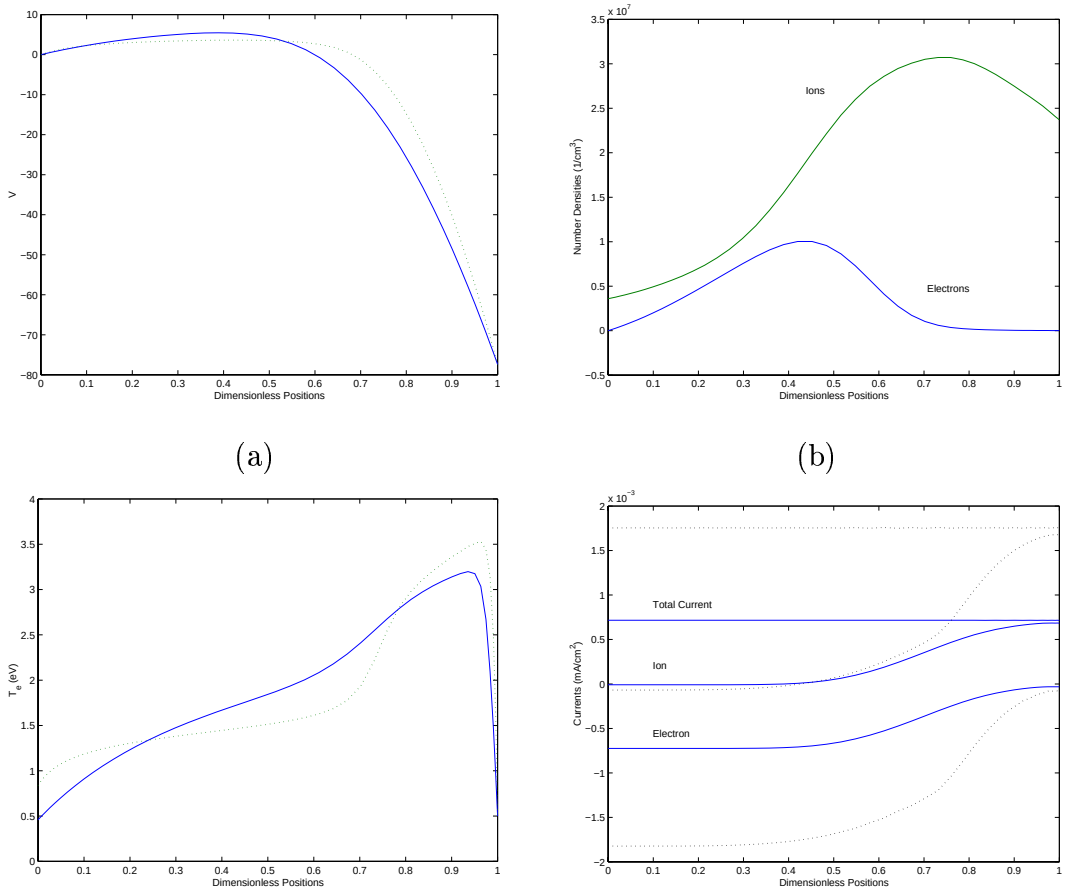

Figure 4.4: The test results for constant electron diffusivity (solid curves): (a) voltage profile (V), (b) electron and ion densities (cm^{-3}), (c) electron temperature (eV), and (d) electron and ion currents ($\frac{mA}{cm^2}$) versus dimensionless position. The dashed curves represent results obtained with electron-temperature dependent diffusivity.

Because the electron current has a significant magnitude at $z = 0$ suggests diffusion dominates in this region. Since the electron current, and, hence, electron cooling increases with applied voltage drop, there is no mechanism to prevent T_e from reaching and passing through zero when D_e is constant. However, if D_e is proportional to T_e (see equation (4.1)), as the voltage drop increases, the electron diffusion terms become smaller owing to a smaller T_e, thus correcting the unrealistic cooling effect.

4.1.4 Solution Convergence Analysis

There have been many papers reporting plasma simulations using a variety of different numerical techniques. The majority concentrate on the results of model prediction or the speed of computations. There is virtually no literature reporting the convergence of the solutions under a given operating condition. The importance of the solution convergence has been emphasized in [112]. The existence of a solution has to be formally judged by convergence analysis, because a "visually correct" result may only exist under a specific method of discretization. Furthermore, a numerically converged but physically nonexisted solution can play an important role for the stability analysis of the physical solution. In Fig. 4.5, the weighted 2-norms of the model residual functions, formed by substitution of the interpolated 160 point result from the N point solution to the modeling equations, are plotted against the number of collocation points used. The operating condition is the same as before except the voltage drop is 72 volts. The monotonic decreasing trend for the four residual norms identify the convergent solution.

The parametric study also has practical interest. According to scaling laws

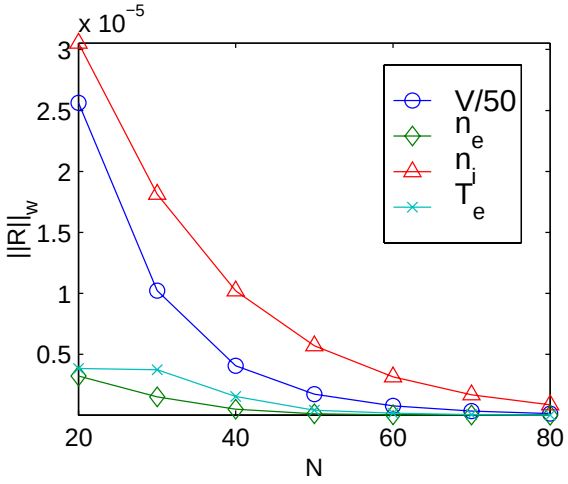

Figure 4.5: DC solution convergence analysis for $\Delta V = 72$ volts case.

in previous studies [15, 114], the total current and voltage drop have a linear relationship for glow discharges. The relation can be easily derived with the discretized particle density equations and electron boundary equation at the powered electrode. Since the the current is all conductive (no time-dependent displacement current), the total current is directly proportional to the ion current at the powered electrode. In Fig. 4.6, the converged solution (N=80) appears to have two slopes and a transition around 73 volts. The steeper-slope region corresponds to the primary discharge (α mode) while the other is sustained due to the secondary electrons (γ mode discharge) [62].

Another interesting analysis shown in the Fig. 4.6 is the convergence of the bifurcation curve. The sold curves represent the stable solutions (with all positive eigenvalues) while the dashed curves represent the unstable solutions. According to the figure, the stability appears to depend on the number of collocation points. As the number of the collocation points increases, the solution curve approaches an asymptotic limiting curve, which describes the change of *true* solution along

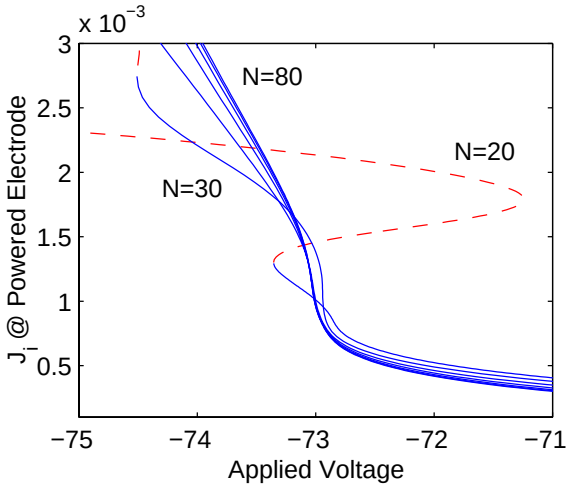

Figure 4.6: DC solution analysis for voltage drop 71-75 volts.

the controlled parameter. Therefore, the bifurcation analysis should be based on the convergent solution (N=80 or beyond), i.e., there are no true bifurcation points within this parameter range. The importance of the convergence analysis illustrated in Fig. 4.5 is proved again in this example.

Figure 4.7 shows the same analysis as Fig. 4.6 except with a wider parameter range. As expected, the higher the applied voltage, the more difficult it is to obtain solution convergence with a given number of collocation points. The solution breakdown point depends on the number of terms in the trial function expansion, and shows the difficulty of plasma simulation in the high voltage region. For higher degree simulations and practical applications, a model reduction technique must be utilized.

4.1.5 Concluding Remarks

A pseudospectral discretization method based on globally defined polynomial trial functions was used to solve a self-consistent DC glow discharge physics

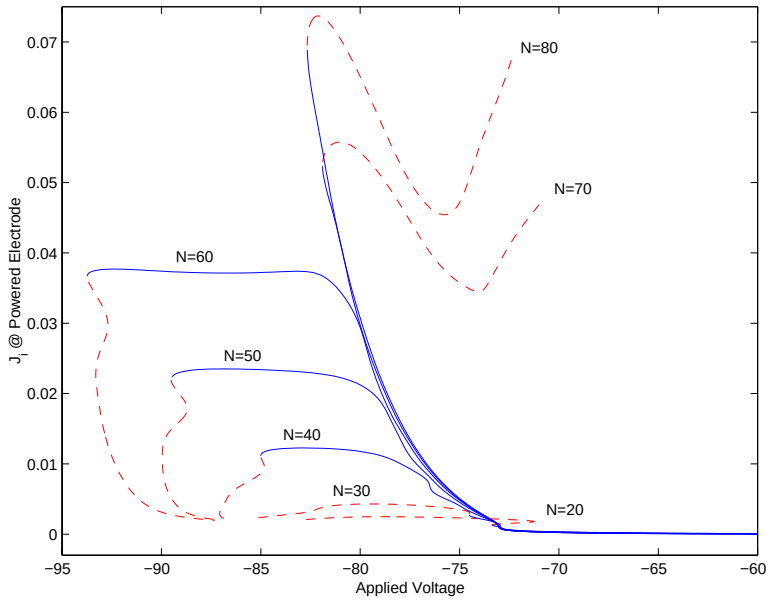

Figure 4.7: DC solution analysis for voltage drop 60-95 volts.

submodel. Starting from a uniformly ionized solution, a continuation technique was used to find the initial self-sustained solution and to study the voltage-drop dependence of the solution. Numerical analysis of the residuals showed that the modeling equations and the boundary conditions were satisfied to the computational round-off error. The excellent interpolation results and the lack of oscillations in the states and flux quantities are an indicator of the numerical stability of the discretization method. The strong influence of electron temperature on the solution profiles in terms of a temperature-dependent electron diffusivity was also investigated. It was found that the formulation for the diffusivity used in this thesis may serve as a simple but more accurate representation than the constant D_e typically used in RF simulation. Finally, the true convergent solutions can be identified by weighted residual analysis that can be conveniently performed using MWRtools.

The PS method introduced in this study was investigated as an alternative approach to the FDM and FEM discretization techniques used in many plasma processing simulations. The discretization procedure was shown to be straightforward to implement; in addition to this advantage, the method also does not require choosing finite element boundary locations, it simplifies stability analysis computations, powerful methods for assessing the accuracy of computed solutions exist, and convergence analysis by energy methods can be conveniently computed (see the examples in [101], Appendix H). The techniques demonstrated in this thesis can be extended to the analysis, design, and optimization of a full plasma processing model.

4.2 Radio Frequency Simulation and Model Reduction

Alternating currents (AC), such as radio frequency (RF) and microwave, have been the primary excitation sources in low temperature plasma processing. Equipment using a DC source results in a serious surface charging problem while an AC source can sustain a plasma with lower energy input without such problems [36]. In this section, we report on numerical techniques for computing the RF solution and for demonstrating model reduction results for the RF discharge. As the first test of plasma model reduction, the model and boundary conditions are slighted modified: the electron diffusivity is assumed to be independent of electron energy and the boundary conditions are made to be homogeneous. The same spatial discretization as the DC simulation is used. The discretized sets of ordinary differential equations are integrated in time using the MATLAB stiff ode solver

`ode15s`, a solver that is based on an implicit integration method [2]. The detailed simulation data then are used to generate the empirical eigenfunctions using the proper orthogonal decomposition. The Galerkin projection method is used with the reduced basis functions to simulate the dynamics of the reduced model. The performance and limitations of the reduced-basis discretization methods are also discussed.

4.2.1 Modeling Equations

The model used by Passchier and Goedheer [7, 115] is adopted in this RF simulation and model reduction study, except that a separate ion effective electric field due to the inertia force is included. The major differences from the model used in the previous DC simulations are

1. Electron diffusivity is a constant in both electron flux and thermal conductivity. The fundamental results will not be changed by this assumption [7, 76]. Therefore, the electron and ion fluxes are described by the same form of diffusion-drift expression.

2. In the electron energy balance equation, the electron density and temperature is combined as the so-called electron energy density, i.e., $n_e(\frac{3}{2}k_bT_e) = n_e\epsilon_e = \omega_e$.

3. Argon ionization coefficient based on the experimental data fitting by Richards and co-workers [76] is used.

[2] Discretizing the system of modeling equations leads to a set of algebraic equations (AEs) (from the Poisson's equation) and ordinary differential equations (ODEs). However, the linear AEs can be folded into the ODEs to form a new set of ODEs suitable for a general ODE solver.

After nondimensionalization, the following one-dimensional model is used for RF simulation and model reduction.

$$\begin{aligned}
\frac{\partial E}{\partial z} &= \epsilon(u_+ - u_e) \\
T\frac{\partial u_e}{\partial \tau} + \frac{\partial J_e}{\partial z} &= k u_e \\
T\frac{\partial u_+}{\partial \tau} + \frac{\partial J_+}{\partial z} &= k u_e \\
T\frac{\partial \omega}{\partial \tau} + \frac{\partial Q}{\partial z} &= -\chi J_e \cdot E - k u_e H_i
\end{aligned}$$

The dimensionless variables are defined as $\tau = \nu t$, $u_e = \frac{n_e}{n_0}$, $u_+ = \frac{n_+}{n_0}$, and $\omega = \frac{T_e n_e}{T_{e0} n_0}$. The auxiliary equations for voltage field, electron, ion, and electron energy fluxes, and ionization rate coefficient are

$$\begin{aligned}
E &= -\frac{\partial \Phi}{\partial z} \\
J_e &= -\frac{\partial u_e}{\partial z} - P_e u_e E \\
D_{e+} \cdot J_+ &= -\frac{\partial u_+}{\partial z} - P_+ u_+ E \\
Q &= -\frac{5}{3}\left(\frac{\partial \omega}{\partial z} + P_e \omega E\right) \\
k &= \begin{cases} D_a(\epsilon_e - 5.3)e^{\frac{-4.9}{\sqrt{\epsilon_e - 5.3}}}, & \text{for} \quad \epsilon_e \geq 5.3\text{eV}; \\ 0, \text{otherwise.} \end{cases}
\end{aligned}$$

The boundary conditions at $z = 0$ (grounded electrode) are

$$\begin{aligned}
\Phi &= 0 \\
u_e &= 0 \\
\nabla u_+ &= 0 \\
\omega &= 0
\end{aligned}$$

and at $z = 1$ (powered electrode)

$$\begin{aligned} \Phi &= \Phi_{DC} + \Phi_{RF} \sin(2\pi\tau) \\ u_e &= 0 \\ \nabla u_+ &= 0 \\ \omega &= 0. \end{aligned}$$

For the electron number density boundary conditions, the secondary electrons were not considered as in the DC case. The effect of maintaining the discharge due to the extra electrons is expected to be less than one-tenth of the ionization rate [7]. However, we then cannot expect the effect from the γ discharge such as shown in Figs. 4.6 and 4.7 or in [62] to result in a plasma sustained by secondary electrons. The zero electron boundary conditions result in zero boundary conditions for energy density.

The values and definitions of dimensionless parameters are given in Table 4.4. The gas properties and scaling parameters are listed in Table 4.5. The operating condition and system configuration are selected so that computed results can be compared with the literature [55, 62, 6, 116].

Symbol	Definition	Value	Symbol	Definition	Value
ϵ	$\frac{en_0L^2}{\epsilon_0 V_0}$	723.8	D_{e+}	$\frac{D_e}{D_+}$	3×10^4
D_a	$\frac{k_{io}L^2N}{D_e}$	955.9	χ	$\frac{eV_0}{\frac{3}{2}k_bT_{e0}}$	100
P_e	$\frac{\mu_e V_0}{D_e}$	25	H_i	$\frac{H_{ei}}{\frac{3}{2}k_bT_{e0}}$	15.578
P_+	$\frac{\mu_+ V_0}{D_+}$	3500	T	$\frac{\nu L^2}{D_e}$	45.2

Table 4.4: Dimensionless parameter values and definitions for RF simulation.

Symbol	Description	Value
L	interelectrode spacing	$2cm$
n_0	charge particle reference density	$4 \times 10^{10} cm^{-3}$
V_0	reference voltage	$100V$
$\frac{3}{2} k_b T_{e0}$	reference electron temperature	$1eV$
D_+	ion diffusivity	$40 \frac{cm^2}{sec}$
μ_e	electron mobility	$3 \times 10^5 \frac{cm^2}{V \cdot sec}$
μ_+	ion mobility	$1.4 \times 10^3 \frac{cm^2}{V \cdot sec}$
H_{ei}	ionization enthalpy loss	$15.578eV$
V_{DC}	direct current bias	$0V$
V_{RF}	RF forcing amplitude	$40V$
ν	RF forcing frequency	$13.5MH_z$
k_{io}	ionization rate prefactor	$8.7 \times 10^{-9} \frac{cm^3}{sec \cdot eV}$

Table 4.5: Gas physical properties and glow discharge system physical dimensions for RF simulation.

4.2.2 Computational Results and Discussions

Detailed simulations of argon RF discharge for various operating conditions have been reported [5, 6, 11, 55, 62, 116]. The purpose of this simulation is to show that the same results can be conveniently reproduced by the spectral numerical method using MWRTOOLS, and the simulation data will be used in the model reduction to generate the empirical eigenfunctions.

Figure 4.8 shows an example result using 100 discretization points for the particle densities, voltage fields, and electron temperature over one RF cycle. The operating condition was 1 torr gas pressure and 40 volts RF forcing amplitude. The simulation initial conditions consisted of flat particle density profiles; ion density was one thousandth of the target mean value and electron density was the tenth of that of the ions. Different initial values for voltage and electron energy were tried; these simulations all converged to the same solution. The solution was considered to be converged onto a limit cycle when the 2-norm of the difference between the beginning and end of the cycle for the state variables passed below a preselected value of 10^{-8}. The convergence required 2000 RF cycles and took 57 hours on a Sun Ultra 10 workstation.

Snapshots of the solution profiles are shown at four phases of an RF cycle in Fig. 4.8. The solution plots qualitatively agree with many reported physical phenomena characteristic of argon plasmas [5, 11]. The ion density is essentially constant over the cycle while electrons instantly respond to the voltage modulation. The plasma sheath thickness reaches 0.3 cm near the cathode, and the plasma potential is approximately 20 volts. Voltage distribution is flat in the bulk, showing the quasineutral property of the plasma, and is steep in the sheaths. Thus, as shown in the electric field distribution plot, the major electric

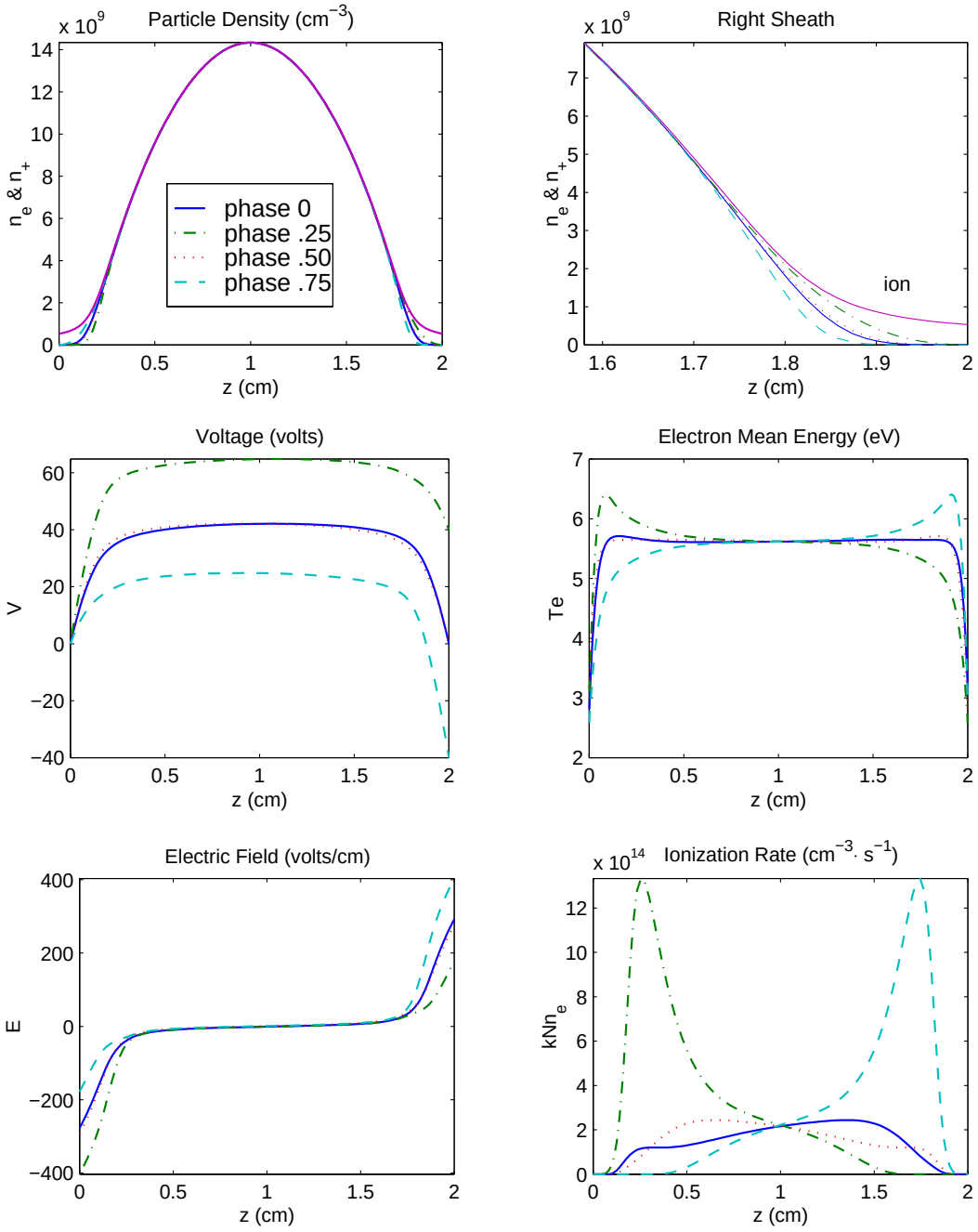

Figure 4.8: Argon RF discharge solution at 1 torr pressure, 2 cm interelectrode spacing, and 293 K.

driving force is in the sheath. Electron energy is also modulated with the electrode voltage variations. The mean energy distribution is flat in the bulk and has maximum magnitude inside the momentary cathode sheath. Since the ionization rate depends on both the electron number density and the electron energy, the ionization peak occurs at the momentary cathode sheath/bulk boundary (compare the energy and the ionization rate plots), where the number of high energy electrons is sufficient to undergo a significant electron-impact ionization reaction.

The plots of electrons, ion, displacement, and total currents shown in Fig. 4.9 quantitatively agree with the total current reported in [62] despite the omitted effect of secondary electrons. Since the generation of the secondary electrons contribute to sustaining the discharge, the total current needed to maintain the discharge should be lower. Qualitatively, the plot of plasma current profiles also reflects the physics of the discharge. Ion currents are almost straight in the bulk phase due to the ambipolar diffusion effect (see Fig. 4.8). However, they are modulated inside the sheaths. The ion current only contributes 10% of the total current. Electrons are the major current carrier in the bulk phase while displacement currents dominate inside the sheaths. The sum of electron, ion, and displacement currents is a constant due to the current conservation law, which can be easily derived using the Poisson's equation, particle continuity equations, and the definition of displacement current (2.28). The current characteristic reflects the capacitive nature of the argon discharge, i.e., the sheaths behave like resistors while the bulk phase behaves like a capacitor. They are connected sequentially as a unit in the entire electrical circuit.

The simulation results demonstrate both the correct physics of the discharge

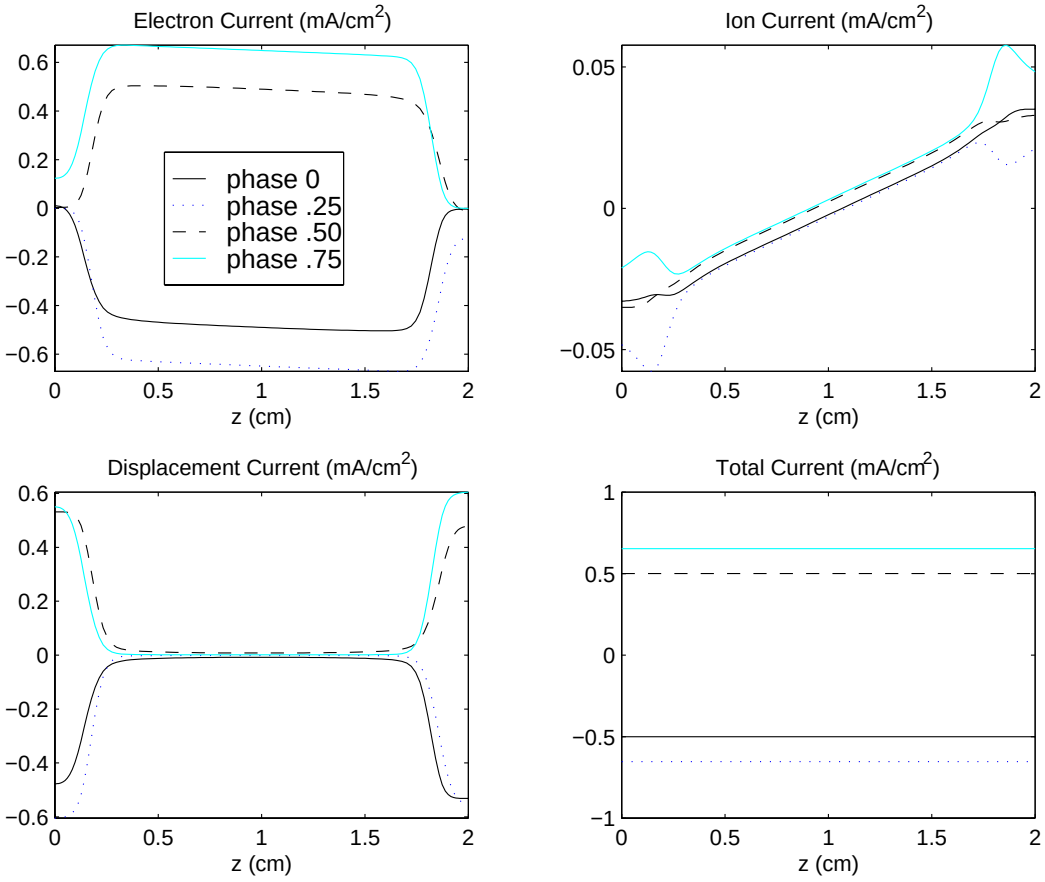

Figure 4.9: Currents in the RF simulation

model and the challenges of the solution techniques. As shown, the primary characteristic of plasma is the thin boundary layers. What distinguishes it from other computational fluid dynamics (CFD) computations is that the solution is contingent on resolving the boundary layers. Independent of what numerical techniques are used, there should be sufficient discretization points to resolve the interphases and the sheaths. Insufficient resolution of these regions causes problems in terms of solution convergence. The solution shown in Fig. 4.8 is produced by Chebyshev collocation method with 100 collocation points. This "coarse" grid solution is interpolated with 250 Gauss-Labotto points and is substituted into the modeling equations to obtain the residual functions. The 2-norms of the residual functions are plotted in Fig. 4.10 in terms of number of collocation points used.

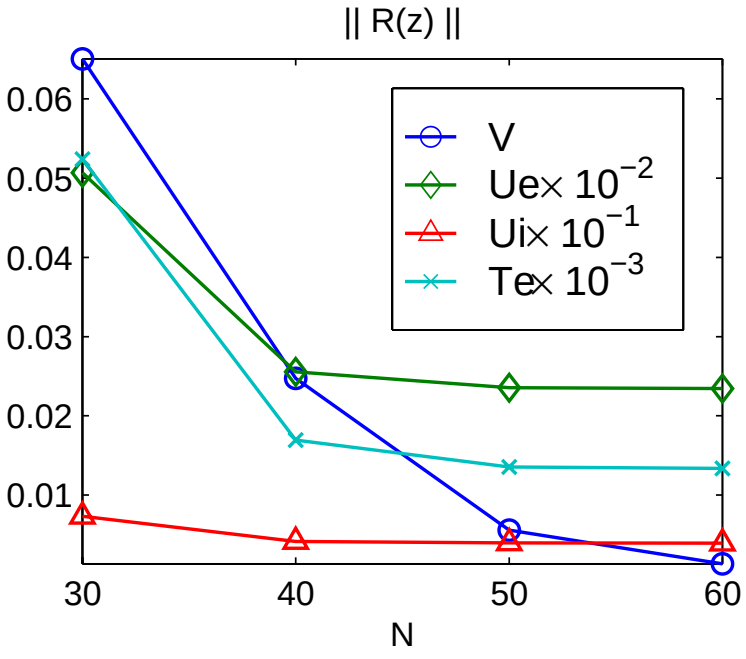

Figure 4.10: Residual analysis for RF simulation.

The residual analysis (Fig. 4.10) confirms that the solution under this operating condition is convergent. Since Poisson equation is an ordinary differential equation, as the number of collocation points increases, the residual norm approaches zero. For the other three partial differential modeling equations, the residual norms approach constants because of the nonzero time derivative functions. The residual plot also serves as a good criterion for the trade-off between computational efficiency and solution convergence.

4.2.3 Optimal Discretized Basis Functions from PCA

The high efficiency of model reduction results from extracting the uncorrelated characteristics of the existing solutions using the proper orthogonal decomposition technique. The principal eigen-modes of the solution are retained and are used to spectrally discretize the original, nonlinear modeling equations. Since each of the empirical eigenfunctions is better tailored to capturing the spatial features of the solution, relatively few trial functions are needed to reconstruct the dynamics. The fewer number of modes used in the simulation, the faster the computations regardless the computing languages or facility. The cut-off number of the eigenfunctions to be used can be conveniently determined using the eigenvalue associated with each eigenfunction. While the mutual orthogonal eigenfunctions represent the activity in each independent direction, the eigenvalues express how much energy the solution spends in that direction. In this section, the empirical eigenfunctions are generated from the solution data obtained in last section, and the performance of the reduced model is demonstrated in the next section.

Figure 4.11 shows the eigenfunctions and the scaled "solution snapshots"

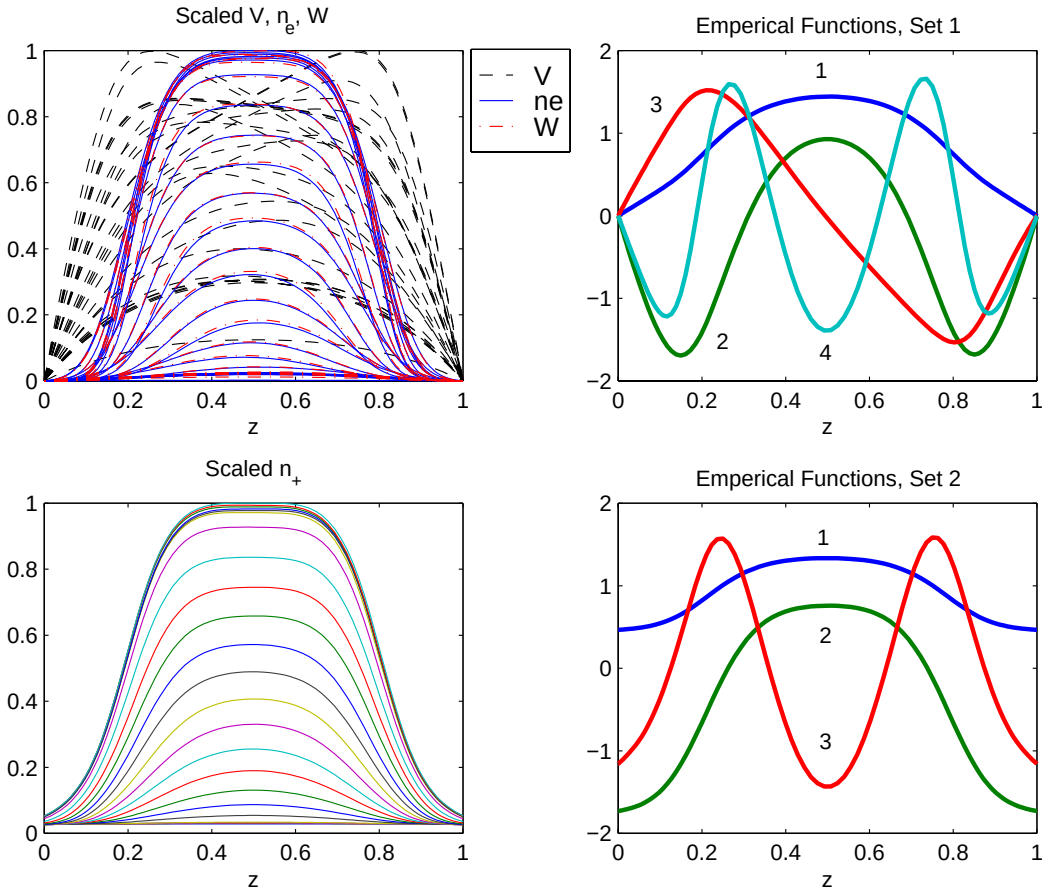

Figure 4.11: Snapshots (left) and empirical eigenfunctions (right) generated using the proper orthogonal decomposition.

used to generate them. The purpose of this model reduction study is to capture the dynamic behavior that includes the start up transient and the limit cycle behavior (e.g. [27]). It was found that the best snapshot data were collected from a transient simulation starting from the stated initial condition to a state near the limit cycle. In this study, the first 60 RF cycles were used.

Instead of generating four sets of empirical eigenfunctions, the solution data are classified into two sets according to their types of boundary conditions. The first set corresponds to states with zero boundary conditions, including electron

density, energy density, and voltage (after folding the applied voltage at the power electrode into the Poisson equation). The three sets of "solutions" after scaling are shown in the top left of the Fig. 4.11. The stacking of the solution snapshots in PCA procedure exploits the possible correlations among the three state variables. The second set of the functions corresponds to the ion density profile, which must satisfy zero first derivative boundary conditions. The classification is reasonable when one considers the problems of generating a set of functions satisfying both zero and zero first derivative boundary conditions.

Table 4.6 shows the percentage of the accumulated energy (eigenvalues) associated with two sets of eigenfunctions. Both sets have a dominant first mode, which captures the major characteristics of the solution dynamics. The second and the third modes tailor the solution profiles to describe the finer structure. Accurate representation of the ion dynamics using three modes can be expected since they accumulate nearly 100% of the total energy. However, the situation may not be true for the states corresponding to the first set functions. The importance of this difference will be illustrated and discussed in the next section.

set 1		
mode	λ_i	
1	35.22	95.97%
2	1.24	99.34%
3	0.17	99.81%
4	0.06	99.97%

set 2		
mode	λ_i	
1	14.22	93.91%
2	0.90	99.84%
3	0.02	99.99%

Table 4.6: Accumulated energy captured.

4.2.4 Reduced Model Simulation

In this section, the RF plasma model is solved with the Galerkin projection method using the empirical eigenfunctions shown in the Fig. 4.11. Each state variable is assumed to be the linear combination of suitable eigenfunctions. The mode coefficients are determined by projecting the residual function onto the corresponding trial functions. The boundary conditions are automatically satisfied because the eigenfunctions generated by PCA already satisfy the boundary conditions. What is different from the previous collocation method is each computational step involves a projection by quadrature. It was found that 60 point quadrature integration of these eigenfunctions can reach essentially the same accuracy as 100 point quadrature. Therefore, to enhance the computational efficiency, 60 discretization points were used for the reduced order functions in this study.

Figure 4.12 shows the Galerkin projection solution corresponding to the 60th cycle (left column) using the empirical eigenfunctions for the same model and operating conditions as the full simulation. The number of empirical trial functions used to approximate the ion density profile is three while the truncation number for the other state variables was set as eight. The right column shows the original simulation data at the same cycle for comparison. The prediction of the state variables is accurate with only minor errors visible for electron density inside the sheaths. The ion density and currents, which are of primary importance in plasma processing applications, are particularly accurate when compared to the detailed simulations. The floating point operations used in the reduced model is *one percent* of the original full simulation using Chebyshev collocation method (see the comparison on Table 4.7).

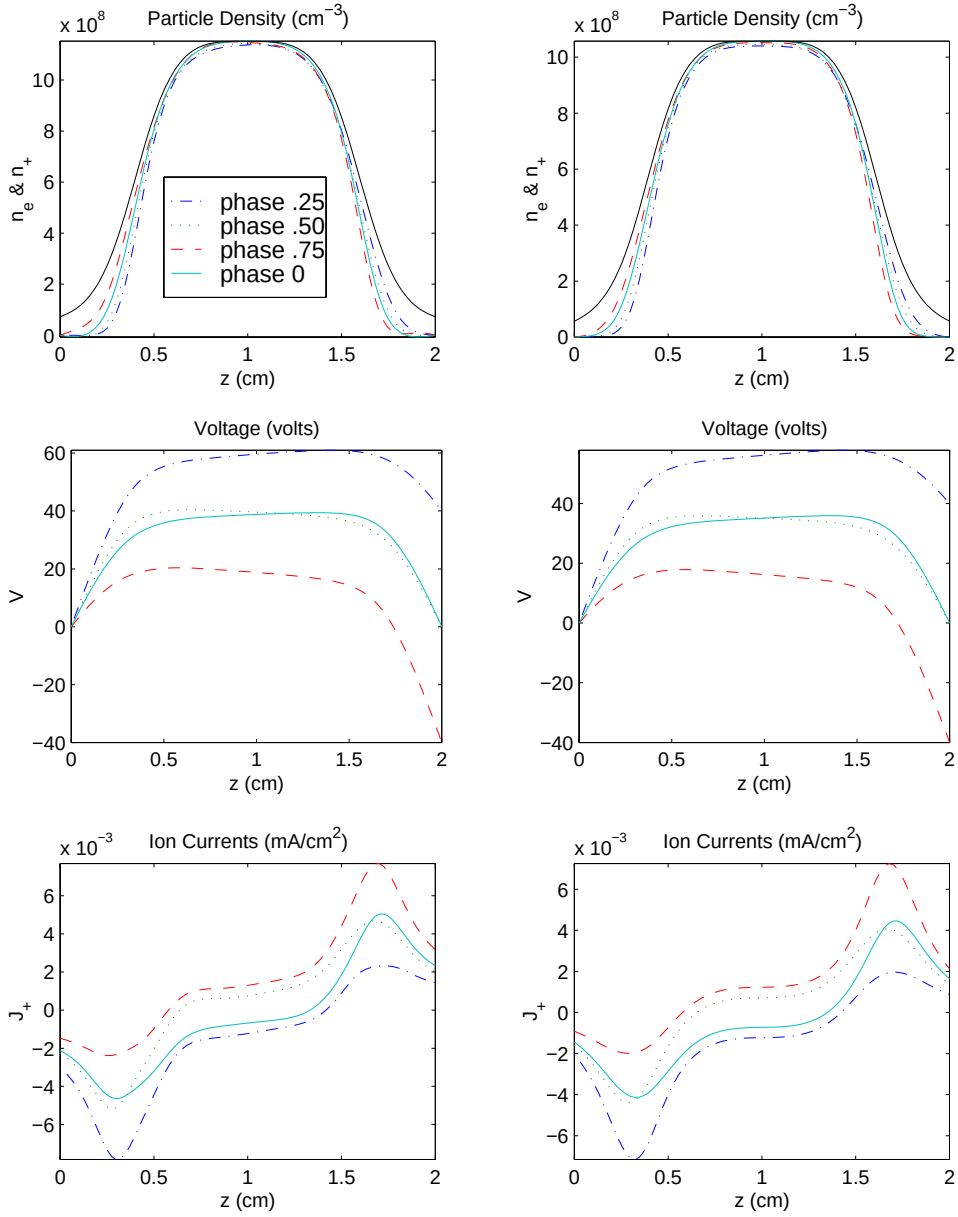

Figure 4.12: Performance of the reduced model. The left column shows the solutions during the 60th RF cycle for the reduced model while the right column corresponds to the original solution snapshots as the same points in time.

	Number of Equations	Floating Point Operations
Original Model	106 AEs and 98×3=294 ODEs	$\approx 10^8$ per time step
Reduced Model	8 AEs and 8×2+3=19 ODEs	$\approx 10^6$ per time step

Table 4.7: Reduction of number of equations and floating point operations required for the reduced model simulations. Each RF cycle consists of four time steps.

4.2.5 Reduced Model Simulator Limitations

The reduced model prediction of electron current is not as accurate as the ion currents shown in Fig. 4.12. Figure 4.13 shows a comparison of predicted electron current between the original and reduced model. The smooth original electron

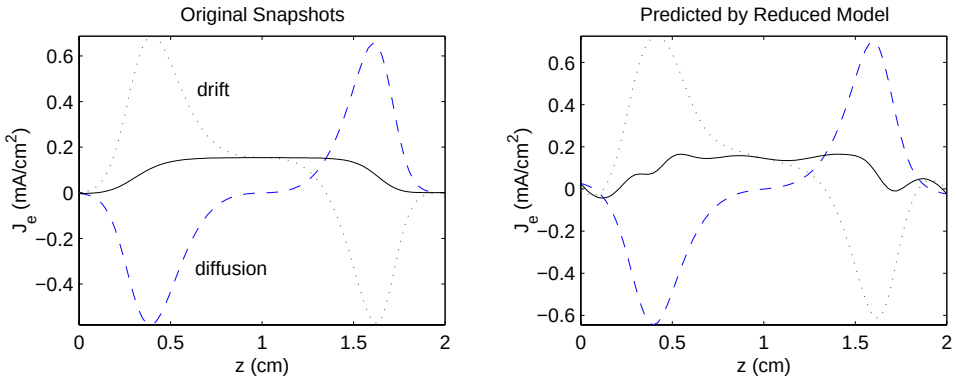

Figure 4.13: Limitations of the reduced model.

total current is due to the smooth diffusion and drift fluxes. However, in the prediction produced by the reduced model, the smooth diffusion and drift currents cannot construct a smooth electron current unless the number of eigenmodes is increased to 12. It suggests the sensitivity of the electron current to the tail of the eigenmodes (as discussed in the previous section). Therefore, we conclude that the number of eigenmodes needed in practical applications of model

reduction methods does not depend solely on the analysis of the accumulated eigenvalues (Table 4.6).

Although the electron current is not the major concern in plasma processing applications, the prediction accuracy of this quantity can be improved via two methods. The first is to use the nonlinear Galerkin method. Additional trial functions can be used for simulations in this framework by slaving them to the primary modes. In other words, dynamics of the system is dictated by the master modes while the slaved modes are assumed to be at steady state with respect to the current state of the masters. The second method for improvement is to use the partial least-squared projection (PLS) to generate an additional set of empirical eigenfunctions. PLS generates a set of basis functions by minimizing the norm of the difference between the original flux and the target flux. Therefore, even though the predicted state variables might not be accurate, the corresponding secondary quantities may be closer to the original dynamics.

4.2.6 Concluding Remarks

The physics of an argon plasma under 1 torr and 40 volts RF forcing was simulated using a Chebyshev collocation method, and the data were used to produce the reduced order model. The detailed simulation results correctly reflected the physics of the argon plasma under consideration. The residual analysis confirmed the solution convergence, which is a unique contribution of this work. The novel model reduction results of plasma simulation were also reported. It was found that the set of empirically determined eigenfunctions can be separated into two groups according to their type of boundary conditions. With this approach, it was found that the state variables can be accurately predicted using the empiri-

cal eigenfunctions. However, it was also found that the prediction of the electron current by the reduced model is not ideal. Although this quantity may not be the primary concern of plasma practitioners, two methods of improvement were suggested.

Chapter 5

Conclusions and Further Studies

5.1 Concluding Remarks

In this thesis, the fundamentals of plasma processing modeling were reviewed, and argon discharge simulations were performed using global spectral numerical methods. DC discharge simulations demonstrated the difficulties of plasma simulation and manifested the importance of residual analysis for determining whether the computed values constituted converged solutions. RF discharge simulation and model reduction studies further demonstrated the need for new numerical tools and a coherent framework for simulation and model reduction. This computational framework was established and coded using MATLAB. The contributions of this dissertation are summarized as follows:

- Fundamental numerical issues were addressed, motivated by practical simulation needs:
  - to provide an "open" framework for simulation/model reduction/solution analysis;

  - the techniques have been coded as MATLAB software by our research team;
  - A web site for the software was developed and can be found at http://www.ench.umd.edu/software/MWRtools;
    the software has been downloaded by 100 research groups since June 1998.

- A model reduction framework was established based on the requirements that it be:
  - compatible with experiment/process data and other simulator output;
  - rigorously tested on the difficult problem of RF plasma simulations;
  - applied to a range of spatially distributed systems including plasma etch, chemical vapor deposition (CVD), rapid thermal processing (RTP), and chemical vapor infiltration (CVI) in related studies by other research group members.

- New computational results include:
  - using global basis functions for plasma simulations;
  - a assessment of solution convergence on DC and RF plasma models;
  - plasma reactor model reduction with PCA based trial functions.

5.2 Further Studies

The value of this dissertation is primary due to the construction of the simulation framework and the software tools to implement simulation and model reduction

studies. There are many studies that can build on this work:

Improvements in MWRtools Implementation

Performance of some toolbox functions can be improved by using different numerical methods:

1. The entire performance of the toolbox will be greatly promoted by using Chebyshev polynomial (roots or extrema) locations and quadrature weights. The analytic formulas for locations are available and the polynomials can be expressed in terms of cosine form [100]. Therefore, the generation of the location vector is much cheaper, computer memory requirements [101] and accuracy of the elements [117, 118] for corresponding differentiation arrays can be optimized, and the limitation for maximum number of points can be raised to the machine accuracy (see the discussions in Section 3.1.2). Furthermore, fast cosine transformations using fast Fourier transform algorithm (FFT) are available for differentiation [100, 101] and interpolation. However, the analytic formula for the associated quadrature weights must be derived.

2. Chebyshev polynomials can be used to evaluate a known function series and thus improve the `gdf.m`. It is well-known that the Chebyshev polynomials are optimal for economizing a power series [100, 119]. An example for generating a higher order polynomials without ill-conditioned vandermonde matrix problem can be found in [29].

Application of MWRtools to Higher Dimensional Problems

The initial stage of this study was to build a comprehensive numerical framework and identify its core elements. It has proved to be very useful in many traditional Chemical Engineering problems [29] and has been applied to several industrial applications [30]. The current MWRtools construct the foundation for solving problems in a one-dimensional geometry. The higher dimension version is simply the extension of the tensor products among the basic blocks. How to implement these methods, however, are open computational and "book-keeping" issues. The ability of Matlab cell array and structure should be exploited.

Extension to Irregular Geometry

Simple geometries may be sufficient for those semiconductor manufacturing simulations which usually major characteristics confined in a small and regular-shape region, such as plasma discharge in axial direction between two parallel electrodes. The extension of the numerical techniques to include spectral element formulations may provide a pathway to solving problems in complex geometries.

Methods for Large Scale Numerical Continuation

The global function method results in a full matrix for the discretized system. The numerical continuation methods used in this study were excellent for a small to medium size system. However, the discretized system for plasma simulations are inevitably large. Using QR factorization to find the tangent direction along the solution curve is inappropriate, and Newton-Raphson type corrector is inefficient for a large full matrix. A special treatment for large scale systems must be introduced to enhance the computation while keeping the stability of the

methods. There are vigorous studies in this subject area [105].

Nonlinear Analysis of RF simulations

Similar continuation and bifurcation analysis as the DC simulations can be performed with the same numerical tools. For the periodic solution problems, the stroboscopic representation or Poincare map is extensively used in the study of dynamical systems [62, 120, 121]. The idea is to record the response of the system at a fixed time interval, which coincides with the RF forcing cycle. The variational equation, measuring the sensitivity of the state variables with respect to initial conditions, is integrated along with the system of equations. The eigenvalues (Floquet multipliers) of the sensitivity matrix determine the stability of the periodic orbit, which is stable if they all lie in the unit circle on the complex plane.

Reduced Model for a Broader Range of Operating Conditions

The PCA reduction method is optimal for the snapshots under the given operating conditions. For real time control purposes, the data can be collected around the limit cycle but the perturbed operating conditions should be considered, i.e., include more trial functions from different initial conditions [122].

Model Reduction for Nonlinear Boundary Condition Problems

This study showed the first step of implementation toward real-time model reduction applications. Inertial manifold theory provides the solid theoretical foundation of model reduction for PDE models while the proper orthogonal decomposition method is used to construct the optimal trial functions. There are

several more problems that must be resolved. One outstanding problem involves application of these methods to systems with nonhomogeneous and nonlinear boundary conditions. For the demonstration problem of RF plasma simulation, the boundary conditions are conveniently assumed to be homogeneous due to the fact that the spectral solution is the linear sum of all trial functions. For systems with nonhomogeneous boundary conditions, as used frequently in material processing simulations, the variational formulation similar to FEM can be introduced. The implementation, however, can be conveniently performed using MWRtools, and the major advantage is that the trial functions are not limited to polynomials.

Bibliography

[1] A. Bouchoule. Dusty plasma. *Physics World*, page 47, 1993.

[2] S. J. Choi, P. L. G. Ventzek, R. J. Hoekstra, and M. J. Kushner. Spatial distributions of dust particles in plasma generated by capacitively coupled radio frequency discharges. *Plasma Sources Sci. Technol.*, 3:418–425, 1994.

[3] F. Y. Huang, H. H. Hwang, and M. J. Kushner. A model for transport and agglomeration of particles in reactive ion etching plasma reactors. *J. Vac. Sci. Technol. A.*, 14(2):562, 1996.

[4] T. R. Govindan and M. Meyyappan. One-dimensional modeling studies of the gaseous electronics conference rf reference cell. *J. Res. Natl. Inst. Stand. Technol.*, 100(4):463–472, 1995.

[5] D. B. Graves and K. F. Jensen. A continuum model of dc and rf discharges. *IEEE Trans. Plasma Sci.*, 14(2):78, 1986.

[6] E. Gogolides, H. H. Sawin, and R. A. Brown. Direct calculation of time-periodic steady-state of continuum models of radio-frequency plasmas. *Chem. Engng. Sci.*, 47(15/16):3839–3855, 1992.

[7] J. D. P. Passchier and W. J. Goedheer. A two-dimensional fluid model for an argon rf discharge. *J. Appl. Phys.*, 74(6):3744–3751, 1993.

[8] A. P. Paranjpe. Modeling an inductively coupled plasma source. *J. Vac. Sci. Technol. A.*, 12(4):1221–1228, 1994.

[9] J. P. Boeuf and L. C. Pitchford. Two-dimensional model of a capactively coupled rf discharge and comparisons with experiments in the geseous electronics conference reference reactor. *Phys. Rev. E.*, 51(2):1376–1390, 1995.

[10] Dimitris P. Lymberopoulos and Demetre J. Economou. Two-dimensional self-consistent radio frequency plasma simulations relevant to the gaseous electronics conference rf reference cell. *J. Res. Natl. Inst. Stand. Technol.*, 100(4):473, 1995.

[11] M. Meyyappan, editor. *Computational Modeling in Semiconductor Processing.* Artech House, Boston, 1995.

[12] M. J. Kushner. Advances in plasma equipment modeling. *Solid State Technol.*, page 135, 1996.

[13] M. S. Barnes, T. J. Cotler, and M. E. Elta. A stagger-mesh finite-difference numerical method for solving the transport equations in low pressure rf glow discharges. *J. of Comp. Phys.*, 7:53, 1988.

[14] C. Li and C-H. Wu. Three fluid transport models by particle-in-cell method for rf glow discharges. *IEEE Trans. on Plasma Science*, 20(6):1000, 1992.

[15] M. Surendra and D. B. Graves. Particle simulation of radio-frequency glow discharges. *IEEE Trans. Plasma Sci.*, 19(2):144–157, 1991.

[16] A. Bogaerts and R. Gijbels. Hybrid Monte Carlo-fluid model of a direct current glow discharge. *J. Appl. Phys.*, 78(4):2233, 1995.

[17] M. J. Kushner. Consequences of asymmetric pumping in low pressure plasma processing reactor: A three-dimensional modeling study. *J. Appl. Phys.*, 82(11):5312–5320, 1997.

[18] V. I. Kolobov, H.-M. Wu, and A. Krishnan. A tool for computer aided engineering of inductively coupled plasma sources. *CFD Research Corporation*, 1999.

[19] C. Foias, M. S. Jolly, I. G. Kevrekidis, G. R. Sell, and E. S. Titi. On the computation of inertial manifolds. *Phys. Lett. A.*, 131(7,8):433–436, 1988.

[20] R. Temam. Inertial manifolds. *The Mathematical Intelligencer*, 12(4):68–74, 1990.

[21] H. Sano and N. Kunimatsu. An application of inertial manifold theory to boundary stabilization of semilinear diffusion systems. *J. Math. Ana. Appl.*, 196:18–42, 1995.

[22] P. D. Christofides and P. Daoutidis. Nonlinear control of diffusion-convection-reaction processes. *Comp. & Chem. Engng. Suppl.*, 20:s1071–s1076, 1996.

[23] P. D. Christofides and P. Daoutidis. Finite-dimensional control of parabolic PDE systems using approximate inertial manifolds. *J. Math. Ana. Appl.*, 216:398–420, 1997.

[24] L. Sirovich. Turbulence and the dynamics of coherent structures part I: Coherent structures. *Quart. Appl. Math.*, XLV(3):561–571, 1987.

[25] Sirovich. L., Knight. B. W., and J. D. Rodriguez. Optimal low-dimensional dynamical approximations. *Quart. Appl. Math.*, XLVIII(3):535–548, 1990.

[26] Sirovich. L. and J. D. Rodriguez. Coherent structures and chaos: A model problem. *Phys. Letts. A.*, 120(5):211–214, 1987.

[27] A. E. Deane, I. G. Kevrekidis, G. E. Karniadakis, and S. A. Orszag. Low-dimensional models for complex geometry flows: Application to grooved channels and circular cylinders. *Phys. Fluids A*, 3(10):2337–2354, 1991.

[28] A. Theodoropoulou, R. A. Adomaitis, and E. Zafiriou. Model reduction for optimization of rapid thermal chemical vapor deposition systems. *IEEE trans. Semicond. Manuf.*, 11(1):85–98, 1998.

[29] Y.-h. Lin, H.-Y. Chang, and R. A. Adomaitis. MWRTOOLS: A library for weighted residual method calculations. *Comp. & Chem. Eng.*, accepted for publication 1999. Also ISR TR 98-24.

[30] R. A. Adomaitis, Y.-h. Lin, and H.-Y. Chang. A computational framework for boundary-value problem based simulations. *Simulations*, accepted for publication 1999. also ISR-TR 98-41.

[31] G. Gottlieb and S. A. Orszag. *Numerical Analysis of Spectral Methods: Theory and Applications*. Society for Industrial and Applied Mathematics, Philadelphia, 1977.

[32] C. A. J. Fletcher. *Computational Galerkin Methods*. Springer-Verlag, New York, 1984.

[33] P. Holmes, J. L. Lumley, and G. Berkooz. *Turbulence, Coherent Structures, Dynamical Systems and Symmetry.* Cambridge University Press, Cambridge, 1996.

[34] R. G. Rice and D. D. Do. *Applied Mathematics and Modeling for Chemical Engineers.* John Wiley & Sons, New York, 1995.

[35] J. N. Reddy. *An Introduction to the Finite Element Method.* McGraw-Hill, New York, 2nd edition, 1993.

[36] B. Chapman. *Glow Discharge Processes.* John Wiley & Sons,, New York, 1980.

[37] F. F. Chen. *Introduciton to Plasma Physics.* Plenum Press, New York, 1980.

[38] D. M. Manos and Flamm. D. L. *Plasma Etching: An Introduction.* Academic Press, San Diego, 1989.

[39] H. V. Boenig. *Fundamentals of Plasma Chemistry and Technology.* Technomic Publishing Co., inc, Lancaster, PA, 1988.

[40] A. Sherman. *Chemical Vapor Deposition for Microelectronics, Principles, Technology and Applications.* Noyes Publication, Park Ridge, NJ, 1987.

[41] S. M. Rossnagel, J. J. Cuomo, and W. D. Westwood. *Handbook of Plasma Processing Technology.* Noyes Publication, New York, 1990.

[42] G. Collins and D. J. Rej. Plasma processing of advanced materials. *MRS Bulletin*, page 26, 1996.

[43] L. E. Kline and M. J. Kushner. Computer simulation of materials processing plasma discharges. *Critical Reviews in Solid State and Materials Sciences*, 16(1):1, 1989.

[44] Dimitris P. Lymberopoulos and Demetre J. Economou. Modeling and simulation of glow discharge plasma reactors. *J. Vac. Sci. Technol. A*, 12(4):1229–1236, 1994.

[45] R. B. Bird, W. E. Stewart, and E. N. Lightfoot. *Transport Phenomena.* John Wiley & Sons, New York, 1960.

[46] B. E. Cherrington. *Gaseous Electronics and Gas Lasers.* Pergamon, New York, 1979.

[47] G. G. Lister. Low-pressure gas discharge modeling. *J. Appl. Phys.*, 25:1649, 1992.

[48] J. H. Ingold. Moment method applied to gaseous electrons. *Phys. Rev. A*, 40(7):3855, 1989.

[49] E. Gogolides and H. H. Sawin. Continuum modeling of radio frequency glow discharge I: theory and results for electropositive and electronegative gases. *J. Appl. Phys.*, 72:3971, 1992.

[50] P. J. Chantry. A simple formula for diffusion calculations involving wall reflection and low density. *J. Appl. Phys.*, 62(4):1141, 1987.

[51] A. P. Paranjpe. Studies of gas discharge for dry etching mdeling and diagnostics. *Ph.D. Dissertation, Stanford University.*, 1989.

[52] Dimitris P. Lymberopoulos and Demetre J. Economou. Fluid simulations of glow discharges: Effect of metastable atoms in argon. *J. Appl. Phys.*, 73(8):3668–3679, 1992.

[53] M. Dalvie, M. Surendra, and G. S. Selwyn. Self-consistent fluid modeling of radio frequency discharges in two dimensions. *Appl. Phys. Lett.*, 62:3207–3209, 1993.

[54] M. Meyyappan and T. R. Govindan. Radio frequency discharge modeling: moment equations approach. *J. Appl. Phys.*, 74(4):2250–2259, 1993.

[55] E. Gogolides and H. H. Sawin. Continuum modeling of radiofrequency glow discharges. I. theory and results for electropositive and electronegative gases. *J. Appl. Phys.*, 72(9):3971–3987, 1992.

[56] M. S. Barnes, T. J. Colter, and M. E. Elta. Large-signal time-domain modeling of low-pressure rf glow discharges. *J. Appl. Phys.*, 61(1):81, 1987.

[57] P. J. Jr. Hargis, K. E. Greenberg, P. A. Miller, J. B. Gerardo, J. R. Torczynski, J. R. Roberts, J. K. Olthoff, J.R. Whetstone, R. J. von Brunt, M. A. Sobolewski, H. M. Anderson, M. P. Splichal, J. L. Mock, P. Bletzinger, A. Garscadden, R. A. Gottscho, G. Selwyn, M. Dalvie, J. E. Heidenreich, J. W. Butterbaugh, M. L. Brake, M. L. Passow, J. Pender, A. Lujan, M. E. Elta, D. B. Graves, H. H. Sawin, M. J. Kushner, J. T. Verdeyen, R. Horwath, and T. R. Turner. The gaseous electronics conference radio-frequency reference cell: A defined parallel-plate radio-frequency system for experimental and theoretical studies of plasma-processing discharges. *Rev. Sci. Instrum.*, 65(1):140, 1994.

[58] S. Rauf and M. J. Kushner. The effect of radio frequency plasma processing reactor circuitry on plasma characteristics. *J. Appl. Phys.*, 83(10):5087–5094, 1998.

[59] B. K. McMillin and M. R. Zachariah. Two-dimensional argon metastable density measurements in a radio frequency plasma reactor by planar laser-induced fluorescence imaging. *J. Appl. Phys.*, 77(11):5538, 1995.

[60] B. K. McMillin and M. R. Zachariah. Two-dimensional laser-induced fluorescence imaging of metastable density in low-pressure radio frequency argon plasma with added o_2, cl_2, and cf_4. *J. Appl. Phys.*, 79(1):77, 1996.

[61] S.-K. Park and D. J. Economou. Analysis of low pressure rf glow discharges using a continuum model. *J. Appl. Phys.*, 68(8):3904–3915, 1990.

[62] E. Gogolides and H. H. Sawin. Continuum modeling of radio frequency glow discharges. II. parametric studies and sensitivity analysis. *J. Appl. Phys.*, 72(9):3988–4002, 1992.

[63] M. Meyyappan and T. R. Govindan. Two-dimensional analysis of radio frequency discharges. *IEEE Trans. Plasma Sci.*, 24(1):119–120, 1996.

[64] Dimitris P. Lymberopoulos and Demetre J. Economou. Fluid simulations of radio frequency glow discharges: Two-dimensional argon discharge including metastables. *Appl. Phys. Lett.*, 63(18):2478–2480, 1993.

[65] J. K. Olthoff and K.E. Greenberg. The gaseous electronics conference rf reference cell - an introduction. *J. Res. Natl. Inst. Stand. Technol.*, 100(4):327–339, 1995.

[66] M. E. Riley, K. E. Greenberg, G. A. Hebner, and P. Drallos. Theoretical and experimental study of low-temperature, capacitively coupled, radio-frequency helium plasmas. *J. Appl. Phys.*, 75:2789, 1994.

[67] H. Schlichting. *Boundary-Layer Theory.* McGraw-Hill Book Company, New York, 1979.

[68] D. F. Rogers. *Laminar Flow Analysis.* Cambridge University Press, New York, 1992.

[69] M. Meyyappan and J. P. Kreskovsky. Glow discharge simulation through solutions to the moments of the Boltzmann transport equation. *J. Appl. Phys.*, 68(4):1506, 1990.

[70] G. G. Lister. Plasma modeling for surface processing. *Vacuum*, 45(5):525, 1994.

[71] J. Polman. Recent developments in low pressure gas discharge research. *Physica*, 82C:125, 1976.

[72] A. Bogaerts and R. Gijbels. Modeling of metastable argon atoms in a direct-current glow discharge. *Phys. Rev. A.*, 52(5):3743, 1995.

[73] J. P. Boeuf. A two-dimensional model of dc glow discharges. *J. Appl. Phys.*, 63(5):1342, 1988.

[74] A. Bogaerts and R. Gijbels. Two-dimensional model of a direct current glow dischage: Description of the electrons, argon, ions, and fast argon atoms. *Anal. Chem.*, 68(14):2296, 1996.

[75] E. Gogolides, J.-P. Nicolai, and H. H. Sawin. Comparison of experimental measurements and model predictions for radio-frequency Ar and SF_6 discharges. *J. Vac. Sci. Technol.*, A7(3):1001–1006, 1989.

[76] A. D. Richards, B. E. Thompson, and H. H. Sawin. Continuum modeling of argon radio frequency glow discharges. *Appl. Phys. Lett.*, 50(9):492, 1987.

[77] S.-K. Park and D. J. Economou. Parametric study of a radio-frequency glow discharge using a continuum model. *J. Appl. Phys.*, 68(9):4888, 1990.

[78] T. Makabe and N. Nakano. Modeling and diagnostics of the structure of rf glow discharges in Ar at 13.56 MHz. *Phys. Rev. A.*, 45(4):2520, 1992.

[79] M. J. Kushner, W. Z. Collison, M. M. Grapperhaus, J. P. Holland, and M. S. Barnes. A three-dimensional model for inductively coupled plasma etching reactors: Azimuthal symmetry, coil properties, and comparison to experiments. *J. Appl. Phys.*, 80(3):1337, 1996.

[80] M. J. Colgan, M. Meyyappan, and D. E. Murnick. Very high frequency capacitively coupled argon discharges. *Plasma Sources Science and Technology*, 3:181, 1994.

[81] L. J. Overzet and M. B. Hopkins. *Appl. Phys. Lett.*, 63:2484, 1993.

[82] F. F. Young and C.-H. Wu. Two-dimensional, self-consistent, three-moment simulation of rf glow discharge. *IEEE Trans. Plasma Sci.*, 21:312, 1993.

[83] F. F. Young and C. H. Wu. Radial flow effects in a multidimensional, three-moment simulation of rf glow discharges. *IEEE Trans. Plasma Sci.*, 62(5):473, 1993.

[84] M. L. Michelsen and J. Villadsen. *Polynomial solution of differential equations. In Foundations of Computer-Aided Chemical Process Design*, volume I. NSF, 1981. pages 341-368.

[85] B. A. Finlayson. *The method of weighted residuals and variational principles.* Acdemic Press, New York, 1972.

[86] J. V. Villadsen and W. E. Stewart. Solution of boundray-value problems by orthogonal collocation. *Chem. Eng. Sci.*, 22:1483–1501, 1967.

[87] J. Villadsen and M. L. Michelsen. *Solution of differential equation models by polynomial approximation.* Int. Series in Phys. and Chem. Engng. Sci. Prentice-Hall, Englewood Cliffs, N. J., 1978.

[88] N. K. Madsen and R. F. Sincovec. Algorithm 540: PDECOL, general collocation software for partial differential equations. *ACM Tans. Math. Software*, 5:326–351, 1979.

[89] U. Ascher, J. Christiansen, and R. D. Russell. Collocation software for boundary-value ODEs. *ACM Transactions on Mathematical Software*, 7(2):209–222, 1981.

[90] W. J. Eaton. *Octave - A High-Level Interactive Language for Numerical Computations.* 1995. Edition 1.1 for Octave version 1.1.1.

[91] W. S. Don and A. Solomonoff. *PseudoPack - Pseudo-Spectral Differentiation Software Package User Manual for version 2.3 beta.* Brown University, 1997.

[92] C. R. Mac Cluer. *Boundary Value Problems and Orthogonal Expansions - Physical Problems from a Sobolev Viewpoint.* IEEE Press, New York, 1994.

[93] G. A. Articolo. *Partial Differential Equations and Boundary Value Problems with Maple V.* Academic Press, San Diego, CA, 1998.

[94] J. M. Cooper. Introduction to partial differential equations with MATLAB. 1998.

[95] B. Childs, M. Scott, J. W. Daniel, E. Denman, and P. Nelson, editors. *Codes for Boundary-Value Problems in Ordinary Differential Equations.* Lecture Notes in Computer Science, No. 76. Springer-Verlag, New York, 1979.

[96] K. S. Denison and C. E. Jr. Hamrin. Solution of boundary value problems using software packages: DD04AD and COLSYS. *Chem. Eng. Commum.*, 22:1–9, 1983.

[97] A. H. Stroud. *Numerical quadrature and solution of ordinary differential equations Vol. 10.* Springer-Verlag Applied Mathematical Sciences Series, New York, 1974.

[98] M. L. Michelsen and J. Villadsen. A convenient computational procedure for collocation constants. *Chem. Eng. J.*, 4:64–68, 1972.

[99] R. A. Adomaitis and Y.-h. Lin. A collocation/quadrature-based Sturm-Liouville solver. *Appl. Math. Comp.*, in press 1999. Also in ISR TR 99-1.

[100] W. H. Press, B. P. Flannery, S. A. Teukolsky, and W. T. Vetterling. *Numerical Recipes in FORTRAN: The Art of Scientific Computing.* Cambridge Press, New York, 2nd edition, 1992.

[101] B. Fornberg. *A Practical Guide to Pseudospectral Methods.* Cambridge University Press, New York, 1996.

[102] G. Gottlieb and C. W. Shu. The Gibbs phenomenon and its resolution. *SIAM Review*, 39:644–668, 1997.

[103] K. Fukunaga. *Introduction to Statistical Pattern Recognition.* Academic Press, New York, 2nd edition, 1990.

[104] R. Temam. *Infinite Dimensional Dynamical Systems in Mechanics and Physics*, volume 68 of *Appl. Math. Sci.* Springer-Verlag, New York, 2nd edition, 1997.

[105] E. L. Allgower and K. Georg. *Numerical Continuation Methods: An Introduction.* Springer-Verlag, New York, 1990.

[106] E. L. Allgower and K. Georg. Continuation and path following. *Acta Numerica*, pages 1–64, 1993.

[107] G. Iooss and D. D. Joseph. *Elementary Stability and Bifurcation Theory.* Undergraduate Texts in Mathematics. Springer-Verlag, New York, 1980.

[108] M. Kubicek and M. Marek. *Computational Methods in Bifurcation Theory and Dissipative Structures.* Springer-Verlag, New York, 1983.

[109] R. Seydel. *Practical Bifurcation and Stability Analysis: From Equilibrium to Chaos.* Springer-Verlag, New York, 2nd edition, 1994.

[110] R. A. Holmgren. *A First Course in Discrete Dynamical Systems.* Springer-Verlag, New York, 1994.

[111] K. T. Alligood, T. D. Sauer, and J. A. Yorke. *Chaos: An Introduction to Dynamical Systems.* Springer-Verlag, New York, 1996.

[112] R. A. Adomaitis and Y.-h. Lin. A technique for accurate collocation residual calculations. *Chem. Engng. J.*, 71(2):127–134, 1998. Also ISR TR 98-6.

[113] G. Gottlieb and S. A. Orszag. *Numerical Analysis of Spectral Methods: Theory and Applications.* Society for Industrial and Applied Mathematics, Philadelphia, 1986.

[114] M. Surendra and D. B. Graves. Capacitively coupled glow discharges at frequencies above 13.56 MHz. *Appl. Phys. Lett.*, 59(17):1022–1024, 1991.

[115] J. D. P. Passchier and W. J. Goedheer. Relaxation phenomena after laser-induced photodetachment in electronegative rf discharge. *J. Appl. Phys.*, 73(3):1073–1079, 1993.

[116] G. L. Huppert, H. H. Sawin, and R. A. Brown. Spectral element analysis of radio-frequency glow discharges. *Chem. Engng. Sci.*, 49(10):1601–1611, 1994.

[117] W. S. Don and A. Solomonoff. Accuracy and speed in computing the Chebyshev collocation derivative. *SIAM J. Sci. Comput.*, 16(6):1253–1268, 1995.

[118] W. S. Don and A. Solomonoff. Accuracy enhancement for higher derivatives using Chebyshev collocation and a mapping technique. *SIAM J. Sci. Comput.*, 18(4):1040–1055, 1997.

[119] C. F. Gerald and P. O. Wheatley. *Applied Numerical Analysis.* Addison Wesley, New York, 6th edition, 1999.

[120] I. G. Kevrekidis, L. D. Schmidt, and R. Aris. On the dynamics of periodically forced chemcial reactors. *Chem. Engng. Commun.*, 30:323–330, 1984.

[121] I. G. Kevrekidis, L. D. Schmidt, and R. Aris. Some common features of periodically forced reacting systems. *Chem. Engng. Sci.*, 41(5):1263–1276, 1986.

[122] M. D. Graham and I. G. Kevrekidis. Alternative approaches to the Karhunen-Loève decomposition for model reduction and data analysis. *Comp. & Chem. Engng.*, 20(5):495–506, 1996.